Universidade do Minho
Escola de Ciências

Hugo Manuel Castro Gonçalves

Unusual Photonic Properties Of Doped Nanostructured Polymeric Fibers

fevereiro de 2019

FCT
Fundação para a Ciência e a Tecnologia
MINISTÉRIO DA EDUCAÇÃO E CIÊNCIA

POPH
QUALIFICAR É CRESCER.

QREN
QUADRO DE REFERÊNCIA ESTRATÉGICO NACIONAL
PORTUGAL 2007.2013

Governo da República Portuguesa

UNIÃO EUROPEIA
Fundo Social Europeu

Hugo Manuel Castro Gonçalves **Unusual Photonic Properties Of Doped Nanostructured Polymeric Fibers**

UMinho | 2019

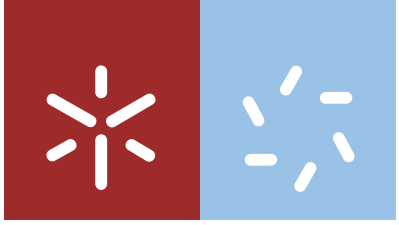

Universidade do Minho
Escola de Ciências

Hugo Manuel Castro Gonçalves

Unusual Photonic Properties Of Doped Nanostructured Polymeric Fibers

Tese de Doutoramento
Doutoramento em Física

Trabalho efetuado sob a orientação do
Professor Doutor Michael Besley

fevereiro de 2019

DECLARAÇÃO DE INTEGRIDADE

Declaro ter atuado com integridade na elaboração da presente tese. Confirmo que em todo o trabalho conducente à sua elaboração não recorri à prática de plágio ou a qualquer forma de falsificação de resultados.

Mais declaro que tomei conhecimento integral do Código de Conduta Ética da Universidade do Minho.

Universidade do Minho, 22 de Fevereiro de 2019

Nome completo: Hugo Manuel Castro Gonçalves

Assinatura: Hugo Manuel Castro Gonçalves

Agradecimentos

Em primeiro lugar, e sobre tudo, eu estou profundamente grato e irá ficar para sempre comigo o esmerado apoio que o Doutor Michael Belsley concedeu-me perante todas as diversidades que ocorreram ao longo destes 4 anos em que desenvolvi a minha tese de doutoramento. De adversidade em adversidade, o professor esteve sempre presente mesmo quando forçado, por motivos maiores, a não estar presente. É de enaltecer os mais sentidos agradecimentos.

Gostava de agradecer às seguintes pessoas e organizações pelo seu incondicional apoio e ajuda na realização da minha tese:

A Doutora Etelvina Gomes pelas suas intervenções perspicazes, pelo apoio incondicional e disponibilidade em ajudar durante todas as etapas de produção e discussão.

A Doutora Marlene Lúcio pela ajuda e pelas possibilidades que forneceu permitindo-me alargar o conhecimento e aplicações, o que tornou a realização desta tese uma tarefa menos penosa.

À colega Inês Saavedra pela ajuda na obtenção dos melhores parâmetros para a produção e deposição das nanofibras usando a técnica de electrospinning.

A Doutora Rute Ferreira da Universidade de Aveiro pela atenção e ajuda que forneceu ao se mostrar disponível para ajudar. Ao Doutor Paulo Lopes pela imprescindível ajuda concedida na realização dos ensaios de espectroscopia Raman.

À Universidade do Minho e ao departamento e centro de física da mesma pelo suporte e material disponibilizado.

À FCT e principalmente ao Estado Português pelo apoio financeiro ao longo de todo o meu percurso académico.

À Família. Eterna.

Abstract

The escalating interest in organic nanotechnology has stimulated the development of new materials that can undergo self-assembly into well-ordered structures at a nanometer scale. This ground up molecular self-assembly of new materials offers the possibility of either enhancing already desirable properties or obtaining through synergies entirely new capabilities. The ability to control molecular order during self-assembling processes within confined geometries is an especially important goal that will lead to deep insights regarding the relationship between structure and a range of desired physical properties. As a particular case, electro-spun nanofibers are an interesting model system for studying how the basic interactions amongst components can lead to emergent optical properties that are distinct from those of the isolated component molecular species.

Organic materials have a number of advantages over inorganic materials for nonlinear optical (NLO) applications. The ease of modification of organic molecular structures makes it possible to synthesize tailor-made molecules and to fine-tune their properties for specific applications. A large number of organic π-conjugated molecules have been investigated and certain guidelines have been established to obtain large second-order nonlinear responses. The most common strategy is to link donor and acceptor moieties on opposite ends of a π-conjugated aromatic spacer. This configuration promotes spatial charge transfer and a strong difference in dipole moments between the ground and excited electronic states. However, more than roughly 80% of all π-conjugated organic molecules crystallize in centrosymmetric space groups, producing materials with no second order bulk susceptibility.

para-nitroaniline (*p*Na) is a paradigmatic molecular building block for organic nonlinear optics. In spite of its exceptional molecular nonlinear optical response, *p*Na crystallizes in a centrosymmetric space group $P2_1/n$, which impedes the observation of any bulk macroscopic second-order optical effect. To overcome this restriction two independent approaches were used in the present thesis; embedding the molecules into nano-structured environments such as polymeric nanofibers and in confined polymeric matrices. In the case of the polymeric nanofibers, the self-assembly of *p*Na nanocrystals and their effective manipulation are achieved by tuning the deposition parameters of the electrospinning process. The effective resultant second order susceptibility is a few orders higher that the inorganic crystal of KDP used to calibrate the polarimetry setup. The size of the

nanocrystals, the induced strain and their surface-to-volume ratio are the key aspects behind this unusual nonlinear response. Ensuring the assemblage of the *p*Na into highly oriented meso-crystalline structures with a dominant acentric surface can also be achieved using a modified version of capillarity growth. Using this method, we are able to obtain oriented structures of *p*Na with a second order effect higher than that observed in the doped polymeric nanofibers. The breaking of the nominally centrosymmetric nature of *p*Na at its surface seems to be insufficient to explain the unusual magnitude of the second order effect. The combination of Raman analysis and synchrotron radiation scattering suggest that bulk effects make a significant contribution to this second order nonlinear optical response.

Abstract

The escalating interest in organic nanotechnology has stimulated the development of new materials that can undergo self-assembly into well-ordered structures at a nanometer scale. This ground up molecular self-assembly of new materials offers the possibility of either enhancing already desirable properties or obtaining through synergies entirely new capabilities. The ability to control molecular order during self-assembling processes within confined geometries is an especially important goal that will lead to deep insights regarding the relationship between structure and a range of desired physical properties. As a particular case, electro-spun nanofibers are an interesting model system for studying how the basic interactions amongst components can lead to emergent optical properties that are distinct from those of the isolated component molecular species.

Organic materials have a number of advantages over inorganic materials for nonlinear optical (NLO) applications. The ease of modification of organic molecular structures makes it possible to synthesize tailor-made molecules and to fine-tune their properties for specific applications. A large number of organic π-conjugated molecules have been investigated and certain guidelines have been established to obtain large second-order nonlinear responses. The most common strategy is to link donor and acceptor moieties on opposite ends of a π-conjugated aromatic spacer. This configuration promotes spatial charge transfer and a strong difference in dipole moments between the ground and excited electronic states. However, more than roughly 80% of all π-conjugated organic molecules crystallize in centrosymmetric space groups, producing materials with no second order bulk susceptibility.

para-nitroaniline (*p*Na) is a paradigmatic molecular building block for organic nonlinear optics. In spite of its exceptional molecular nonlinear optical response, *p*Na crystallizes in a centrosymmetric space group $P2_1/n$, which impedes the observation of any bulk macroscopic second-order optical effect. To overcome this restriction two independent approaches were used in the present thesis; embedding the molecules into nano-structured environments such as polymeric nanofibers and in confined polymeric matrices. In the case of the polymeric nanofibers, the self-assembly of *p*Na nanocrystals and their effective manipulation are achieved by tuning the deposition parameters of the electrospinning process. The effective resultant second order susceptibility is a few orders higher that the inorganic crystal of KDP used to calibrate the polarimetry setup. The size of the

nanocrystals, the induced strain and their surface-to-volume ratio are the key aspects behind this unusual nonlinear response. Ensuring the assemblage of the *p*Na into highly oriented meso-crystalline structures with a dominant acentric surface can also be achieved using a modified version of capillarity growth. Using this method, we are able to obtain oriented structures of *p*Na with a second order effect higher than that observed in the doped polymeric nanofibers. The breaking of the nominally centrosymmetric nature of *p*Na at its surface seems to be insufficient to explain the unusual magnitude of the second order effect. The combination of Raman analysis and synchrotron radiation scattering suggest that bulk effects make a significant contribution to this second order nonlinear optical response.

Resumo

O crescimento do interesse pela nanotecnologia orgânica estimulou o desenvolvimento de novos materiais que podem ser sujeitos ao processo de auto-organização em estruturas bem ordenadas à escala nanométrica. Essa auto-ordenação molecular dos novos materiais oferece a possibilidade de melhorar as propriedades apelativas, ou obter, por meio de sinergias, características inteiramente novas. A capacidade de controlar a ordem molecular durante os processos de auto-ordenação no interior de geometrias confinadas é uma abordagem especialmente importante que pode aprofundar o conhecimento sobre a relação entre a estrutura e a gama de propriedades físicas desejadas. As nanofibras produzidas por *electrospinning* são um exemplo particular de um sistema modelo interessante para estudar como é que as interações básicas entre aos diferentes componentes produzem propriedades óticas inesperadas que são distintas da das espécies moleculares constituintes.

Os materiais orgânicos têm várias vantagens sobre os materiais inorgânicos em aplicações de ótica não linear (NLO). A facilidade de modificação das estruturas moleculares torna possível sintetizar moléculas feitas à medida e ajustar as suas propriedades para aplicações específicas. Um grande número de moléculas π conjugadas foi investigado e certas diretrizes foram estabelecidas para obter grandes respostas não-lineares de segunda ordem. A estratégia mais comum é ligar grupos dadores e aceitadores de eletrões em extremos opostos de um espaçador aromático π conjugado. Essa configuração promove transferência de carga elétrica espacialmente, produzindo uma enorme diferença nos momentos dipolares entre os estados eletrónicos fundamental e excitado. No entanto, mais de 80% de todas as moléculas orgânicas π conjugadas cristalizam em grupos espaciais centro-simétricos, inviabilizando a geração de efeitos óticos de segunda ordem em cristais macroscópicos.

A *para*-nitroanilina (*p*Na) é uma molécula orgânica paradigmática para a obtenção de ótica não linear. Apesar da sua excecional resposta molecular de ótica não-linear, a *p*Na cristaliza num grupo espacial centro-simétrico $P2_1/n$, que impede a observação de qualquer efeito macroscópico de segunda ordem. Para ultrapassar essa restrição foram utilizadas na presente tese duas abordagens independentes; incorporação das moléculas em ambientes nanoestruturados, como nanofibras poliméricas e em matrizes poliméricas confinadas espacialmente. No caso das nanofibras poliméricas, a auto-organização da *p*Na em nanocristais e sua manipulação foi obtida

através da alteração dos parâmetros de deposição relacionados com a técnica de *electrospinning*. A suscetibilidade de segunda ordem efetiva resultante é algumas ordens mais intensa que o cristal inorgânico KDP usado para calibrar a montagem experimental de polarimetria. O tamanho dos nanocristais, a tensão induzida e sua relação área de superfície e volume são os principais parâmetros por detrás da resposta não-linear inesperada. A confirmação da organização da *p*Na em estruturas meso-cristalinas altamente orientadas com uma superfície acêntrica dominante também foi conseguida usando uma versão modificada do método de crescimento em capilar. Utilizando este método, conseguimos obter estruturas orientadas de *p*Na com um efeito de segunda ordem superior ao observado nas nanofibras poliméricas dopadas. A quebra da natural centro-simetria da *p*Na ao nível da sua superfície parece ser insuficiente para explicar a magnitude do efeito ótico de segunda ordem inesperado. A combinação da espectroscopia de Raman e difração de radiação raio-X em sincrotrão sugere que os efeitos de volume contribuem significativamente para esta resposta ótica não linear de segunda ordem.

ABREVIATIONS

AFM – Atomic Force Microscope

DAST – *trans*-4-[4-(dimethylamino)-*N*-methylstilbazolium] *p*-tosylate

FLIM – Fluorescence lifetime image microscope

KDP – Dihydrogen Phosphate

*M*NA – 2-methyl-4-nitroaniline

NLO – Non-linear optical properties

NPP – (4-nitrophenyl)-(L)-prolinol

PCL – Polycaprolactone

PEO – Polyethylene glycol

PLLA – poly-L-lactic acid

PMMA – Poly(methyl methacrylate)

PMT – Photon multiplied tube

pNa – *para*-nitroaniline

POM – 3-methyl-4-nitropyridine-1-oxide

PS – Polystyrene

PVA – Poly(vinyl alcohol)

SAXS – Small Angle X-ray scattering

SEM – Scanning Electron Microscope

SHG – Second Harmonic Generation

TATB – 1,3,5-trinitro-2,4,6-triaminobenzene

TPA – Two-Photon absorption

WAXS - Wide Angle X-ray scattering

Index

1 Introduction

This chapter introduces the main topics related to the present thesis. A contextualization of the work is provided within the emergent field of organic, or carbon-based, technologies applied to nanophotonics, as a major area of interest because they are adaptable, inexpensive, plentiful and lightweight. Additionally, the general goals and specific objectives of the present study are presented, followed by a short section outlining the overall structure of this dissertation.

1.1 General overview

Organic optoelectronic materials have been reported in the literature for almost a century. One of the first examples is anthracene; the first studies of its optical and electronic properties were reported in the 1910s[1,2]. In the 1960s and 1970s, interest in such materials intensified, motivated by the discovery of electroluminescence in molecular crystals and of conducting polymers[3–5]. However, a real surge of interest in the field of organic optoelectronics occurred during the past two decades, with Joseph Zyss[1] and Larry Dalton[2] playing central roles in the field.

Even more recently, the new concepts in the physics of metamaterials and the rapid development of nanoscale fabrication technologies have rejuvenated the field of nanophotonics. It has experienced an explosive growth in recent years, enabling various applications relying on flexible and efficient subwavelength light manipulations[6]. Nanophotonics occupies the area where photonics (photons) merge with nanoscience and nanotechnology, and is related with the material (electrons) interactions, that is the generation, transmission, modulation and detection of excitation in this confined environmental of the nanomaterials. Nanotechnology allows researchers to optimize materials properties such as mechanical strength, and thermal and chemical stability. In a similar manner, strengthening the non-linear optical response or optimizing the electrical and optical properties of individual materials can be accomplished by creating hybrid structures using similar or even markedly different materials[7]. Organic compounds, being easy to alter chemically or structurally are particularly attractive components for these hybrid materials and are key elements of many current photonics applications and components[8,9].

One crucial technological breakthrough for this immerging research area of organic compounds for optoelectronic application has been the rapid evolution of new laser sources[10]. The time when the laser was seen as a solution in search of a problem is long past. Theodore H. Maiman, a physicist at Hughes Research Laboratories in Malibu in California could not have foreseen the far-ranging impact that his first demonstration of a laser system would bring about[11,12]. He constructed the first laser using a cylinder of synthetic ruby measuring 1 cm in diameter and 2 cm long, with the ends silver-coated to make them reflective and able to serve as a Fabry-Perot resonator, employing photographic flash lamps as the laser's pump source. After his demonstration

[1] https://www.researchgate.net/profile/Joseph_Zyss
[2] https://scholar.google.com/citations?user=Vmz9ul0AAAAJ&hl=en

both experimental and theoretical research in laser physics exploded. As an example, Logan E. Hargrove, Richard L. Fork and M.A. Pollack reported the theory for a mode-locked laser in 1963[13]. In their first demonstration, they report the use of a helium-neon laser with an acousto-optic modulator as a system to achieve ultra-fast laser pulses. Schawlow and Bloembergen used a laser for the first time as a source for spectroscopic studies[14]. Their contributions and developments of the new field of laser spectroscopy and nonlinear optics were recognized with the Nobel Prize in physics in 1981. Laser spectroscopy has developed rapidly into a very successful field of scientific and technological endeavor. Ranging from applications in analytical spectroscopy to Bose-Einstein condensation[15]. Another mark in laser research was achieved with the realization of ultrafast pulses below 100 fs, revolutionized by the Kerr lens mode-locking mechanism [16]. Ultra-fast laser pulses allow researchers to transfer an appreciable population to selective excited states facilitating fluorescence spectroscopy and optical pumping experiments with high temporal and spatial resolution with excellent signal to noise ratios, an essential task in high sensitivity spectroscopy[17]. Lasers serve as radiation sources in the spectral range from the ultra-violet to the infra-red with extremely narrow bandwidths and with high spectral power densities. On the other hand, detection sensitivity increases with increasing spectral resolution $\omega/\Delta\omega$ as long as $\Delta\omega$ is still larger than the linewidth $\delta\omega$ of the absorption line. Laser pulses with a durations of 100 fs or less are opening doors in transient absorption studies and in rapid relaxation processes[18]. A complementary aspect of ultra-fast pulses is that their high spectral power densities they can be used to measure and study phenomena that require high peak power but low energy pulses, particularly non-linear optical effects[19]. These effects have a quadratic or higher dependence on the incident power.

Non-linear phenomena, the central part of this dissertation, have been observed at wavelengths from deep infrared to extreme ultra-violet, and even used to generate THz radiation[20]. Crystals, amorphous materials, polymers, liquid crystals, semiconductors, organics, liquids, gases and plasmas all exhibit optical nonlinear effects. Some examples of second order nonlinear effects are harmonic generation, frequency mixing and optical parametric oscillators. Examples of third order nonlinear effects are refractive index modulation, self-phase modulation, Kerr lens induced mode-locking, four wave-mixing, photo-refractivity, two-photon absorption and optical phase conjugation. Third order effects can also be used to create spatial solitons and optical bistability[21]. Nonlinear optical materials are expected to have a bright future in applications where photonic and electronic

integration is a crucial feature, such as, fast communication, data storage, quantum optics and quantum computing, to name a few, with many more to come[22,23].

1.2 Objectives

The central focus of the work presented in this PhD thesis is to understand in detail the physical mechanisms behind the surprisingly large second order nonlinear optical response of Poly(methyl methacrylate) (PMMA) electro-spun nanofibers doped with *para*-Nitroaniline (*p*Na). More fundamentally, it is hoped that this understanding will provide a means to open new pathways for developing organic optoelectronic devices. The versatility of the electrospinning[24,25], the characteristic of polymeric matrices and the tunability of the organic chromophores are the main variables that can be adjusted to optimize the second order nonlinear optical response.

Previous work of our group sparked the motivation to explore this approach as a main strategy to extend the possibilities of organic push-pull molecules. The simplicity of the *p*Na molecule represents the ideal choice to identify the main mechanisms behind the large SHG response present in this hybrid material, polymeric nanofibers doped with *p*Na.

The role of each part of the electrospinning process has an influence on the final SHG response of an individual nanofiber. Manipulating the speed of the polymeric jet solution during the electrospinning process, deposition rate and the applied voltage were all observed to influence the SHG response, but the specific physical mechanism behind SHG in the nanofibers was not known. Using a light source like synchrotron radiation to characterize the variation of the size and the strain of the nanocrystals as a function of the deposition parameters is one means of trying to uncover the origin of the nanofiber's SHG response.

Another key aspect necessary to understand is the effect of the polymeric matrix on the self-assembly process that occurs inside of the nanofiber. This was explored using an altered version of the capillary growth on several polymeric matrices. These matrices were obtained using different polymers such as PMMA polymer with different molecular weights, polymers with similar optical properties polystyrene (PS) and semi-crystalline polymers polycaprolactone (PCL). At the end, the extracted information can provide insights for the manufacturing of organic devices.

I believe this approach of restricting the self-assembly of the organic compounds inside a polymeric matrix host, be it a nanofiber or layered structure, is a mechanism to consider. These methods are

able to overcome the main limitations connected with the use of the organic compounds in manufacturing optical devices for a variety of present and future applications.

1.3 Thesis Structure

This thesis is divided into four introductory chapters. The first one aims at introducing the topic, as well, a detailed description of the main objectives. Chapter 2 describes the mathematical description of light and light-matter interactions with a special focus on the description of SHG and ultra-fast lasers. This chapter, provides as well, a general introduction to the topic of nanophotonic, organic materials and a detailed description of the *p*Na molecule. Then, chapter 3 introduces a few self-assembling approaches used in engineering to obtain a desired shape or structure, exploiting and manipulating the natural organization of the organic compounds. At the end of the chapter a brief introduction to the mathematical description of the mechanism that governs the self-assemble process is given. Chapter 4 is dedicated to the more important experimental aspects. This chapter describes the experimental work, as well, the main characterization techniques employed. Chapter 5 reprints three manuscripts, that were elaborated during the last years and that represent the essential outcome of the author's research activity.

The last chapter of this thesis contains a brief conclusion and outlines future perspectives that were opened by this work.

1.4 Bibliography

1. A. Pochettino, "Sull' effetto fotoelettrico nell' Antracene," Atti R. Accad. Dei Lincei **15**(5), 171 (1906).

2. M. Phillips, "The chemistry of anthraquinone," Chem. Rev. **6**(1), 157–174 (1929).

3. H. Sasabe, T. Furuno, and T. Wada, "Photovoltaic Effects in Polymer Thin Films," Mol. Cryst. Liq. Cryst. Inc. Nonlinear Opt. **160**(1), 281–296 (1988).

4. R. S. Potember, R. C. Hoffman, H. S. Hu, J. E. Cocchiaro, C. A. Viands, R. A. Murphy, and T. O. Poehler, "Conducting organics and polymers for electronic and optical devices," in *Polymer* (1987), **28**(4), pp. 574–580.

5. R. R. Chance, R. H. Baughman, J. L. Bredas, H. Eckhardt, R. L. Elsenbaumer, J. E. Frommer, L. W. Shacklette, and R. Silbey, "Conducting Complexes of Conjugated Polymers - a Comparative-Study," Mol. Cryst. Liq. Cryst. **83**(1–4), 1249–1259 (1982).

6. M. Aeschlimann, M. Bauer, D. Bayer, T. Brixner, F. J. García De Abajo, W. Pfeiffer, M. Rohmer, C. Spindler, and F. Steeb, "Adaptive subwavelength control of nano-optical fields," Nature **446**(7133), 301–304 (2007).

7. B. P. Isaacoff and K. A. Brown, "Progress in Top-Down Control of Bottom-Up Assembly," Nano Lett. **17**(11), 6508–6510 (2017).

8. J. Xu, S. Semin, T. Rasing, and A. E. Rowan, "Organized chromophoric assemblies for nonlinear optical materials: Towards (Sub)wavelength scale architectures," Small **11**(9–10), 1113–1129 (2015).

9. S. Ahmad, "Organic semiconductors for device applications: Current trends and future prospects," J. Polym. Eng. **34**(4), 279–338 (2014).

10. S. Chénais and S. Forget, "Recent advances in solid-state organic lasers," Polym. Int. **61**(3), 390–406 (2012).

11. T. H. Maiman, "Stimulated optical radiation in Ruby," Nature **187**(4736), 493–494 (1960).

12. C. H. Gerlt, "Obituary: Theodore H. Maiman (1927–2007)," Nature **447**(7145), 654–654 (2007).

13. L. G. Wright, D. N. Christodoulides, and F. W. Wise, "Spatiotemporal mode-locking in multimode fiber lasers," Science (80-.). **358**(6359), 94–97 (2017).

14. N. Bloembergen, "Nonlinear optics and spectroscopy," Rev. Mod. Phys. **54**(3), 685–695 (1982).

15. B. H. Bransden and C. J. Joachin, "The physics of atoms and molecules," in *Optical Astronomical Spectroscopy* (IOP Publishing Ltd, 1983).

16. T. Brabec, C. Spielmann, P. F. Curley, and F. Krausz, "Kerr lens mode locking," Opt. Lett. **17**(18), 1292 (1992).

17. L. Lepetit, G. Chériaux, and M. Joffre, "Linear techniques of phase measurement by femtosecond spectral interferometry for applications in spectroscopy," J. Opt. Soc. Am. B **12**(12), 2467 (1995).

18. U. Megerle, I. Pugliesi, C. Schriever, C. F. Sailer, and E. Riedle, "Sub-50 fs broadband absorption spectroscopy with tunable excitation: putting the analysis of ultrafast molecular dynamics on solid ground," Appl. Phys. B Lasers Opt. **96**(2–3), 215–231 (2009).

19. J. L. Hall, J. Ye, S. A. Diddams, L. S. Ma, S. T. Cundiff, and D. J. Jones, "Ultrasensitive spectroscopy, the ultrastable lasers, the ultrafast lasers, and the seriously nonlinear fiber: A new alliance for physics and metrology," IEEE J. Quantum Electron. **37**(12), 1482–1492 (2001).

20. R. Thomson, C. Leburn, and D. Reid, eds., *Ultrafast Nonlinear Optics* (Springer International Publishing, 2013).

21. H. Gibbs, *Optical Bistability: Controlling Light With Light* (Academic Press, 2012).

22. S. Suresh and D. Arivuoli, "Nanomaterials for nonlinear optical (NLO) applications: A review," Rev. Adv. Mater. Sci. **30**(3), 243–253 (2012).

23. E. Garmire, "Nonlinear optics in daily life," Opt. Express **21**(25), 30532 (2013).

24. W. E. Teo and S. Ramakrishna, "A review on electrospinning design and nanofibre assemblies," Nanotechnology **17**(14), R89–R106 (2006).

25. R. Sahay, P. S. Kumar, R. Sridhar, J. Sundaramurthy, J. Venugopal, S. G. Mhaisalkar, and S. Ramakrishna, "Electrospun composite nanofibers and their multifaceted applications," J. Mater. Chem. **22**(26), 12953 (2012).

2 Theory and Framework

This chapter is a brief resume of the major topics embraced in this dissertation. The chapter begins with a small introduction guiding the reader through the framework of the investigation. There follows a short revision of light-matter interactions, including the linear and nonlinear optical response of matter. Next, a more detailed introduction to the NLO effect known as second harmonic generation (SHG) is given. The basic theory of ultra-fast Kerr lens mode-locked lasers is then covered, followed by a short description of various nanophotonics applications and an indication of how organic compounds might help solve several major challenges in the field. The chapter ends by discussing the main arguments in favour of using *p*Na as a building block for a novel nanophotonic material, motivating the work undertaken during the elaboration of this dissertation.

2.1 Framework

Applications, or devices, that rely on the emission, modulation or control of photons are of increasing technological importance. Lasers, displays and sensors are a few examples of light-emitting devices. The electrical modulation of light emission is, for example, key in many applications connected with optical communications. The electronic control of the light emission pathways opens up the possibility of novel types of nanophotonic devices, based on active near field light-matter interactions [1]. The performance of nanophotonic devices relies essentially on our ability to tailor and control electromagnetic fields on a sub-wavelength scale, in much the same way as the wave function in electronic nanostructures is localized on an atomic scale. This control has already been achieved in metamaterials, photonic and plasmonic crystals, nanoscale waveguides, resonators, switches or optical antennas [2–4]. Often the efficiency of these devices depends on the control of the relevant material properties at a sub-wavelength spatial scale.

Looking at the example of the evolution of transistor based integrated circuits, where the decrease in transistors size has doubled every two years (Moore's law), many researchers around the world are pursuing the goal of shrinking photonic devices until they fit onto integrated circuits. In this demanding task, the search for the best materials as the building blocks for miniaturizing the photonic components will be key to routinely employing nanophotonics in a variety of applications including communication and data processing [5,6].

It is well known that organic materials with donor and acceptor entities separated by an extended π-system conjugation often interact strongly with light [7] experiencing significant intra-molecular charge transfer upon absorption. This interaction leads to strong nonlinear responses such two-photo absorption (TPA) and second harmonic generation (SHG) where the interaction with the light can be quantified by measuring the two-photon absorption cross-section and the effective non-linear susceptibility, respectively [8,9]. Larger cross sections allow excitation at lower incident intensities, limiting light induced damage and increasing the efficiency of applications such as microscopy or data storage. The same happens in applications were the SHG is used as a mechanism for light generation and detection. An increase of the effective conjugation length leads to a more extensive π-electron delocalization and greater charge transfer distances, both of which increase the induced dipole moment of the excited state and strengthen the effective third order NLO response associated with processes such as TPA. In contrast, in organic π-systems, the second order NLO coefficients result from the asymmetric polarization of the electron cloud. For

this reason, SHG is very sensitive to the local symmetry of system. Unfortunately, strong donor-acceptor molecules tend to crystallize in centrosymmetric structures due to the strong dipole-dipole interaction that aligns the molecules in alternating head to tail chains. This precludes the use of the majority of organic donor-acceptor bulk crystals as second harmonic generators or second order electro-optic modulators as bulk centrosymmetric structures are prohibited by symmetry from generating a macroscopic second order nonlinear response [8].

However, the fact that bulk centrosymmetric structures cannot generate a macroscopic second harmonic generation does not necessarily imply the rejection of the material for second-order NLO applications [10,11]. Even in centrosymmetric arrangements, at the surface the inversion symmetry is broken, permitting a dipolar contribution to the harmonic field. It is also well known that the local electric fields induced at interfaces by incident radiation can have a noticeable influence on the TPA cross-sections. Consequently, for these types of materials, it is the surface upon which attention should be focused; this is where structure induced SHG becomes possible.

2.2 Theory of the electromagnetic field

Electromagnetic fields, including light, should be theoretically treated as three-dimensional vector fields. Physically, such fields are fully determined by their divergence and curl properties. The well known mathematical description for electromagnetic fields is summarized in the four Maxwell equations. They explain the structure and properties of light. In Gaussian units and in their macroscopic version they are:

$$\begin{aligned}
\nabla \cdot \mathbf{D}(r,t) &= 4\pi\boldsymbol{\zeta}(r,t) \\
\nabla \cdot \mathbf{B}(r,t) &= 0 \\
\nabla \times \mathbf{H}(r,t) &= \frac{4\pi}{\mathrm{c}}\mathbf{j} + \frac{1}{\mathrm{c}}\frac{\partial \mathbf{D}(r,t)}{\partial t} \\
\nabla \times \mathbf{E}(r,t) &= -\frac{1}{\mathrm{c}}\frac{\partial \mathbf{B}(r,t)}{\partial t}
\end{aligned} \tag{2.1}$$

Here $\mathbf{B} = \mu\mathbf{H}$ is the magnetic field (at optical frequencies normally the magnetic permeability $\mu = 1$), $\mathbf{D} = \varepsilon\mathbf{E}$ is the dielectric displacement[1], ζ the free charge density, c the speed of light and $\mathbf{j}$ the current density.

Maxwell's equations are partial differential equations of first order. It is often helpful to make a Fourier decomposition with respect to time and consider only harmonic fields. Henceforth, we will use,

$$\mathbf{E}(r,t) = \mathbf{E}(r)e^{-i\omega t}, \quad \mathbf{B}(r,t) = \mathbf{B}(r)e^{-i\omega t} \tag{2.2}$$

and if no source are present ($\zeta = 0, \quad \mathbf{j} = 0$) Maxwell's equations reduce to:

$$\begin{aligned} &\nabla \cdot \mathbf{D}(r,t) = 0 \\ &\nabla \cdot \mathbf{B}(r,t) = 0 \\ &\nabla \times \mathbf{H}(r,t) - \frac{1}{\mathrm{c}} \frac{\partial \mathbf{D}(r,t)}{\partial t} = 0 \\ &\nabla \times \mathbf{E}(r,t) + \frac{\partial \mathbf{B}(r,t)}{\partial t} = 0 \end{aligned} \tag{2.3}$$

2.3 Linear and nonlinear response

When an external source of electromagnetic radiation is applied to a polarizable medium, the electrons in the material respond with a microscopic shift in their positions while remaining bound to their associated atoms inducing internal fields. The collective effect on the electric displacement, $\mathbf{D}$, of these displaced electrons is characterized by a macroscopic response known as the polarization of the material, $\mathbf{P}$. In terms of Maxwell's theory it becomes useful to distinguish between bound charge distributions and free charges, which are represented as ζ in the set of equations (2.1). The constitutive relations that describe the material response to the applied fields are represented by

$$\mathbf{D} = \mathbf{E} + 4\pi\mathbf{P}; \quad \mathbf{B} = \mathbf{H} + 4\pi\mathbf{M} \tag{2.4}$$

Where $\mathbf{P}$ is the dipole moment per unit of volume and $\mathbf{M}$ refers to the magnetic moment per unit of volume. Since attention in this dissertation is focused only on fields at optical frequencies

[1] This relation connects the microscopic response with a macroscopic field

for which the magnetic response of most materials is negligible, it is assumed that $\mathbf{M}=0$. Then combining Maxwell's equations one obtains,

$$\nabla^2\mathbf{E}-\nabla\left(\nabla\cdot\mathbf{E}\right)-\frac{1}{c^2}\frac{\partial^2\mathbf{E}}{\partial t^2}-\frac{4\pi}{c^2}\frac{\partial^2\mathbf{P}}{\partial t^2}=0 \tag{2.5}$$

This means that for a full microscopic theoretical description of the response of a polarizable material, one requires the relation between the macroscopic electric field $\mathbf{E}$ and the induced polarization, $\mathbf{P}$. To proceed, some simplifying assumptions are made. The laboratory fields of interest are typically a few orders of magnitude smaller than the electric fields experienced by the electrons in atoms, or molecules, in material under investigation. Under these circumstances, it is possible to expand $\mathbf{P}(r,t)$ in a Taylor series in powers of the applied macroscopic field $\mathbf{E}(r,t)$. The αth cartesian component of the dipole moment per unit volume is a function of the three Cartesian components of the electric field, represented by $\mathbf{E}_\beta=\mathbf{E}_\beta(r,t)$ with $\beta\in\{x,y,z\}$; therefore the Taylor series is written as follows:

$$\begin{aligned}\mathbf{P}_\alpha(r,t)=\mathrm{P}_\alpha^0+\sum_\beta\left(\frac{\partial\mathrm{P}_\alpha}{\partial\mathrm{E}_\beta}\right)\mathrm{E}_\beta+\frac{1}{2!}\sum_{\beta\gamma}\left(\frac{\partial^2\mathrm{P}_\alpha}{\partial\mathrm{E}_\beta\,\partial\mathrm{E}_\gamma}\right)\mathrm{E}_\beta\,\mathrm{E}_\gamma+\\ \frac{1}{3!}\sum_{\beta\gamma\delta}\left(\frac{\partial^3\mathrm{P}_\alpha}{\partial\mathrm{E}_\beta\,\partial\mathrm{E}_\gamma\,\partial\mathrm{E}_\delta}\right)\mathrm{E}_\beta\,\mathrm{E}_\gamma\,\mathrm{E}_\delta+\cdots\end{aligned} \tag{2.6}$$

The above expansion assumes that the dipole moment $\mathbf{P}(r,t)$ depends on the electric field $\mathbf{E}$ at the same point r in space and at same time t. This imposition of an instantaneous response is equivalent to assuming the material has no memory and is clearly violated if the material absorbs some of the incident radiation field. While more general treatments are possible this is sufficient to describe the generation of second harmonic light by transparent media, one of the main objectives of this dissertation.

Further assuming, that in the absence of an applied electric field the material under study has no net dipole moment per unit volume, the field independent term in the above expansion can be neglected and following tradition the various tensor coefficients are written as nth order susceptibilities:

$$\mathbf{P}_\alpha(r,t)=\sum_\beta\chi^1_{\alpha\beta}\,\mathrm{E}_\beta+\sum_{\beta\gamma}\chi^2_{\alpha\beta\gamma}\,\mathrm{E}_\beta\,\mathrm{E}_\gamma+\sum_{\beta\gamma\delta}\chi^3_{\alpha\beta\gamma\delta}\,\mathrm{E}_\beta\,\mathrm{E}_\gamma\,\mathrm{E}_\delta+\cdots \tag{2.7}$$

The first term, χ^1 is the linear susceptibility (usually a diagonal matrix) and χ^2 and χ^3 are referred to as the second and third order susceptibilities, respectively. The number of subscripts indicated that the nth order susceptibility χ^n is a tensor of rank $(n+1)$. In the following develop it will be convenient to decompose the polarization,

$$\mathbf{P}_\alpha(r,t) = \mathbf{P}_\alpha^L(r,t) + \mathbf{P}_\alpha^{NL}(r,t) \tag{2.8}$$

into a part that is linear with the electric field

$$\mathbf{P}_\alpha^L(r,t) = \sum_\beta \chi_{\alpha\beta}^1 \, \mathrm{E}_\beta \tag{2.9}$$

and the terms which are nonlinear in the applied field

$$\mathbf{P}_\alpha^{NL}(r,t) = \sum_{\beta\gamma} \chi_{\alpha\beta\gamma}^2 \, \mathrm{E}_\beta \, \mathrm{E}_\gamma + \sum_{\beta\gamma\delta} \chi_{\alpha\beta\gamma\delta}^3 \, \mathrm{E}_\beta \, \mathrm{E}_\gamma \, \mathrm{E}_\delta + \cdots \tag{2.10}$$

This allows one to make a clear distinction between linear and nonlinear optics: If we insert $\mathbf{P}_\alpha^L(r,t)$ into Maxwell's equations, we obtain a description of electromagnetic wave propagation in a crystalline media, described by an electric susceptibility rank-2 tensor $\chi_{\alpha\beta}$, in linear response. By moving the nonlinearity polarization terms to the right hand side of equation 2.5,

$$\nabla^2\mathbf{E} - \nabla\left(\nabla\cdot\mathbf{E}\right) - \frac{1}{c^2}\frac{\partial^2\mathbf{E}}{\partial t^2} - \frac{4\pi}{c^2}\frac{\partial^2\mathbf{P}^L}{\partial t^2} = \frac{4\pi}{c^2}\frac{\partial^2\mathbf{P}^{NL}}{\partial t^2} \tag{2.11}$$

one obtains a wave-equation in which the nonlinear polarization can be viewed as a source term for the linear wave equation. As will be seen subsequently the nonlinear polarization allows one to generate new waves, which will then propagate in the medium according to the linear wave equation.

The lowest nonlinear term involves a rank-3 tensor. Since $\mathbf{P}$ and $\mathbf{E}$ are vectors, and thus are odd under inversion symmetry, χ^2 vanishes in any material that is left invariant under inversion. However, if the symmetry is broken, for example at the interface from one medium to another, or in the case of crystal imperfections, we can also obtain χ^2 localized contributions from centrosymmetric materials. A clear example where this broken of symmetry leads to a high SHG field is the case of *p*Na embedded in a polymeric matrix.

2.4 Ultra-fast laser source

A laser has three major components. An optical resonator (optical cavity), a gain material and a pump source to excite the material in the gain medium. The optical resonator consists of at least two highly reflective mirrors for bouncing the light back and forth resonantly. The mirrors are often spherical mirrors used to confine the light to a stable cavity containing the gain medium that ultimately leads to constructive laser output. One of the end mirrors called an output coupler is made up of a partially reflective material so that a fraction of the light is transmitted providing the laser output. The gain medium contains an active material within the resonator and its function is to amplify light via stimulated emission. Therefore, only the light that bounces back and forth inside an optical resonator is amplified several times in the gain medium to give an intense laser output. Interestingly, the amplified light conserves the phase and direction of the incident light to yield coherent and directional laser output. Coherence is the fundamental property of a laser light. There are two independent forms of coherent light called spatial and temporal coherence.

An ultra-fast laser emits light pulses with durations shorter than one picosecond. Typically, a mechanism modulates the gain of the laser in such a way that light is encouraged to propagate within the cavity in short packets. While the average power can be modest, the peak power can easily reach MWatts or higher values, providing a convenient source to study nonlinear optical phenomena. Typically, the pulse repetition rate of an ultrafast laser is on the order of MHz, but amplifiers with high gain work at much lower repetitions rates.

Subpicosecond duration pulses can be achieved by employing different forms of mode-locking. In the work described in this dissertation, the Kerr lens mode-locking technique is used for generating ultrafast laser pulses.

Mode-locking is an optical technique for producing short light pulses, with durations varying from nanoseconds to femtoseconds. The main function of the technique is impose a constant phase correlation between the several longitudinal cavity modes oscillating in the resonant cavity. Thus, the term of mode-locking is referring to phase locking of the produced modes. To achieve mode-locking the gain bandwidth of the active medium must be sufficiently wide to support multiple cavity modes. The number and amplitude of the locked modes and the frequency spacing between the

modes determines the pulse duration of the laser. Fast laser pulses are very important for studying materials, which require high intensity laser sources and fast temporal probing.

In order to understand how the mode-locking technique works, it is helpful consider a simplified mathematical expression of mode-locking process. Considering that all the oscillating modes resonate at equal amplitude inside the resonating cavity, the electromagnetic field resulting from the superposition of $2n+1$ equally spaced modes with the same amplitude E_0 is given by

$$\mathbf{E}(t) = \sum_{q=-n}^{n} \mathrm{E}_0 \, e^{i\left[(\omega_0 + q\Delta\omega)t + \phi_q\right]} \tag{2.12}$$

where ω_0 is the frequency of the central mode, $\Delta\omega$ is the angular frequency spacing between modes, and ϕ_q is the phase of the q^{th} mode. The above equation corresponds to summation of all possible modes involved. In the case of equal amplitudes (E_0) and locked phases where by the phase of the successive modes are all equal ($\phi_q = \Delta\phi$), the equation reduces to:

$$\mathbf{E}(t) = \mathrm{E}_0 \, e^{i\omega_0 t + i\Delta\phi} \sum_{q=-n}^{n} \mathrm{E}_q \, e^{iq(\Delta\omega t)} \tag{2.13}$$

And this equation can be written as

$$\mathbf{E}(t) = \mathrm{A}(t) e^{i\omega_0 t} \tag{2.14}$$

Where $\mathrm{A}(t)$ is given by

$$\mathrm{A}(t) = \mathrm{E}_0 \, e^{i\Delta\phi} \sum_{q=-n}^{n} e^{iq(\Delta\omega t)} \tag{2.15}$$

Since, q varies from $-n$ to n, the summation at the right side of equation (2.15) contains a geometrical progression. Summing the geometric series leads to the following expression for the laser intensity

$$I(t) \propto \left[\mathrm{A}(t)\right]^2 = \frac{\sin^2\left[(2n+1)\Delta\omega t/2\right]}{\sin^2(\Delta\omega t/2)} \tag{2.16}$$

Equation (2.16) corresponds to a periodic function in which strong peaks emerge in equally spaced manner while very weak peaks appear in between. The time spacing between the pulses or the

period (T) is given by $2\pi/\Delta\omega$ and the pulse duration Δt can be estimated as $2\pi/(2n+1)\Delta\omega = 1/\Delta\nu$ where $\Delta\nu$ is a full frequency width of the oscillating cavity modes.

In a more realistic case, the different mode amplitudes will not be uniform. Assuming for simplicity that $\Delta\phi = 0$, the expression for $\mathrm{A}(t)$ is written as:

$$\mathrm{A}(t) = \sum_{q=-n}^{n} \mathbf{E}_q e^{iq\Delta\omega t} \tag{2.17}$$

Provided that the number of modes is very large and they are closely spaced in frequency the above sum can be treated in the continuum limit as an integration. Further simplifying by assuming the amplitudes decay to zero at the limits of the above sum allows one to take the integration limits to infinity.

$$\mathrm{A}(t) = \int_{-\infty}^{\infty} \mathbf{E}_q e^{iq\Delta\omega t} dq \tag{2.18}$$

Equation (2.18) essentially states that in the time domain, the amplitude of a mode-locked laser is given by the Fourier transform of the amplitude distribution of modes in the frequency domain. For instance, the mode-locking of a continuum of oscillating modes with a Gaussian distribution of amplitude will result in transform limited Gaussian pulses:

$$\mathrm{I}(t) \propto \left[\mathrm{A}(t)\right]^2 \approx e^{-\ln 2\left(\frac{2t}{\Delta\tau_p}\right)^2} \tag{2.19}$$

Where the duration of the pulses is given by

$$\Delta\tau_p = \frac{2\ln 2}{\pi\Delta\nu} = \frac{0.441}{\Delta\nu} \tag{2.20}$$

Note that the pulse width, $\Delta\tau_p$, is once again inversely proportional to the bandwidth, $\Delta\nu$. In practice, several higher order effects such as group velocity dispersion in the gain medium can lead to slightly longer pulses than the transform limit.

The value of $\Delta\nu$ can written in terms of the spread in wavelengths, $\Delta\lambda$ as

$$\Delta\nu = \frac{\Delta\lambda c}{\lambda_0^2} \tag{2.21}$$

where λ_0 the central wavelength and c is the speed of light. For example, the femto-second laser system used in the second harmonic measurements carried out in this dissertation work, was typically adjusted to have a spectral bandwidth of $\Delta\lambda = 12\,nm$ with $\lambda_0 = 800\,nm.$ The corresponding value of $\Delta\nu$ is $5.75\times10^{12}\,s.$ Assuming a sech^2 temporal pulse profile, this leads to a transform limited pulse duration of $\Delta\tau_p = 0.315/\Delta\nu$ or ≈ 96 femtoseconds.

2.5 Second Harmonic Generation

Second harmonic generation (SHG) was the first nonlinear optical effect observed shortly after the invention of the laser, in quartz by Franken et. al. in 1961 [12].

When a medium is exposed to weak light at frequency ω, a polarization density is induced of the form

$$\mathbf{P}(\omega) = \varepsilon_0 \chi^1(-\omega;\omega)\mathrm{E}(\omega) \tag{2.22}$$

where $\chi^1(-\omega;\omega)$ is the practical representation of the linear susceptibility [13]. It has already been shown that polarization density is not just a linear function of the applied electric field $\mathbf{E}$. The linear term is just the first term in the Taylor expansion of $\mathbf{P}$ in $\mathbf{E}$, see equation (2.7). There are a plethora of other terms in the Taylor expansion of $\mathbf{P}$ corresponding to nonlinear effects such as harmonic generation, the Kerr effect, coherent control, and so on. Generally, these effects are only observed using pulsed lasers because the intensity of conventional light sources is too low to significantly excite the higher order polarizations. SHG is one of the simplest nonlinear effect, This is a process whereby a material is illuminated by light at frequency ω and generates light at frequency, 2ω. Mathematically, there is a second order contribution to the polarization density that can be written as

$$\mathbf{P}(2\omega) = \chi^2(-2\omega;\omega,\omega)\mathbf{E}(\omega)\mathbf{E}(\omega) \tag{2.23}$$

where $\chi^2(-2\omega;\omega,\omega)$ is the nonlinear rank-3 tensor associated with second harmonic generation.

2.5.1 Second Order Susceptibilities

The rank-3 tensor associated with second harmonic generation is a matrix with dimensions of 3 × 3 × 3 consisting of 27 elements. However there are several permutation symmetries that impose relations amongst these tensor elements. When the medium is lossless for all frequencies involved, i.e. when the material has no effective memory, one can freely permute the tensor indices, provided the corresponding frequencies are similarly permuted. For example,

$$\chi^{2}_{ikj}\left(\omega_{n+m};\omega_{m},\omega_{n}\right)=\chi^{2}_{kij}\left(\omega_{n};\omega_{m+n},-\omega_{m}\right) \tag{2.24}$$

Physically this states for a transparent medium the process of sum frequency generation, $\omega_{m+n}=\omega_{m}+\omega_{n}$ has the same nonlinear response as the reverse process of difference frequency generation, $\omega_{n}=\omega_{m+n}-\omega_{m}$. Further simplifications can be obtained if the frequency dispersion of the nonlinear susceptibility can be neglected, a condition generally satisfied when all frequencies are well removed from any absorption resonances. This leads to a set known as Kleinman's symmetry where the indices can be permuted freely without altering the corresponding frequencies. In this case, it is no longer necessary to explicitly write the frequency dependence of the susceptibility tensor. For example for second harmonic generation,

$$\chi^{2}_{ijk}\left(2\omega,\omega,\omega\right)=\chi^{2}_{ikj}\left(2\omega,\omega,\omega\right)\ . \tag{2.25}$$

For the case of second harmonic generation, the last two indices can be freely permuted allowing them to be contracted into a more compact notation, that of the so-called d-tensor, which takes the form of a 3x6 matrix with 18 independent elements. The interacting frequencies follow the energy conservation law being $2\omega=\omega+\omega$ where 2ω is SHG frequency. In matrix form, the induced second-order nonlinear polarization, and its dependence on the electric fields are then given by:

$$\mathbf{P}_{i}\left(2\omega\right)=2\varepsilon_{0}d_{ir}\mathbf{E}_{j}\mathbf{E}_{k} \tag{2.26}$$

The Kleinman symmetry implies that the independent element of the *d*-matrix can be reduced using the follows permutation.

$$
\begin{aligned}
d_{15} &= d_{31} = \chi_{xzx} = \chi_{xxz} = \chi_{zxx} \\
d_{16} &= d_{21} = \chi_{xxy} = \chi_{xyx} = \chi_{yxx} \\
d_{24} &= d_{32} = \chi_{yyz} = \chi_{yzy} = \chi_{zyy} \\
d_{26} &= d_{12} = \chi_{yxy} = \chi_{yyx} = \chi_{xyy} \\
d_{34} &= d_{23} = \chi_{zyz} = \chi_{zzy} = \chi_{yzz} \\
d_{35} &= d_{13} = \chi_{zzx} = \chi_{zxz} = \chi_{xzz} \\
d_{36} &= d_{25} = d_{14} = \chi_{zxy} = \chi_{zyx} = \chi_{yzx} = \chi_{yxz} = \chi_{xzy}
\end{aligned}
\tag{2.27}
$$

When evaluating the spatial properties of a specific crystal, the *d*-matrix can almost always be further simplified with several elements vanishing and other being equal. This is an important aspect to take into account when designing SHG devices, since it is useful to access to the highest coefficients in order to have highest conversion efficiency. According to the symmetry of the crystal, the crystal can be classified as being either a triclinic crystal system, monoclinic crystal system, orthorhombic crystal system, quadratic crystal system, trigonal crystal system, hexagonal crystal system, cubic crystal system (or isotopic medium). People already found the susceptibility tensor form of these 7 crystal systems and their 32 crystal classes. Visible, the symmetry is higher; the number of the non-zero tensor element and independent tensor element is less.

For example, the second order d tensor of KDP, belonging to the $\bar{4}2m$ crystal class, takes the form

$$
\begin{pmatrix}
0 & 0 & 0 & d_{14} & 0 & 0 \\
0 & 0 & 0 & 0 & d_{14} & 0 \\
0 & 0 & 0 & 0 & 0 & d_{36}
\end{pmatrix}
\tag{2.28}
$$

In this particular case $d_{36} = 0.39\,\mathrm{pm/V}$ is the largest coefficient. Depending on the propagation direction and polarization of the incident waves, the corresponding electric fields will have different projections onto the crystal's optic axes and often the interaction is described in terms of an effective nonlinear coefficient $\left(d_{eff}\right)$. This coefficient takes into account the projections for a specific experimental configuration.

2.5.2 Wave equation approximation for SHG

In the case of propagation in dielectric media, which do not have any free charges and low magnetic permeability, the Maxwell's equations are then reduced to the wave-equation:

$$\left(\nabla^2 - \frac{1}{c^2}\frac{\partial^2}{\partial t^2}\right)\mathbf{E}(r,t) = \mu_0 \frac{\partial^2}{\partial t^2}\mathbf{P}(r,t) \tag{2.29}$$

where c is the speed of light and μ_0 is the permeability of vacuum. Considering the case of infinite plane wave approximation and unidirectional propagation, the quasi-monochromatic plane waves can be written in the mixed Fourier domain

$$\mathbf{A}(x,\omega) = \frac{1}{2}\sum_{\omega}\left[\mathbf{A}_{\omega}(x)e^{ik_{\omega}x} + c.c.\right] \tag{2.30}$$

Here, ω is the angular frequency of the monochromatic waves and $k_{\omega} = \omega n(\omega)/c$ is the wave vector where $n(\omega)$ is the refractive index as a function of the frequency. The losses are not taken in consideration and c.c. denotes the complex conjugate of the A-fields. The Fourier transform of the wave-equation is

$$\left(\nabla^2 - \frac{\omega^2}{c^2}n^2(\omega)\right)\mathbf{A}(r,t) = \mu_0\omega^2\mathbf{P}_{NL}(r,t) \tag{2.31}$$

Here, by neglecting absorption, only the real part of the refractive index is considered and $\mathbf{P}_{NL}$ contains the higher order susceptibilities. Due to the linear and nonlinear processes, the amplitude, varies over a spatial distance. However, if the amplitude varies slowly over a distance on the order of the wavelength, then it is possible to approximate the above to a first-order wave equation

$$\left|\frac{\partial^2\mathbf{A}(r,t)}{\partial x^2}\right| << \left|k\frac{\partial\mathbf{A}(r,t)}{\partial x}\right| . \tag{2.32}$$

This is usually valid and it is commonly called the slow varying envelope approximation. With this approximation, the wave equation becomes

$$\frac{\partial\mathbf{A}_{\omega}}{\partial x} = \frac{i\mu_0\omega^2}{2k_{\omega}}\mathbf{P}_{\mathrm{NL}}e^{-ik_{\omega}x} \tag{2.33}$$

In the case of the second-order susceptibility, the nonlinear polarization contains the interaction between three waves. The wave equation for the second harmonic field is

$$\frac{\partial \mathbf{A}_{2\omega}}{\partial x} = \frac{i\omega}{n_{2\omega}c} d_{eff} \mathbf{A}_{\omega} \mathbf{A}_{\omega} e^{-i\Delta kx} \tag{2.34}$$

where the phase mismatch is $\Delta k = k_{2\omega} - 2k_{\omega}$. Assuming that the conversion form the incident fundamental wave to the second harmonic field is low, the amplitude of the fundamental wave can be taken to be constant and the above equation can be readily integrated using the initial condition $\mathrm{A}_{2\omega} = 0.$ Then the irradiance of the SHG can be calculated using the magnitude of the Poynting vector, $I = |\mathbf{A}|^2 n\varepsilon_0 c/2$. This results in the following expression for the second harmonic intensity exiting a crystal of length L ,

$$I_{2\omega}(L) = \frac{\varepsilon_0 n_{2\omega} c}{2} |\mathbf{A}_{2\omega}|^2 = \frac{2\omega^2 d_{eff} L^2 I_{\omega}^2}{\varepsilon_0 n_{\omega}^2 n_{2\omega} c^3} \mathrm{sinc}^2 \left[\frac{\Delta kL}{2} \right] \tag{2.35}$$

Where I_{ω} is the intensity of the incident fundamental wave, n_{ω} and $n_{2\omega}$ are the respective refractive indices of the fundamental beam and the second harmonic and $\mathrm{sinc}(\xi) = \sin(\xi)/\xi$. This expression is valid for incident plane waves or at best a loosely focused beam. For more realistic laser beams with a Gaussian transverse profile, the SHG efficiency depends on the beam waist and the optical path length inside the crystal [14,15]. In this case, assuming a focused Gaussian laser beam, the amplitude of the second harmonic beam is given by

$$\frac{\partial \mathrm{A}}{\partial z} = i \frac{\omega}{n_2 c} \chi^{(2)} \mathrm{A}_0^2 \int_{z_0}^{z_0+L} \frac{e^{i\Delta kz'}}{1 + 2iz'/b} dz' \tag{2.36}$$

where $b = kw_0^2$ is the confocal beam parameter of the incident beam with w_0 being the waist radius of the beam. Here z_0 is the position of the entrance to the crystal in relation to the beam waist.

2.5.3 Phase-matching

A fundamental parameter to have a good efficiency of SHG in bulk crystals is the degree of phase-matching [16], which represents the degree to which the propagation vectors of the fundamental

and second harmonic light agree, $\Delta k = k_{2\omega} - 2k_{\omega}$. For an efficient SHG the induced polarizations and their respective waves need to be phase matched, which can be interpreted as the conservation of photon momentum during the second harmonic generation process. If perfect phase-matching occurs $(\Delta k = 0)$ the process will be highly efficient. However, perfect phase-matching is difficult to achieve, since the refractive index usually increases with increasing frequency. In the case of SHG, with $\mathbf{E}_{\omega}$ and $\mathbf{E}_{2\omega}$ polarized in the same direction, the condition that $n(\omega) = n(2\omega)$ is, generally, not possible to obtain and, consequently, the SHG conversion efficiency will be low. From equation 2.36 it can be seen that the intensity at 2ω will oscillate over the crystal length if the phase-mismatch is not zero

$$\Delta k = k_{2\omega} - 2k_{\omega} = \frac{2\omega(n_{2\omega} - n_{\omega})}{c} \neq 0 \tag{2.37}$$

The interpretation of equation is that the driving polarization propagates at a phase velocity of

$$v_{phase}^{\omega} = \left(k_{\omega} / \omega \right)^{-1} \tag{2.38}$$

whereas the generated wave, $\mathbf{A}_{2\omega}$ has the phase velocity of

$$v_{phase}^{2\omega} = \left(k_{2\omega} / 2\omega \right)^{-1} \tag{2.39}$$

Hence, if $\Delta k \neq 0$, after a distance called the coherence length (L_c), the driving polarization and the generated beam will have drifted out of phase by π. At this point back conversion starts and the energy will flow back into the fundamental beam from the second harmonic field. In terms of the phase mismatch, the coherence length is given by

$$L_c = \left| \frac{\pi}{\Delta k} \right| = \left| \frac{\lambda}{4(n_{2\omega} - n_{\omega})} \right| \tag{2.40}$$

In birefringent crystals there are main two types of material phase-matching strategies: type-I is when two fields at ω_1 and ω_2 will have the same polarization, while the third field, at ω_3 is polarized orthogonally with respect to the first two; type-II, is when the two fields at ω_1 and ω_2 are orthogonal. In a uniaxial material, the principal optics axis is commonly along the crystal z-axis

(symmetry axis) and the principal refractive indices are then, $n(x) = n(y) = n_o$ and $n(z) = n_e$ which are called the ordinary and the extraordinary refractive indices, respectively. For a positive uniaxial crystal, $n_o < n_e$, the opposite is the case for a negative uniaxial crystal.

In this work a KDP crystal was used as reference crystal for SHG efficiency calibration. KDP is an efficient second harmonic generator, possessing a large nonlinear coefficient, being transparent from 0.365 μm to approximately 4.3 μm, and having a high damage threshold. For frequency conversion in the visible, KDP is an appropriate choice. KDP is a negative uniaxial crystal with normal dispersion. For example, for the fundamental beam at $800\,nm$ the respective indices are $n_e = 1.466$ and $n_o = 1.506$, while for SHG the respective indices becomes $n_e = 1.487$ and $n_o = 1.534.$ Thus the birefringence is sufficient to compensate for the refractive index dispersion and KDP can be used in a type I phase matching scheme with the fundamental light input as an ordinary wave.

2.6 Nanophotonics

Nanophotonics occupies the area where photonics, the science that involves the control of photons in free space or in matter, merges with nanoscience and nanotechnology. The related light–matter interactions can be generation, transmission, modulation and detection of photons in confined structures at a nanoscale [5,17–20]. The future and success of photonic technologies will require the discovery of new optical materials and the miniaturization of optoelectronic devices that feature better performance, low cost and low power consumption.

One application that is easy to visualize is a photonic chip that controls or modulates incoming light signals as efficiently as possible [21], [22]. A minuscule laser on a chip with a large tuning bandwidth allows the user the freedom to adjust the frequency accordingly to optimize the modulation. However, the technical difficulties associated with this goal are tremendous. In this aspect, NLO can be used to generate new frequencies and increasing the operating bandwidth of the device. The Spaser (surface plasmon amplification by stimulated emission of radiation) has be singled out as a possible candidate. Its characteristic of a nanoscopic quantum generator of

localized surface plasmons able to generate, in a single mode and with a very high spectral density and intensity, extreme electromagnetic fields in a small volume capable of pumping a gain medium at the nanoscale [23]. The number of potential applications of the spaser is enormous in science, in industry and, especially, in healthcare because their nanoscopic sizes and emission frequencies can be matched to those of biomolecules. However, current plasmonic devices suffer from high losses associated with the metals used, heating, and incompatibility with complementary metal oxide semiconductor fabrication processes, among other problems. To overcome such limitations high-index nanophotonic structures complement or can even replace different plasmonic components in a range of applications [24]. High-index dielectric structures can be employed as new building blocks to obtain unique functionalities. This is one example of the development of nanoscale optical physics that has recently led to a new branch of nanophotonics.

Assembling nanomaterials as a building blocks into a clever, functional and highly integrated 2D or 3D heterogeneous material systems with a high angular, spatial or temporal precision for emitting photons, is a promising future possibility for light matter manipulation [25]. Such nanomaterials offer unique opportunities for reducing the dissipative losses, enlarging resonance interactions and enhancing the near field amplitudes of both electric and magnetic fields.

2.7 Organic compounds

Organic compounds are compounds based on carbon and often contain several other low atomic number elements like hydrogen, oxygen, nitrogen, sulfur, phosphorus, and halogens like chlorine, bromine, fluorine or iodine. Based on their size, organic compounds are mainly divided into two classes: molecules (short chain) and polymers (long chain) molecules. Organic materials have salient features, including a low cost in terms of both materials and processing equipment, the simplicity and high-throughput of their fabrication, as well as the ease of modification of their chemical structure compared to their inorganic equivalents, being inherent tunable by chemical synthesis techniques. These features are very attractive and convenient for engineering materials with optical properties. Chemically grown is an unique process with exceptional advantages, such as, the capability to grow single crystals, relatively defect free with atomically smooth surfaces.

Organic nanomaterials, are promising building blocks for integrated photonic devices [26–28]. Their easy processability, plastic properties combined with desirable optical properties, including

large optical cross-sections and wide spectral tunability, make them strong prospects to contribute to the development of flexible photonics and the realization of nanophotonic circuits for next-generation optical information processing.

The first generation of molecular engineering studies whereby a one-dimensional dipolar donor-acceptor conjugated system had served, since the early 1970s, as a universal template has led to strong molecular responses [8,9,29]. Various optimization methods have been proposed: increase of the donor or acceptor strength, modification of the electronic structure of the conjugated path, or adequate combinations of the end donor, or acceptor groups, with the conjugated bridge. In 1970s and the 1980s it is well known that the second order nonlinear optical response of the organic compounds is a function of the length of the conjugated π-system and the strength of the donor and acceptor [29]. However, it has proven difficult to incorporate these molecules at high density into noncentrosymmetric structures capable of providing a second order nonlinear response. At the time, much of the research was focused on engineering dipolar crystalline materials. Several milestones were achieved like as 3-methyl-4-nitropyridine-1-oxide (POM) [30], N-(4-nitrophenyl)-(L)-prolinol (NPP) [31] and *trans*-4-[4-(dimethylamino)-*N*-methylstilbazolium] *p*-tosylate (DAST) [32].

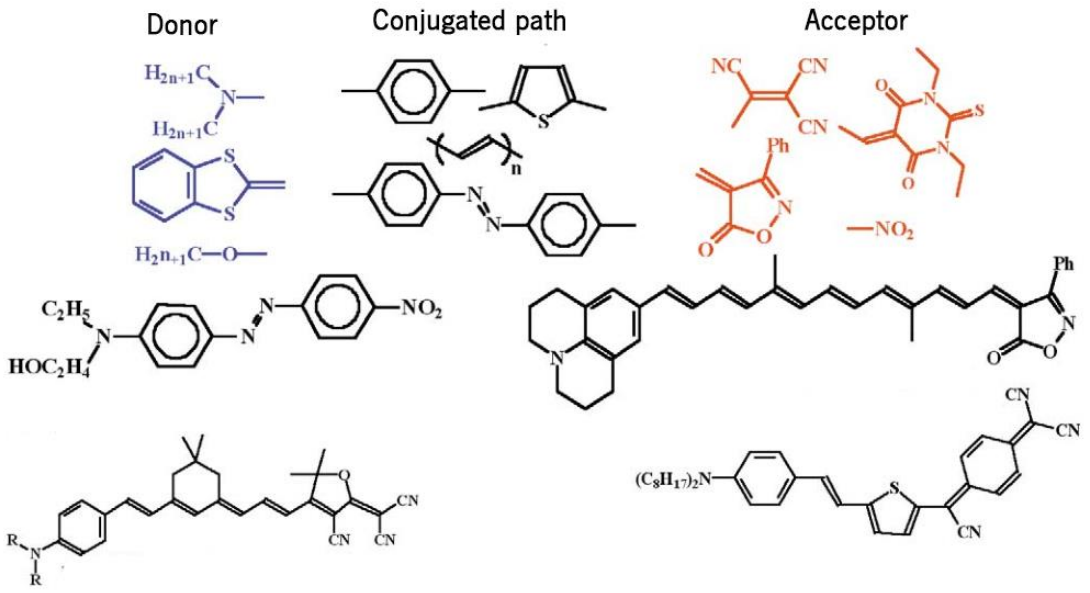

Figure 1 – Examples of donor, conjugated path and acceptor groups. Optimization of the second order nonlinear coefficient are done by the combination of the best conjugation path together with donor and acceptor groups.

Dalton and his collaborators have shown that the residual dipole-dipole interactions among chromophores makes it extremely difficult to achieve a high degree of noncentrosymmetric order in doped polymer devices, unless the undesirable spatially anisotropic intermolecular electrostatic interactions are minimized by a modification of the shape of chromophores to sterically inhibit such interactions [33]. Typically, the active organic molecules were embedded in a polymeric material heated to above the glass transition point and a strong electric field was used to orientate the molecules to reach noncentrosymmetric structures in a viscous phase that was then locked in upon cooling [33,34]. However, the nonlinear response of the majority of materials fabricated in this was relax over a timescale of weeks to months.

Since the early years of 1990 until now the organic molecular engineering has been advancing for example by developing octupolar systems whereby the symmetry-imposed cancellation of the dipole moment precludes the molecules to organize in a centrosymmetric order [35–37]. In the early 1990s, the first experimental evidence of frequency doubling is observed in the 1,3,5-trinitro-2,4,6-triaminobenzene (TATB) [38].

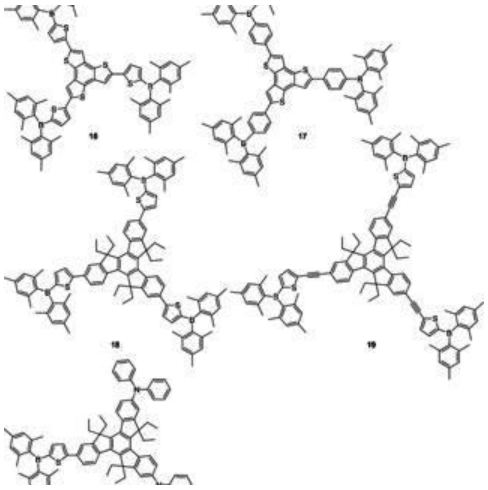

Figure 2 – Representative exemples of octupolar systems.

However, coupling of preferably large molecular dipoles to an externally applied electric field, is not applicable to octupolar molecules which are deliberately deprived of dipole moments. Structures based on two-dimensional (2D) and three-dimensional (3D) multipolar arrangements of alternating donor and acceptor groups interacting via adequately defined conjugated backbones and have been shown to lead to giant nonlinearities [39–43]. Optimization at the molecular level has shown great progress in these systems as exemplified by well established structure-property relationship for two-dimensional octupoles and the development of highly efficient molecules [44,45].

Novel π-conjugated polymers are now promising materials because of their several advantages, like semiconductor-like properties, high absorption cross-section, and broad emission spectra, which can overlap with a large variety of organic chromophores and polymers, attractive features for suitability of hybrid integration. π-conjugated polymers is basically a multi chromophoric system, and each subunit acts as a chromophore [46,47]. These hybrid structures have a delocalized π-electrons along the carbon backbone, which are easily polarizable as useful property to many organic nanophotonic systems.

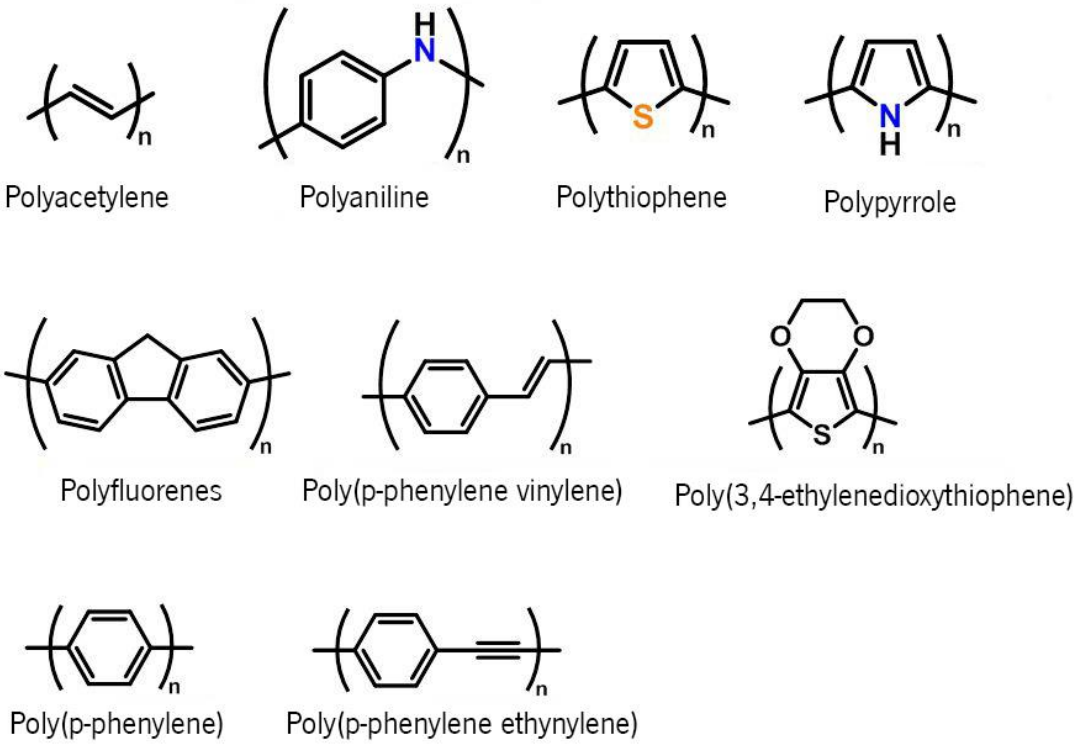

Figure 3 – Examples of several backbones of π-conjugated polymers

SHG often has a dipolar origin that cannot exist in a medium possessing inversion symmetry. A material with an inversion of symmetry is known as centrosymmetric. The explanation is simple since $\mathbf{P}$ and $\mathbf{E}$ are both vectors that change sign under inversion equation 2.12 stipulates that for a second order response to exist the second order susceptibility must change signs under inversion. However, in centrosymmetric materials, all physical properties remain unchanged by inversion. Hence, the bulk second order susceptibility of a centrosymmetric material must vanish.

Nevertheless, there are many ways to obtain SHG from materials with inversion symmetry, for example by breaking the inversion symmetry of the material using different strategies to avoid the centrosymmetric structure[39,41,43,48,49]. In a natural way, inversion symmetry is broken at the

surface layer of the material, that is, at any interfaces between the centrosymmetric material and other materials [49,50]. Therefore, a two-dimensional second harmonic polarization sheet exists at interfaces where the SHG is allowed. There is also a bulk quadrupole source, whereby an electric quadrupole density (rather than an electric dipole density) is generated in the medium at the second harmonic frequency, as well as a magnetic dipole source, whereby a magnetic dipole density is generated at 2ω [51]. Surface dipolar, and bulk quadrupole/magnetic contributing for dipolar SHG are allowed for any crystal system, and they are the main sources of weak second harmonic light in centrosymmetric media when there are no external influences acting on the medium.

For long time, all major efforts in crystal engineering of molecular organic with enhanced quadratic nonlinear properties have been focused on developing efficient shape-engineered chromophores and increasing polar order through careful control of the nanoscale architecture of macromolecules [52]. They has so far been almost exclusively based on the paradigm ''molecular dipole'' of the simplest dipolar and octupolar extensions of *para*-nitroaniline (*p*Na).

2.8 *para*-Nitroaniline

A feature common of many of the organic systems presented in the previous section is their relation with the underlying basic polar *p*Na pattern. With a single pair of donor–acceptor substituents interacting through a π-electron conjugated linkage serving as a polarizable electron reservoir, *p*Na is the simplest polar organic compounds with chemical formula $NO_2C_6H_4NH_2$. It consists of a benzene ring with the electron-donor amino group (NH_2) and the electron-acceptor nitro group (NO_2) attached in a linear geometry to the two carbon atoms leading to an unsaturated bridge and a delocalized π-electron system. The delocalization of the π-electrons leads to an asymmetric charge distribution resulting in a strong molecular optical nonlinearity [53].

Polar organic compounds are, inherently, good candidates for SHG applications. They have several advantages compared to their inorganic counterparts including high optical nonlinearities, fast response time, high damage threshold and ease of design and fabrication. Despite the exceptional molecular nonlinear optical response of *p*Na it crystallizes in a centrosymmetric space group $P2_1/n$, which impedes the observation of any macroscopic second-order nonlinear effect. The

principal properties of *p*Na crystal are the very weak electric conductivity, strong third order nonlinear optical properties. It also possesses an anomaly at 140K corresponding to a sign reversal in a pyroelectric coefficient[2]. Finally it displays strong couplings in vibrational spectra, which turn out to be analogous to electron-phonon couplings in other charge transfer complexes [54–58].

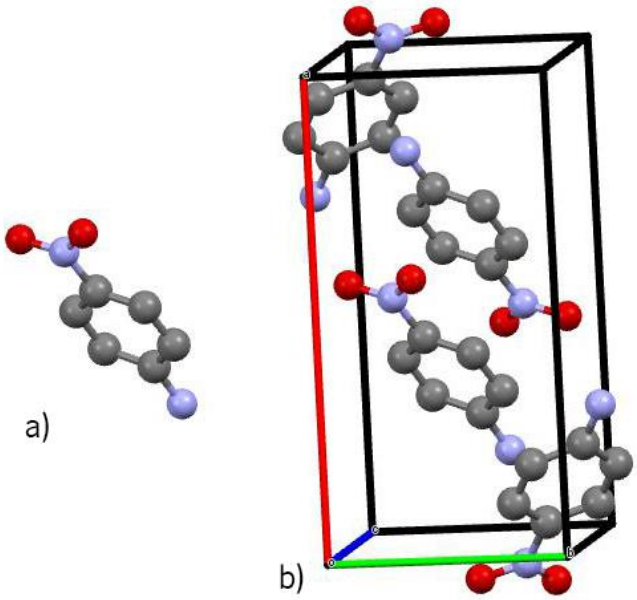

Figure 4 – Schematic representation of pNa structure a) and the respective unitary crystal cell b). The colours red and blue represent the oxygen and the nitrogen atoms, respectively.

As mentioned, the inherent polar nature of *p*Na molecules exhibiting significant ground state dipole moments projecting a large charge-transfer between donor and acceptor group. The consequence is to favor dipole–dipole interactions that frustrate the structural goal of engineering noncentrosymmetric structures for second order nonlinear optics. This problem has been identified since the early eighties. Since then, several schemes have been successfully proposed and implemented to diminish either the dipole–dipole forces or conversely build-up structures based on more energetic interactions which will surpass and hence get around the influence of dipole interactions [39,41,48,49,59–62].

Methods for the control of bulk dipolar arrangement of organic molecules, including *p*Na, into acentric environments have been restricted to thin film structures. The main techniques are the Langmuir-Blodgett technique, guest-hosts approach and orientation of molecules in polymer glasses, or liquid-crystalline, using strong electric or magnetic fields. A promising method is the

[2] Pyroelectricity is interpreted as the ability of certain materials to generate electric potential energy when they are heated or cooled.

guest-hosts approach where a polarizable material, whose natural crystal habit may be centrosymmetric (thus unable to produce SHG) can be induced to exhibit SHG by inclusion into a host matrix which works as a polar director to align the molecular dipoles. The use of inclusion compound hosts appears, surprisingly, to be a general method for dipolar alignment of organic compounds [60,63–65].

The most important message from table 1 is that guest molecules are completely separated from each other to avoid molecular centrosymmetric aggregation, which has a beneficial effect for the NLO activity. In the 28 examples listed in Table 1, only four failed to exhibit SHG. Statistically, 80% of the polar organic compounds crystallize in a centrosymmetric group. With this approach, statistically, the occurrence of polar noncentrosymmetric structures increases to 85%. Besides, it is convenient to modulate the NLO properties of supramolecular materials by controlling the host–guest inclusion process.

Another approach extensively studied to overcome the natural centrosymmetric structure of the organic chromophores, including *p*Na, is the electric field poling. The most common poling configurations are contact electrode poling where a high electrical potential are applied between the two electrodes that are in direct contact with the material solution[66,67]. These electrodes can be oriented in-plane, where the poling axis is parallel to the device surface, or vertically, where the poling axis is normal to the device surface. A uniform field is very important in electrical poling method in order to obtain molecular organizations with desirable NLO properties. The presence of film non-uniformity caused by impurities or inhomogeneity can lower the value of the maximum poling field that can be applied before damage occurs. In homogeneities may also change the spatial profile of the effective poling field causing local fluctuations in chromophore order.

Among the progress previously reported in nonlinear molecular engineering for efficient SHG crystals, *p*Na shows some of the most promising values reuslts SHG. In fact *p*Na is a paradigmatic molecule and has be the subject of a multitude of both experimental and theoretical studies. For example, Munn and his co-works have focused on determining the surface response that might explain the unusually strong SHG detected from the certain locations along the (101) cleavage plane of a *p*Na crystal [50].

Guest	Host:Guest Ratio	SHG relative to urea
Inclusion Compounds with β-Cyclodextrin		
p-Nitroaniline	1:1	2.0-4.0
p-(N,N-imethylamino)cinnamaldehyd	1:1	0.4
N-methyl-*p*-nitroaniline	1:1	0.25
2-amino-5-nitropyridine	1:1	0.07
p-(dimethylamino)benzonitrile	1:1	0.015
Inclusion Complexes with Thiourea		
benzenechromium tricarbonyl	3:1	2.3
(fluorobenzene)chromium tricarbonyl	3:1	2.0
(cyclopentadieny1)rhenium tricarbonyl	ND	0.5
(1,3-cyclohexadiene)iron tricarbonyl	3:1	0.4
(1,3-cyclohexadienyl)manganese tricarbonyl	3:1	0.4
(trimethy1enemethane)iron tricarbonyl	3:1	0.3
(cyclopentadieny1)manganese tricarbonyl	3:1	0.3
(1,3-butadiene)iron tricarbonyl	ND	1.0
pyrrolylmanganese tricarbonyl	ND	0.2
(cyclopentadieny1)dicarbonylnitrosyl- chromium	3:1	0.1
(cyclopentadien y1)diethylenerhodium	ND	0.0
(cyclopentadienyl)(1,3-cyclohexadiene)cobalt	3:1	0.0
(cyclopentadienyl)ethylenetetrafluoroethylen-erhodium	ND	0.0
Inclusion Complexes with Tris(o-thymotide)		
p-(dimethy1amino)cinnamaldehyde	2:1	1.0
p-(dimethy1amino)benzonitrile	2:1	0.2
(*p*-cyanobenzoyl)manganese pentacarbonyl	ND	0.2
(indane)chromium tricarbonyl	1:1	0.1
(anisole)chromium tricarbonyl	ND	0.1
(tetra1in)chromium tricarbonyl	1:1	0.1
benzenemanganese tricarbonyl-tetrafluoroborate	ND	0.1
(pyridine)tungsten pentacarbonyl	2:1	0
Inclusion Complexes with Deoxycholic Acid		
p-nitroaniline	ND	1.0
4-(dicyanomethylene)-2-methy-6-(p-(dimethylamino)styryl)-4*H*-pyran	ND	0.4
Errors in powder SHG intensity measurements can be *50% because of particle size differences among samples, but relative rankings within a series are probably correct. ND = not determined.		

Table 1 - Relative Second-Harmonic generation capabilities of several host-guest complexes, based on the publication [65].

In a previous work carried out within our research group, electrospun poly(ethylene oxide) (PEO) and poly(vinyl alcohol) (PVA) nanofiber matrices were used to embed and align the well-known organic molecule urea, which can generate significant SHG[68]. Additionally, they used the same technique to align the push-pull molecule of 2-methyl-4-nitroaniline (*M*NA) molecules using poly(L-lactic acid) (PLLA) as a host [69,70]. *M*Na is one of the few push-pull molecules that have a natural noncentrosymetric crystal form with a strong SHG [71]. In these studies, they discovered that in the PEO matrix, the urea molecules combine with the matrix forming an inclusion complex with an orthorhombic unit cell; while in PVA matrix, the urea molecules maintain the same tetragonal unit cell as seen in its bulk crystals, forming one-dimensional crystalline cores embedded within the electrospun nanofibers. The SHG polarizations are different in both matrices. In the case of PEO/urea nanofiber arrays, the resultant polarization of the SHG as a function of the excitation polarization is nearly independent of the analyser orientation, indicating a poor molecular orientation. Conversely, the polarization dependence of the SHG response of the PVA/urea aligned fibres array reveals a strong orientation of the active molecules along the fibres. Furthermore, in the approach using *M*Na, optical measurements suggest that the SHG signals from the uniaxial aligned PLLA/*M*Na nanofiber arrays are strongly dependent on the polarization direction of the fundamental beam, as well, as the analyser. The powder diffraction X-ray spectra indicates that the *M*Na molecules crystallize within the electrospun nanofibres in a common orientation similar to bulk crystals, in the monoclinic I_a space group. The individual molecular dipole moments are parallel to each other lying in the (010) plane leading to a strong net dipole moment of the unit cell. By comparing the SHG signal from the PLLA/MNa fiber with that from a Maker fringe measurement on a (110) cut KDP crystal, the value for the effective nonlinear coefficient of the PLLA/*M*Na nanofibers was determined to be greater than that of bulk *M*Na crystals.

After the observation of these astonishing results, the research group decided to explore the potential of the same approach to overcome the centrosymmetric nature of several organic push-pull molecules. In this way, we hoped to provide a starting point for a better comprehension of the mechanisms involved, and contribute a new pathway for organic crystal engineering. Applying the same electrospinning approach, but using *p*Na molecules embedded in a Poly(methyl methacrylate) (PMMA) matrix resulted in a strong and unusual SHG rising from the PMMA/*p*Na nanofibres [48]. PMMA is the most versatile polymer for electrospun nanofibres in same way *p*Na is the simple push-pull molecules.

2.9 Bibliography

1. L. Novotny and N. Van Hulst, "Antennas for light," Nat. Photonics **5**(2), 83–90 (2011).
2. N. Xi and K. Lai, *Nano Optoelectronic Sensors and Devices* (Elsevier, 2012).
3. M. L. Juan, M. Righini, and R. Quidant, "Plasmon nano-optical tweezers," Nat. Photonics **5**(6), 349–356 (2011).
4. D. H. Lien, J. S. Kang, M. Amani, K. Chen, M. Tosun, H. P. Wang, T. Roy, M. S. Eggleston, M. C. Wu, M. Dubey, S. C. Lee, J. H. He, and A. Javey, "Engineering light outcoupling in 2D materials," Nano Lett. **15**(2), 1356–1361 (2015).
5. V. J. Sorger, N. D. Lanzillotti-Kimura, R. M. Ma, and X. Zhang, "Ultra-compact silicon nanophotonic modulator with broadband response," Nanophotonics **1**(1), 17–22 (2012).
6. N. Youngblood and M. Li, "Integration of 2D materials on a silicon photonics platform for optoelectronics applications," Nanophotonics **6**(6), 1205–1218 (2017).
7. I. Ledoux and J. Zyss, "Polar and Non-Polar Organic Molecules, Crystals and Langmuir-Blodgett Films for Quadratic Nonlinear Optics," in *Organic Molecules for Nonlinear Optics and Photonics* (1991), **194**, pp. 81–103.
8. F. Kajzar, J. Messier, D. S. Chemla, and J. Zyss, "Nonlinear Optical Properties of Organic Molecules and Crystals," by DS Chemla J. Zyss, Acad. Press. New York **1**, 51 (1987).
9. G. S. He, L. Yuan, N. Cheng, J. D. Bhawalkar, P. N. Prasad, L. L. Brott, S. J. Clarson, and B. A. Reinhardt, "Nonlinear optical properties of a new chromophore," J. Opt. Soc. Am. B **14**(5), 1079 (1997).
10. H. Kobayashi and M. Kotani, "Observation of Generation of Intense Second-Harmonics at Etch Pits of p - Nitroaniline Single Crystal Surface," Mol. Cryst. Liq. Cryst. Sci. Technol. Sect. A. Mol. Cryst. Liq. Cryst. **278**(1), 125–130 (1996).
11. D. Epperlein, B. Dick, G. Marowsky, M. Chemie, and A. Laserphysik, "Second-Harmonic Generation in Centro-Symmetric Media," **10**, 5–10 (1987).
12. P. A. Franken, A. E. Hill, C. W. Peters, and G. Weinreich, "Generation of optical harmonics," Phys. Rev. Lett. **7**(4), 118–119 (1961).
13. R. W. Boyd, *Nonlinear Optics* (2003).
14. H. Wang and A. M. Weiner, "Efficiency of Short-Pulse Type-I Second-Harmonic Generation With Simultaneous Spatial Walk-Off, Temporal Walk-Off, and Pump Depletion," IEEE J. Quantum Electron. **39**(12), 1600–1618 (2003).
15. T. R. Zhang, H. R. Choo, and M. C. Downer, "Phase and group velocity matching for second harmonic generation of femtosecond pulses.," Appl. Opt. **29**(27), 3927–3933 (1990).
16. A. M. Weiner, "Effect of Group Velocity Mismatch on the Measurement of Ultrashort Optical Pulses via Second Harmonic Generation," IEEE J. Quantum Electron. **19**(8), 1276–1283 (1983).
17. J. A. Schuller, E. S. Barnard, W. Cai, Y. C. Jun, J. S. White, and M. L. Brongersma, "Plasmonics for extreme light concentration and manipulation," Nat. Mater. **9**(3), 193–204 (2010).
18. D. K. Gramotnev and S. I. Bozhevolnyi, "Plasmonics beyond the diffraction limit," Nat. Photonics **4**(2), 83–91 (2010).
19. N. Xi and K. Lai, *Nano Optoelectronic Sensors and Devices* (2012).
20. F. S. Kim, G. Ren, and S. A. Jenekhe, "One-dimensional nanostructures of π-conjugated molecular systems: Assembly, properties, and applications from photovoltaics, sensors, and nanophotonics to nanoelectronics," Chem. Mater. **23**(3), 682–732 (2011).

21. A. Reinhard, T. Volz, M. Winger, A. Badolato, K. J. Hennessy, E. L. Hu, and A. Imamoğlu, "Strongly correlated photons on a chip," Nat. Photonics **6**(2), 93–96 (2012).

22. L. Li, Y. O. Dudin, and A. Kuzmich, "Entanglement between light and an optical atomic excitation," Nature **498**(7455), 466–469 (2013).

23. N. I. Zheludev, S. L. Prosvirnin, N. Papasimakis, and V. A. Fedotov, "Lasing spaser," Nat. Photonics **2**(6), 351–354 (2008).

24. M. I. Stockman, "Spaser Action, Loss Compensation, and Stability in Plasmonic Systems with Gain," Energy **156802**(2), 4 (2010).

25. M. A. Boles, M. Engel, and D. V. Talapin, "Self-assembly of colloidal nanocrystals: From intricate structures to functional materials," Chem. Rev. **116**(18), 11220–11289 (2016).

26. Y. S. Zhao, H. Fu, A. Peng, Y. Ma, D. Xiao, and J. Yao, "Low-dimensional nanomaterials based on small organic molecules: Preparation and optoelectronic properties," Adv. Mater. **20**(15), 2859–2876 (2008).

27. Y. Guo, L. Xu, H. Liu, Y. Li, C. M. Che, and Y. Li, "Self-Assembly of functional molecules into 1D crystalline nanostructures," Adv. Mater. **27**(6), 985–1013 (2015).

28. S. Ahmad, "Organic semiconductors for device applications: Current trends and future prospects," J. Polym. Eng. **34**(4), 279–338 (2014).

29. G. Chen and S. Mukamel, "Nonlinear Susceptibilities of Donor—Acceptor Conjugated Systems: Coupled-Oscillator Representation," J. Am. Chem. Soc. **117**(17), 4945–4964 (1995).

30. M. Sigelle and R. Hierle, "Determination of the electrooptic coefficients of 3-methyl 4-nitropyridine 1-oxide by an interferometric phase-modulation technique," J. Appl. Phys. **52**(6), 4199–4204 (1981).

31. I. Ledoux, C. Lepers, A. Périgaud, J. Badan, and J. Zyss, "Linear and nonlinear optical properties of N-4-nitrophenyl L-prolinol single crystals," Opt. Commun. **80**(2), 149–154 (1990).

32. F. Pan, G. Knöpfle, C. Bosshard, S. Follonier, R. Spreiter, M. S. Wong, and P. Günter, "Electro-optic properties of the organic salt 4-N,N-dimethylamino-4′-N′-methyl-stilbazolium tosylate," Appl. Phys. Lett. **69**(1), 13–15 (1996).

33. L. R. Dalton, A. W. Harper, R. Ghosn, W. H. Steier, M. Ziari, H. Fetterman, Y. Shi, R. V. Mustacich, A. K. Y. Jen, and K. J. Shea, "Synthesis and Processing of Improved Organic Second-Order Nonlinear Optical Materials for Applications in Photonics," Chem. Mater. **7**(6), 1060–1081 (1995).

34. L. R. Dalton, L. P. Yu, M. Chen, L. S. Sapochak, and C. Xu, "Recent advances in the synthesis and characterization of nonlinear optical materials: second-order materials," Synth. Met. **54**(1–3), 155–160 (1993).

35. M. Blanchard-Desce, J. B. Baudin, L. Jullien, R. Lome, O. Ruel, S. Brasselet, and J. Zyss, "Towards highly efficient nonlinear optical chromophores: molecular engineering of octupolar molecules," Opt. Mater. (Amst). **12**(2), 333–338 (1999).

36. J. Zyss, "Molecular engineering implications of rotational invariance in quadratic nonlinear optics: From dipolar to octupolar molecules and materials," J. Chem. Phys. **98**(9), 6583–6599 (1993).

37. S. Brasselet, F. Cherioux, P. Audebert, and J. Zyss, "New octupolar star-shaped strucures for quadratic nonlinear optics," Chem. Mater. **11**(7), 1915–1920 (1999).

38. H. S. Nalwa, T. Watanabe, and S. Miyata, "A comparative study of 4-nitroaniline, 1,5-diamino-2,4-dinitrobenzene and 1,3,5-triamino-2,4,6-trinitrobenzene and their molecular engineering for second-order nonlinear optics," Opt. Mater. (Amst). **2**(2), 73–81 (1993).

39. L. Werner, J. Caro, G. Finger, and J. Kornatowski, "Optical second harmonic generation (SHG) on p-nitroaniline in large cyrstals of AlPO4-5 and ZSM-5," Zeolites **12**(6), 658–663 (1992).

40. R. Vallée, P. Damman, M. Dosière, E. Toussaere, and J. Zyss, "Nonlinear optical properties and crystalline orientation of 2-methyl-4- nitroaniline layers grown on nanostructured poly(tetrafluoroethylene) substrates," J.

Am. Chem. Soc. **122**(28), 6701–6709 (2000).

41. T. Miyazaki, T. Watanabe, and S. Miyata, "Highly efficient second harmonic generation in p-nitroaniline/poly(lactone) systems," Jpn. J. Appl. Phys. **27**(9 A), L1724–L1725 (1988).

42. L. Werner, J. Caro, and G. Finger, "Optical second harmonic generation (SHG) on p-nitroaniline in large crystals of AlPO.hlf.4.rhlf.-5 and ZSM-5," Zeolites **12**, 658–663 (1992).

43. M. Kato, M. Kiguchi, N. Sugita, and Y. Taniguchi, "Second-Order Nonlinearity of Mixtures Including p-Nitroaniline Derivatives," Nonlinearity **5647**(97), 8856–8859 (1997).

44. J. Zyss and S. Brasselet, "Multipolar Symmetry Patterns in Molecular Nonlinear Optics," J. Nonlinear Opt. Phys. Mater. **07**(03), 397–439 (1998).

45. J. Zyss, C. Dhenaut, I. Samuel, I. Ledoux, M. Bourgault, and H. Le Bozec, "Giant octupolar nonlinearity in chiral donor-acceptor organometallic systems," in *Proceedings of the International Quantum Electronics Conference (IQEC'94)* (1994).

46. L. Yu, M. Chen, and L. R. Dalton, "Ladder Polymers: Recent Developments in Syntheses, Characterization, and Potential Applications as Electronic and Optical Materials," Chem. Mater. **2**(6), 649–659 (1990).

47. I. Ledoux and J. Zyss, "Molecular engineering of molecules and materials for quadratic nonlinear optics," Comptes Rendus Phys. **3**(4), 407–427 (2002).

48. D. V. Isakov, M. S. Belsley, E. De Matos Gomes, H. Gonçalves, P. Schellenberg, and B. G. Almeida, "Intense optical second harmonic generation from centrosymmetric nanocrystalline para-nitroaniline," Appl. Phys. Lett. **104**(18), 181903 (2014).

49. H. Kobayashi and M. Kotani, "Study of single crystal surface with second-harmonic generation: P-nitroaniline," Mol. Cryst. Liq. Cryst. Sci. Technol. Sect. A. Mol. Cryst. Liq. Cryst. **252**(1), 277–281 (1994).

50. M. Malagoii and R. W. Munn, "Microscopic calculation of surface-induced second-harmonic generation in crystals of para-nitroaniline," J. Chem. Phys. **112**(15), 6757–6762 (2000).

51. G. J. Ashwell, G. Jefferies, D. G. Hamilton, D. E. Lynch, M. P. S. Roberts, G. S. Bahra, and C. R. Brown, "Strong second-harmonic generation from centrosymmetric dyes," Nature **375**(6530), 385–388 (1995).

52. K. Clays and B. J. Coe, "Design strategies versus limiting theory for engineering large second-order nonlinear optical polarizabilities in charged organic molecules," Chem. Mater. **15**(3), 642–648 (2003).

53. S. J. Lalama and A. F. Garito, "Origin of the nonlinear second-order optical susceptibilities of organic systems," Phys. Rev. A **20**(3), 1179–1194 (1979).

54. T. Gunaratne, J. R. Challa, and M. C. Simpson, "Energy flow in push-pull chromophores: vibrational dynamics in para-nitroaniline," ChemPhysChem **6**(6), 1157–1163 (2005).

55. M. Harrand, "Raman study on para nitroaniline single crystal. II: Internal Vibrations," J. Raman Spectrosc. **4**(1), 53–73 (1975).

56. J. Xia, L. Zhu, Y. Feng, Y. Li, Z. Zhang, L. Xia, L. Liu, and F. Ma, "Unusual Raman spectra of para-nitroaniline by sequential Fermi resonances," Spectrochim. Acta - Part A Mol. Biomol. Spectrosc. **120**(2), 616–620 (2014).

57. M. Harrand, "Raman study on p-nitroaniline: Molecular structure in the molten phase," J. Raman Spectrosc. **8**(3), 161–164 (1979).

58. T. Asaji and A. Weiss, "Pyroelectricity of Molecular Crystals: Benzene Derivatives," Zeitschrift fur Naturforsch. - Sect. A J. Phys. Sci. **40**(6), 567–574 (1985).

59. L. Zhang and D. Cui, "Investigation of second-harmonic generation and molecular orientation in electrostatically self-assembled thin films," Polymers (Basel). **3**(3), 1297–1309 (2011).

60. J. Xu, S. Semin, T. Rasing, and A. E. Rowan, "Organized chromophoric assemblies for nonlinear optical materials: Towards (Sub)wavelength scale architectures," Small **11**(9–10), 1113–1129 (2015).

61. H. Goncalves, I. Saavedra, R. A. S. Ferreira, P. E. Lopes, E. De Matos Gomes, and M. Belsley, "Efficient second harmonic generation by para-nitroaniline embedded in electro-spun polymeric nanofibres," J. Phys. D. Appl. Phys. **51**(10), (2018).

62. M. Kato, M. Kiguchi, N. Sugita, and Y. Taniguchi, "Second-Order Nonlinearity of Mixtures Including p-Nitroaniline Derivatives," Nonlinearity **5647**(97), 8856–8859 (1997).

63. F. Marlow, W. Hill, J. Caro, and G. Finger, "Raman-Study on P-Nitroaniline in Channels of the Molecular-Sieve Alpo(4)-5," J. Raman Spectrosc. **24**(9), 603–608 (1993).

64. S. Cambré, J. Campo, C. Beirnaert, C. Verlackt, P. Cool, and W. Wenseleers, "Asymmetric dyes align inside carbon nanotubes to yield a large nonlinear optical response," Nat. Nanotechnol. **10**(3), 248–252 (2015).

65. D. F. Eaton, A. G. Anderson, W. Tam, and Y. Wang, "Control of Bulk Dipolar Alignment Using Guest-Host Inclusion Chemistry: New Materials for Second-Harmonic Generation," J. Am. Chem. Soc. **109**(6), 1886–1888 (1987).

66. S. Di Bella, G. Lanza, I. Fragalà, S. Yitzchaik, M. A. Ratner, and T. J. Marks, "Charge distribution and second-order nonlinear optical response of charged centrosymmetric chromophore aggregates. An ab initio electronic structure study of p-nitroaniline dimers," J. Am. Chem. Soc. **119**(13), 3003–3006 (1997).

67. D. M. Burland, R. D. Miller, and C. A. Walsh, "Second-Order Nonlinearity in Poled-Polymer Systems," Chem. Rev. **94**(1), 31–75 (1994).

68. D. Isakov, E. De Matos Gomes, M. Belsley, B. Almeida, A. Martins, N. Neves, and R. Reis, "High nonlinear optical anisotropy of urea nanofibers," Epl **91**(2), (2010).

69. D. V. Isakov, E. De Matos Gomes, L. G. Vieira, T. Dekola, M. S. Belsley, and B. G. Almeida, "Oriented single-crystal-like molecular arrangement of optically nonlinear 2-methyl-4-nitroaniline in electrospun nanofibers," ACS Nano **5**(1), 73–78 (2011).

70. D. Isakov, E. de Matos Gomes, M. S. Belsley, B. Almeida, and N. Cerca, "Strong enhancement of second harmonic generation in 2-methyl-4-nitroaniline nanofibers," Nanoscale **4**(16), 4978 (2012).

71. B. F. Levine, C. G. Bethea, C. D. Thurmond, R. T. Lynch, and J. L. Bernstein, "An organic crystal with an exceptionally large optical second-harmonic coefficient: 2-methyl-4-nitroaniline," J. Appl. Phys. **50**(4), 2523–2527 (1979).

3 Self-assembly Strategies

This chapter will focus on self-assembly techniques that attempt to translate individual molecular optoelectronic properties into macroscopic effects. Several typical approaches to implement micro-manufacturing by self-assembly are introduced. The chapter concludes with a short theoretical description of the self-assembly process.

3.1 - Organic engineering

The robust local control of light and matter interactions at room temperature would create the foundations for the practical implementation of photonic quantum technologies [1]. Many demonstrations of quantum processes require cryogenic temperatures to protect the quantum states. Thermal and spontaneous interactions often introduce dephasing leading to decoherence. Nano-engineering of the local environment can relax these thermal constraints. For example, when an excited molecule returns to its low-energy ground state by the spontaneous emission of a photon, the process is generally incoherent and irreversible. Normally the emitted photon would be lost. However, if the molecule is strongly coupled to an optical resonator [2], [3] that subtends a significant solid angle, then there is a high probability that the emitted photon will remain near the emitter until it is reabsorbed. Under the strong coupling regime, the atom-cavity system can lead to a long-lived a coherent quantum state, well described by the Jaynes-Cummings model.

Organic devices, despite their potentially strong role in next-generation optoelectronic devices, are often challenging to implement experimentally, due to their inherent structural disorder; they often contain significant grain boundaries, lattice defects or vacancies. These imperfections can complicate the transport of energy or charge over intermolecular distances, creating limitations that are not present in the bulk inorganic alternatives. The successful application of the organic materials in nanophotonics will require strategies to overcome or suppress these limitations depending on the specific functionalities of the devices [4], [5]. Concurrently, different synthesis and assembly strategies can also alter the optical and/or electronic responses at the individual molecular scale, indicating the need for a multi-scale assessment [6].

Self-assembly strategies rely on the strong intermolecular interactions to create the desired structures over a large range of size scales [7]–[9]. The molecular components, either separate or linked, spontaneously form ordered aggregates without any external trigger. Since they proceed via spontaneous processes, they tend to lead to thermodynamically stable structures. Through the self-assembly process, one or several intermolecular interactions may be the driving forces. The type and strength of the driving forces are generally molecular structure dependent, which when properly manipulated, offers one of the most broad-spectrum strategies available for engineering nanostructures [10]. Self-assembling processes are especially interesting from a materials processing point of view as they provide a route to create regular structures without contamination or phase separations (see figure 3.1). They have long been employed in chemistry and materials

science to create supramolecular structures with sizes ranging from the nano scale to well-ordered macroscopic ensembles.

One traditional form of self-assembly is the process of crystal growth that encourages the arrangement of molecular units into long range, regular and two or three-dimensional periodic system [11], [12]. The growth of organic crystals has several peculiarities in comparison the main classes of inorganic crystals with optical applications, but recent progress has led to expanded activity and lower costs. Several organic materials are readily available in the form of high quality, defect-free crystals, often a prerequisite for their technological application. All the crystal growth processes can be broadly classified according to preparation of the precursor materials [13]. The vast majority of approaches can be categorized as either growth from melts, solutions or gas phase deposition. The nature of the individual building blocks, their interactions and the specifications of the desired physical properties all must be considered when choosing the most suitable method for a given application or structure. Several self-assembly methods are particularly well adapted to micro-manufacturing and the following text gives a quick review of some key strategies.

3.2 Melt growth – Bridgman-Stockbarger method

One of the more conventional approaches to obtain organic crystals, the Bridgman-Stockbarger method, follows a traditional method to grow inorganic crystals [14]. The vertical Bridgman technique is one of the simplest and oldest melt techniques to rapidly obtain high quality bulk crystals.

Crystal growth using the Bridgman technique is based on directional solidification by translating a melt material from the hot to the cold zone of the furnace. The active control of how the material moves through the temperature gradient determines the quality of the grown crystals. The starting material, typically a powder, is placed into a quartz ampoule, sealed under high vacuum, put into the Bridgman furnace and heated [14]–[17]. When the melt is homogeneous, the furnace is slowly moved upwards. Consequently, the melt experiences a temperature gradient, the narrow tip of the ampoule always being the coldest point. Crystallization will start there, and as the ampoule is gradually removed from the furnace, growth proceeds until the ampoule is filled with one single crystal. During growth the boundary surface of the liquid melt is surrounded and in contact with the walls, allowing the latent heat associated with crystallization to be discharged by conduction.

This method has several advantages including its simplicity and the possibility of varying the growth conditions. It is easy to control the vapor pressure of the volatile components; it is even possible to carry out growth under a vacuum in a sealed container. The relatively well-stabilized temperature gradient, also permits come control over the extent of convective mixing and segregation [18]–[21]. Conversely, this method does not allow one to specify the orientation of the obtained crystals. Both vertical and horizontal system configurations are possible.

3.3 Self-assembly

Almost all organic compounds have the inclination to self-assemble. However, many optoelectronic applications require the growth of specific crystal orientations often within a pre-determined structural from different from that which spontaneously occurs through self-assembly [22]. Important progress has been made in this direction over the past couple of years [23].

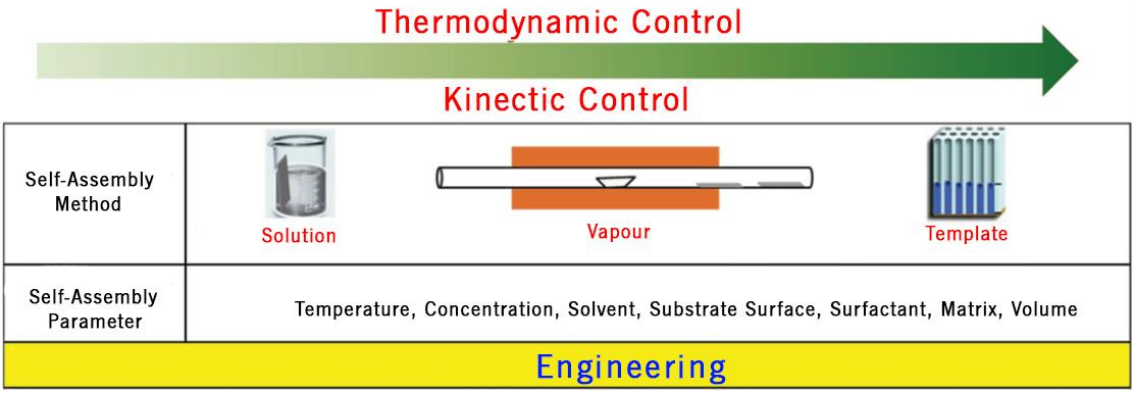

Figure 3.1 - Molecular self-assembling engineering. Design and processing for functional crystalline nanostructures.

3.3.1 Self-Assembly in the Liquid Phase

Organic compounds are soluble in a variety of organic solvents, even at room temperature. Moreover, solution growth allows a considerable degree of control over process parameters, including temperature, solution viscosity and concentration. The equipment needed for solution growth is simple and low-cost, and good morphology crystals can be produced with a small number of defects [24]–[26].

The self-assembly of organic molecules into nanostructures is based on the driving forces from the molecules themselves, sometimes encouraged by a nucleation initiator from the surroundings. Organic nanotubes, for example, can be achieved through the Coulomb interactions between two oppositely charged ionic precursors in aqueous solutions. The dimensions of the nanotubes can be tuned by simply changing the temperature of the aqueous solution [7]. Sonication can control the length of the self-assembling structures [27]. Lamellar structures have been obtained through the cooperation of three chemically orthogonal and spatially independent noncovalent intermolecular interactions, namely, hydrogen bonds, $\pi-\pi$ interaction and van der Waals contact [28].

Based on the properties of the organic molecules to be crystallized, several solution methods are available such as, solvent evaporation [29], slow cooling [30], vapour diffusion [31] and liquid-liquid diffusion [24]. Solvent evaporation method is by far the simplest and often the most effective method to grow single crystals. Volatile organic solvents, such as toluene, are usually employed. If a beaker containing a solution is not hermetically sealed, the solvent can slowly evaporate forming a supersaturated solution. Spontaneous nucleation will eventually occur followed by growth into larger crystals.

3.3.2 Organogelation

Self-assembly through organogelation occurs mainly in gel [32]. A gel denotes a dilute mixture of at least two components, in which each of the components form a separate continuous phase throughout the system. For example, peptide molecules are capable of gelating in a wide range of aromatic and aliphatic organic solvents like benzene, toluene, ethyl acetate, tetrahydrofuran, chloroform and many others. Generally, gels are divided into two groups, chemical gels and physical gels, depending on the type of interactions that hold the network structure together. The physical type are those where the network structures are held together by non-covalent interactions such as hydrogen bonding or $\pi-\pi$ stacking. Additionally, solvophobic and entropic effects can be very important in the formation of organogels. These strategies have proven very effective in constructing organic 1D nanomaterials with a variety of structures and properties [33], [34].

3.3.3 Solvent Evaporation

Almost all organic materials can be dissolved in some organic solvent. As the solvents evaporate, the local concentration increases and molecular aggregates slowly form, eventually leading to small

crystals. This is a chaotic process in which, the size, morphology, and uniformity of the molecular aggregates are not easy to control, especially in the nanometer regime [35]. However, it is possible to achieve well-defined macroscopic single crystals, often through the use of seed crystals in saturated solutions [36]. In fact, this is the most common strategy to obtain organic single crystals. Some researchers have applied sonication to the solvent evaporation process as an approach to tune the morphologies of the resulting nanostructures. The final structures are heavily influenced by the container substrate and evaporation conditions as well the initial concentration and the type of the solvent used [37].

3.3.4 Assembling in templates

A straightforward way to fabricate nanostructures with a specific morphology and structure is by a template method. In this approach, target materials are induced to grow according to a template pattern. Nanomaterials have been obtained with a pre-determined shape and size [38].

The templates adopted in this method can be divided into two groups: soft and hard [39]. Soft templates are those that can be dissolved in the liquid phase. For example, micelles or inverse micelles [26]. It is well known that micelles can be formed with different shapes, such as spherical or rod-like, by varying the critical micelle concentration.

Hard templates are often used in the fabrication of inorganic nanomaterials, but have recently been invoked to fabricate organic nanomaterials [40], [41]. This group includes, but is not limited, to ordered porous membranes prepared with anodized aluminum oxide, silica, nanochannel glass, and ion-track-etched polymers.

3.4 Poling

The tendency of organic π systems to organize themselves in centrosymmetric structures has already been mentioned as the principal limitation in the macroscopic application of organic systems in second order NLO. However, the centro-symmetry can be broken by applying a strong electric field to align the molecular dipole moments along a single direction [42]. To lock in this electric field induced alignment, the molecules are typically incorporated inside polymeric hosts to prevent the relaxation into their natural (centrosymmetric) state (see Figure 3.2). Sol-gel matrices can also be used as a support, but polymers are usually easier and more versatile [43]. The

simplest method is to simply mix the active molecules in a polymer solution and let the solution crystallize into a guest-host system. By heating the polymer above its glass transition temperature, the guest organic molecules gain the ability to reorient in response to a strong applied DC electric field. This introduces a long-range orientational order that can be frozen in by subsequently lowering the temperate below the glass transition point. UV irradiation had also been used during the application of the strong DC electric field to enhance the orientation of chromophores [44]. If no further steps are taken, the achieved alignment corresponds to a metastable state that tends to relax over a timescale of weeks to months back to the equilibrium centrosymmetric state due to the strong Coulomb forces associated with the dipole–dipole interactions. Higher organic molecule concentrations tend to lead to faster relaxation rates. Some additional methods such as a crosslinking have been employed in an attempt to prevent this relaxation [42].

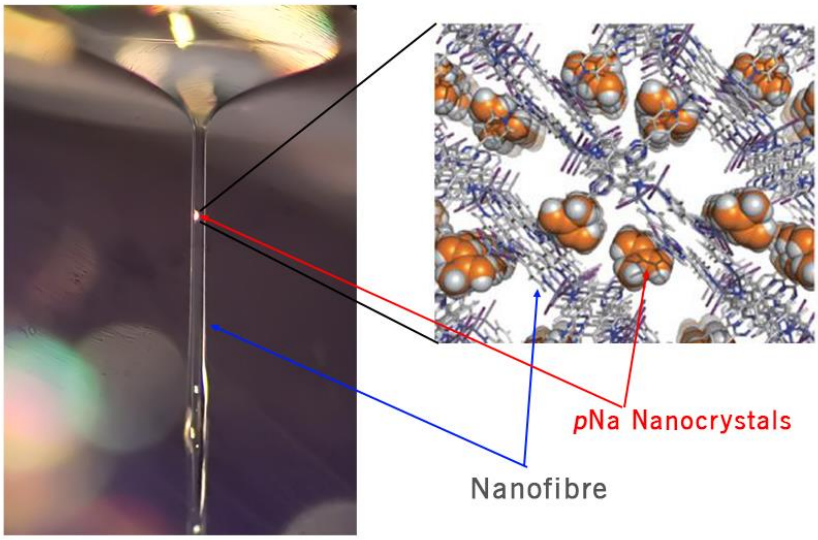

Figure 3.2 – Representation of the polymeric nanofibre doped with pNa an example of guest-host system approach.

3.5 Morphology Control

The control of morphology is often a key factor for optoelectronic applications. The morphologic control of organic nanomaterials has met with limited success in contrast to their inorganic nanomaterial counterparts where choice of the appropriate materials and established synthesis methods have been used [45], [46]. The most commonly used strategy to modulate organic nanostructures is create a series of derivatives. For examples, researchers have prepared either nanobelts or nanospheres by using two different derivatives of perylene [47]. Besides

nanostructures made from compounds with different substituents, nanostructures with well-defined shapes, such as spheres, square wires and cubes, have also been prepared [8]. For example, different organic nanostructures morphologies have been obtained through the self-assembly of three isomeric molecules of bis(imino-pyrrole)benzene with the same substituents at different positions [47], [48]. Although all three isomeric precursors, *o*-, *m*-, and *p*-bis(iminopyrrole) benzene, exhibit similar, strong, multiple hydrogen-bonding interactions for molecular aggregation, distinctly shaped nanostructures were obtained [49]. The two iminopyrrole groups in the *o*-isomer are 60° open-armed. Therefore, two monomers can interlock to form a dimer by means of quadruple hydrogen bonds, which act as the basic units for the formation of spherical structures. In contrast, the configurations of *m*- and *p*-isomers, with two iminopyrrole groups open-armed at angles of 120° and 180°, respectively, allow each molecule to connect with two other molecules via hydrogen bonds, forming chain-like structures. Also determined by the molecular configurations, the chain of the *m*-isomer is zigzag shaped while that of the *p*-isomer is almost linear. These chains are the building blocks to form square wires and cubes, respectively. Essentially, different interactions involved in aggregate stacking at the supramolecular level associated with the isomeric molecular structures are responsible for the different morphological configurations.

Another approach to control the shape and dimension of aggregated organic systems is to induce their self-assembly on nanostructured surfaces with different morphologies [50], [51].

3.6 Theoretical aspects

Crystal growth inside a polymeric matrix is essentially a process of aggregation within a confined space. There can be a strong interaction at the interface between the growing organic crystal and the solution phase of the surrounding polymeric matrix. An equilibrium between crystal growth and dissolution corresponds to a dynamic state for which variations in its concentrations $\left(\Delta C = C - C^*\right)$ and mass exchange vanish. This corresponds, to a specific point on a solubility curve in the phase diagram of a solution where the concentration does not change, a point which can often be manipulated by changes in temperature [35].

The theoretical description of the spontaneous association of freely diffusing molecules into finite-sized supramolecular objects at the solid–liquid interface, assumes that in systems at chemical equilibrium there is no net exchange between the two components, i.e.

$$\eta \mathrm{A} \leftrightarrow \mathrm{B} \tag{0.1}$$

where A is the monomeric species, B is the self-assembled architecture, and η it is the molecularity of the reaction. The exchange between the monomer and the supermolecular assembly can be described by the difference in the chemical potentials between the two phases: that of the crystal $\left(\mu_B\right)$ equalizes and that of the reactant $\left(\mu_A\right)$

$$\Delta\mu_{AB} = \mu_A - \mu_B \tag{0.2}$$

From this, a generalized driving force may be expressed as:

$$\Delta\mu = k_\beta T \ln\left(\frac{C}{C^*}\right) \tag{0.3}$$

where k_β is the Boltzmann constant, C/C^* is the ration between the initial concentration (C) and cluster concentration $\left(C^*\right)$ and T is the absolute temperature. The driving force can be characterized in terms of an unit-less parameter, $\Delta\mu\left(k_\beta T\right)^{-1}$.

Self-assembly typically starts by the initial association of a random cluster of a few molecules. Subsequently more molecules join, forming a structure that continually grows. In the limit of idealized behaviour and at a constant temperature and volume $\left(\mathrm{V}\right)$, the chemical potential can be expressed as

$$\mu_i\left(\mathrm{V},\, T\right) = -kT \ln \frac{q_i\left(\mathrm{V},T\right)}{N_i} \tag{0.4}$$

with and q_i and N_i being the molecular partition function and the number of molecules of the ith component, respectively.

The chemical potential of a finite-sized supramolecular structure physio-adsorbed at the interface with the polymeric matrix can be estimated introducing the harmonic oscillator approximation and the Born–Oppenheimer hypothesis [35].

$$\mu_i(\mathrm{V},T) = -kT\ln\left[\left(\frac{2\pi mkT}{h^2}\right)\frac{S_{\mathrm{Int}}}{N}\right] - kT\ln\left[\frac{\sqrt{\pi}}{\sigma}\left(\frac{8\pi^2 kT}{h^2}\right)^{\frac{1}{2}}\sqrt{I_{\mathrm{Int}}}\right] - kT\sum_{j=1}^{3n-3}\ln\left[2\sinh\left(\frac{h\nu_j}{2kT}\right)\right] - D_e \quad (0.5)$$

Here the volume has turned into structure edge area S_{Int} where I_{Int} is the principal moment of inertia of the molecule around the axis perpendicular to the edge, the number of vibrational modes has increased to $3n-3$ as one translational and two rotational degrees of freedom are effectively converted into internal vibrations upon 2D confinement, and D_e describes the interaction with the surface.

In quantitative terms, this situation at the edge of the structure and the interface with the host matrix can be described as follows. The formation of a solid structure in a homogeneous interface results from spending a necessary quantity of energy.

$$\varepsilon_{B\leftrightarrow S_{\mathrm{Int}}} = \varepsilon_B + \varepsilon_{S_{\mathrm{Int}}} \quad (0.6)$$

The total quantity of energy (ε) required for the formation of a stable structure is equal to the sum of the energy required to form the surface edge $\left(\varepsilon_{S_{\mathrm{Int}}}\right)$ a positive quantity, and the energy $\varepsilon_{S_{\mathrm{Int}}}$ required to form the bulk of the structure (ε_B) a negative quantity.

While the chemical potential of the unit cell is concentration independent, it is necessary to take into consideration both the concentration of building blocks and the packing density. When the chemical equilibrium is established, the free energy does not vary with temperature. Therefore, the total change in Gibbs free energy $\left(\Delta \mathrm{G}^*\right)$, between the crystalline phase and the surrounding matrix results in a driving force, which stimulates crystallization [52]. This free energy is the sum of the edge free energy and the volume free energy which can be simply expressed as,

$$\Delta \mathrm{G}^* = \Delta \mathrm{G}_0 - \frac{1}{\mathrm{A}_{\mathrm{UC}}} kT\ln\frac{C_{S_{Int}}}{C_B} \quad (0.7)$$

Equation (0.7) represents the total free energy normalized to the area of the unit cell per molecule $\left(\mathrm{A}_{\mathrm{UC}}\right)$. The concentration of the molecules in bulk structures is represented by C_B and the concentration of the molecules at the edge is given by $C_{S_{\mathrm{Int}}}$ (see Figure 3.3).

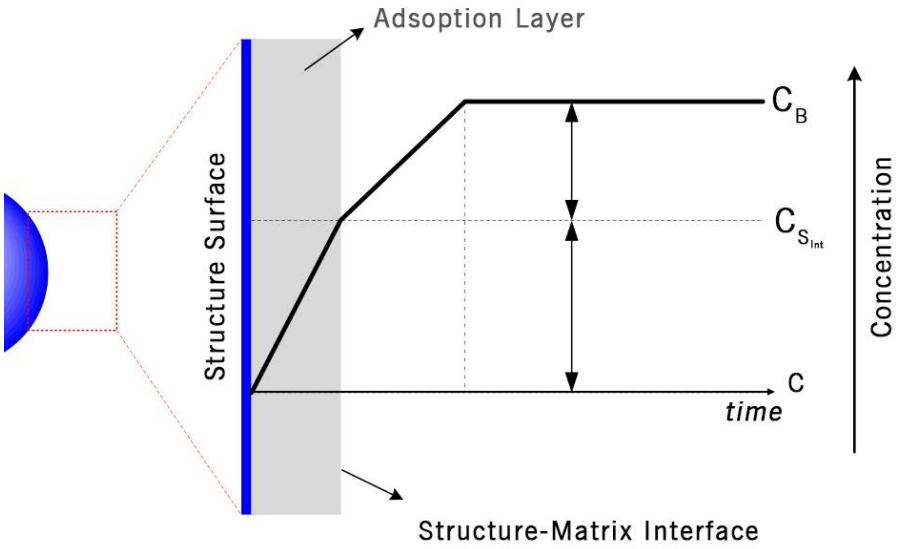

Figure 3.3 - Model for structure growth with concentration driving in solution state.

3.7 Bibliography

[1] J. L. O'Brien, A. Furusawa, and J. Vučković, "Photonic quantum technologies," *Nat. Photonics*, vol. 3, no. 12. pp. 687–695, 2009.

[2] P. Kumar, P. Kwiat, A. Migdall, S. W. Nam, J. Vuckovic, and F. N. C. Wong, "Photonic technologies for quantum information processing," in *Exper. Aspects of Quantum Comp.,* pp. 215–231, 2005.

[3] G. Kurizki *et al.*, "Quantum technologies with hybrid systems," *Proc. Natl. Acad. Sci.*, vol. 112, no. 13, pp. 3866–3873, 2015.

[4] A. J. C. Kuehne and M. C. Gather, "Organic Lasers: Recent Developments on Materials, Device Geometries, and Fabrication Techniques," *Chem. Rev.,* vol. 116, no. 21. pp. 12823–12864, 2016.

[5] Y. Yan and Y. S. Zhao, "Organic Nanophotonics: Controllable Assembly of Optofunctional Molecules toward Low-Dimensional Materials with Desired Photonic Properties," in *Soft Matter Nanotechnology*, 2015, pp. 131–160.

[6] B. Lebeau and P. Innocenzi, "Hybrid materials for optics and photonics," *Chem. Soc. Rev.*, vol. 40, no. 2, pp. 886, 2011.

[7] Y. Guo, L. Xu, H. Liu, Y. Li, C. M. Che, and Y. Li, "Self-Assembly of functional molecules into 1D crystalline nanostructures," *Adv. Mater.*, vol. 27, no. 6, pp. 985–1013, 2015.

[8] George M. Whitesides and Mila Boncheva, "Beyond Molecules: Self-Assembly of Mesoscopic and Macroscopic Components," *Proc. Natl. Acad. Sci. U. S. A.*, vol. 99, no. 8, pp. 4769–4774, 2002.

[9] K. Takazawa, Y. Kitahama, Y. Kimura, and G. Kido, "Optical waveguide self-assembled from organic dye molecules in solution," *Nano Lett.*, vol. 5, no. 7, pp. 1293–1296, 2005.

[10] J. L. A. Jonathan W. Steed, "Supramolecular chemistry.," *Science*, vol. 260, no. 5115, pp. 1762–1763, 1993.

[11] S. Rosenne *et al.*, "Self-Assembled Organic Nanocrystals with Strong Nonlinear Optical Response," *Nano Lett.*, vol. 15, no. 11, pp. 7232–7237, 2015.

[12] A.-P. Hynninen, J. H. J. Thijssen, E. C. M. Vermolen, M. Dijkstra, and A. van Blaaderen, "Self-assembly route for photonic crystals with a bandgap in the visible region.," *Nat. Mater.*, vol. 6, pp. 202–205, 2007.

[13] R. Li, W. Hu, Y. Liu, and D. Zhu, "Micro- and nanocrystals of organic semiconductors," *Acc. Chem. Res.*, vol. 43, no. 4, pp. 529–540, 2010.

[14] H. Potts and W. R. Wilcox, "Thermal fields in the bridgman-Stockbarger technique," *J. Cryst. Growth*, vol. 73, no. 2, pp. 350–358, 1985.

[15] G. T. Neugebauer and W. R. Wilcox, "Convection in the vertical Bridgman-Stockbarger technique," *J. Cryst. Growth*, vol. 89, no. 2–3, pp. 143–154, 1988.

[16] D. Nicoară and I. Nicoară, "An improved Bridgman-Stockbarger crystal-growth system," *Mater. Science and Engineering*, vol. 102, no. 2. 1988.

[17] H. Potts and W. R. Wilcox, "Chaotic asymmetric convection in the Bridgman-Stockbarger technique," *J. Cryst. Growth*, vol. 74, no. 2, pp. 443–445, 1986.

[18] Q. Ai, P. Chen, Y. Feng, and Y. Xu, "Growth of Pentacene-Doped p-Terphenyl Crystals by Vertical Bridgman Technique and Doping Effect on Their Characterization," *Cryst. Growth Des.*, vol. 17, no. 5, pp. 2473–2477, 2017.

[19] B. Riscob, N. Vijayan, M. Shakir, M. A. Wahab, and G. Bhagavannarayana, "Effect of crucible design on crystalline perfection and the enhanced optical properties of benzimidazole single crystals grown by the vertical Bridgman technique," *J. Appl. Crystallogr.*, vol. 46, no. 1, pp. 276–278, 2013.

[20] D. A. Jones, "The crystallization of materials having high vapour pressures at their melting points by the

Bridgman-Stockbarger technique," *J. Cryst. Growth*, vol. 34, no. 1, pp. 149–151, 1976.

[21] X. Yang, G. Lv, W. Ma, H. Xue, and D. Chen, "The effect of radiative heat transfer characteristics on vacuum directional solidification process of multicrystalline silicon in the vertical Bridgman system," *Appl. Therm. Eng.*, vol. 93, pp. 731–741, 2016.

[22] C. C. Figura, "*Second Order Nonlinear Optics in Ionically Self-Assembled Thin Films*" PhD Diss. Blacksburg, Virginia, pp. 1–24, 1999.

[23] T. Nishinaga, "*Handbook of Crystal Growth: Bulk Crystal Growth"* Second Edition, vol. 2. Elsevier, 2014.

[24] H. K. Bisoyi and Q. Li, "Light-directing chiral liquid crystal nanostructures: From 1D to 3D," *Acc. Chem. Res.*, vol. 47, no. 10, pp. 3184–3195, 2014.

[25] L. Wang and Q. Li, "Stimuli-Directing Self-Organized 3D Liquid-Crystalline Nanostructures: From Materials Design to Photonic Applications," *Adv. Funct. Mater.*, vol. 26, no. 1, pp. 10–28, 2016.

[26] M. Poutanen *et al.*, "Block Copolymer Micelles for Photonic Fluids and Crystals," *ACS Nano*, vol. 12, no. 4, pp. 3149–3158, 2018.

[27] S. A. Wang *et al.*, "Room-Temperature Synthesis of Soluble Carbon Nanotubes by the Sonication of Graphene Oxide Nanosheets," *J. of the American Chem. Soc.,* vol. 131, no. 46. pp. 16832–16837, 2009.

[28] A. Garg, R. M. Davis, C. Durak, J. R. Heflin, and H. W. Gibson, "Polar orientation of a pendant anionic chromophore in thick layer-by-layer self-assembled polymeric films," *J. Appl. Phys.*, vol. 104, no. 5,pp. 053116, 2008.

[29] P. M. Dinakaran and S. Kalainathan, "Synthesis, growth, structural, spectral, linear and nonlinear optical and mechanical studies of a novel organic NLO single crystal 4-Bromo 4-Nitrostilbene (BONS) for nonlinear optical applications," *Opt. Mater.*, vol. 35, no. 5, pp. 898–903, 2013.

[30] R. M. Kumar, D. R. Babu, D. Jayaraman, R. Jayavel, and K. Kitamura, "Studies on the growth aspects of semi-organic l-alanine acetate: A promising NLO crystal," in *J. of Cryst. Growth*, vol. 275, no. 1–2, pp. 1935-1939 2005.

[31] G. De Luca *et al.*, "Self-assembly of discotic molecules into mesoscopic crystals by solvent-vapour annealing," *Soft Matter*, vol. 4, no. 10, pp. 2064, 2008.

[32] K. Narasimha and M. Jayakannan, "pi-Conjugated Polymer Anisotropic Organogel Nanofibrous Assemblies for Thermoresponsive Photonic Switches," *ACS Appl. Mater. Interfaces*, vol. 6, no. 21, pp. 19385–19396, 2014.

[33] R. Zhang *et al.*, "Synthesis and nonlinear optical properties of a cross-linkable system using sol-gel approach," *J. Non. Cryst. Solids*, vol. 358, no. 6–7, pp. 1003–1008, 2012.

[34] F. Pan *et al.*, "Polymorphism, growth and characterization of a new organic nonlinear optical crystal: 4-dimethylaminobenzaldehyde-4-nitrophenylhydrazone (DANPH)," *J. Cryst. Growth*, vol. 165, no. 3, pp. 273–283, 1996.

[35] S. Conti and M. Cecchini, "Predicting molecular self-assembly at surfaces: a statistical thermodynamics and modeling approach," *Phys. Chem. Chem. Phys.*, vol. 18, no. 46, pp. 31480–31493, 2016.

[36] W. L. Wang, M. Wang, and W. D. Huang, "A novel growth method for organic nonlinear optical crystals," *Opt. Mater.*, vol. 27, no. 3, pp. 609–612, 2004.

[37] H. Chen *et al.*, "Engineering of Organic Chromophores with Large Second-Order Optical Nonlinearity and Superior Crystal Growth Ability," *Cryst. Growth Des.*, vol. 15, no. 11, pp. 5560–5567, 2015.

[38] H. Search, C. Journals, A. Contact, M. Iopscience, and I. P. Address, "Nanostructure fabrication using block copolymers," *Nanotechnology*, vol. 39, pp. 39–54, 2003.

[39] N. Haberkorn, M. C. Lechmann, B. H. Sohn, K. Char, J. S. Gutmann, and P. Theato, "Templated organic and hybrid materials for optoelectronic applications," *Macromolecular Rapid Communications*, vol. 30, no. 14. pp. 1146–1166, 2009.

[40] K. Shiba, M. Tagaya, R. D. Tilley, and N. Hanagata, “Oxide-based inorganic/organic and nanoporous spherical particles: Synthesis and functional properties,” *Science and Tech. of Adv. Materials*, vol. 14, no. 2, pp. 23002, 2013.

[41] S. Cambré, J. Campo, C. Beirnaert, C. Verlackt, P. Cool, and W. Wenseleers, “Asymmetric dyes align inside carbon nanotubes to yield a large nonlinear optical response,” *Nat. Nanotechnol.*, vol. 10, no. 3, pp. 248–252, 2015.

[42] C. Cabanetos *et al.*, “New cross-linkable polymers with Huisgen reaction incorporating high $\mu\beta$ chromophores for second-order nonlinear optical applications,” *Chem. Mater.*, vol. 24, no. 6, pp. 1143–1157, 2012.

[43] P. M. Wallace, D. R. B. Sluss, L. R. Dalton, B. H. Robinson, and P. J. Reid, “Single-molecule microscopy studies of electric-field poling in chromophore-polymer composite materials,” *J. Phys. Chem. B*, vol. 110, no. 1, pp. 75–82, 2006.

[44] Y. Wang *et al.*, “Electric-field-induced layer-by-layer fabrication of second-order nonlinear optical films with high thermal stability.,” *Langmuir*, vol. 20, no. 21, pp. 8952–8954, 2004.

[45] G. A. Ozin, A. C. Arsenault, L. Cademartiri, "*Nanochemistry : a chemical approach to nanomaterials*." Royal Society of Chemistry, Great Britain, Royal Society of Chemistry, 2009.

[46] J.-M. Lehn, "*Supramolecular Chemistry*." Weinheim, FRG: Wiley-VCH Verlag GmbH & Co. KGaA, 1995.

[47] M. Huang, M. Antonietti, and H. Cölfen, “Morphology-controlled growth of perylene derivative induced by double-hydrophilic block copolymers,” *APL Mater.*, vol. 4, no. 1, pp. 15705, 2016.

[48] S. Ghosh, X. Q. Li, V. Stepanenko, and F. Würthner, “Control of H- and J-type π stacking by peripheral alkyl chains and self-sorting phenomena in perylene bisimide homo- and heteroaggregates,” *Chem. - A Eur. J.*, vol. 14, no. 36, pp. 11343–11357, 2008.

[49] Y. Wang *et al.*, “Distinct nanostructures from isomeric molecules of bis(iminopyrrole) benzenes: effects of molecular structures on nanostructural morphologies,” *Chem. Commun.*, no. 16, p. 1623, 2007.

[50] J. J. Gooding and S. Ciampi, “The molecular level modification of surfaces: from self-assembled monolayers to complex molecular assemblies,” *Chem. Soc. Rev.*, vol. 40, no. 5, pp. 2704, 2011.

[51] J. C. Love, L. A. Estroff, J. K. Kriebel, R. G. Nuzzo, and G. M. Whitesides, “Self-assembled monolayers of thiolates on metals as a form of nanotechnology,” *Chem. Rev.*, vol. 105, no. 4. pp. 1103–1169, 2005.

[52] S. Lei, K. Tahara, F. C. De Schryver, M. Van Der Auweraer, Y. Tobe, and S. De Feyter, “One building block, two different supramolecular surface-confined patterns: Concentration in control at the solid-liquid interface,” *Angew. Chemie - Int. Ed.*, vol. 47, no. 16, pp. 2964–2968, 2008.

4 Experimental Techniques

In this chapter, the tools and techniques that were used to perform measurements of nonlinear optical properties shall be described. In particular, the polarimetry procedure used to perform the SHG measurements in transmission mode. The measurements were carried out with high spatial and temporal resolution with low noise due to the Kerr mode-locked Ti:Sapphire laser that delivers stable, spatially and temporally coherent ultra-short laser pulses and a high-sensitivity detection scheme. In addition, bulk characterization techniques of the *p*Na materials will be also addressed.

Fabrication of nano-tailored materials is often motivated by advanced applications in the fields of separation, catalysis, medicine, electronics and optics. An important area of nano-tailored materials consists of polymeric nanofibers, polymeric nanostructures, hybrid materials and direct writing templates [1].

Organic structures with applications in micro and nano optoelectronics are still largely limited to laboratory scales. These devices often have major problems in relation to their long-term performances, reproducibility and reliability. Until industry-scale production is achieved, future visions for organic optoelectronic will remain just that – visions.

In this work two approaches with the potential to grow and design large surfaces that can be used in a variety of devices and applications have been explored; electrospinning and capillary growth from a mixed organic chromophore polymeric solution. These two approaches attempt to translate the strong second order nonlinear optical response of individual *p*Na molecules to a macroscopic level. In both of these two particular cases, the organization of the *p*Na molecules has been manipulated to give rise to macroscopic SHG.

4.1 - Electrospinning

Among all the techniques used for the development nanostructures, electrospinning is an especially attractive method due to its versatility and simplicity [2–6]. Electrospinning allows the fabrication of polymer nanofibers membranes composed of randomly distributed nanofibers, forming a three-dimensional network. These networks present a high surface area and is being used as a strategy to increase the sensitivity and response of the material [7–9]. Nanofibres materials produced through electrospinning are attractive in many fields, particularly in the food industry where protective electro-spun membranes potentially allow for the time-controlled release of embedded chemical constituents [10]. Their characteristic high surface area per volume ratio, offer a high chemical load area with reduced volume and material.

The large surface to volume ratio of electro-spun polymeric nanofibers is the main motivating reason for their use in the developing the hybrid materials here presented.

Geometrically, the surface area per unit volume is inversely proportional to the fibers diameter [11]. The diameter can be controlled by several process parameters. For example, thinner fibres can be obtained by controlling the precursor solution parameters such as viscosity and concentration. Concentration is a critical parameter; very low concentrations, with very low viscosity, tend to result in defects arising in the drying of the material during the short path of the polymeric jet in the air, due to the excess solvent and lack of matrix, resulting in irregular fibers and even breaks [9,12]. However to promote the forming of the polymeric jet, the solution should also have a sufficiently low surface tension, a high charge density and a suitable viscosity to prevent the collapse of the jet into beads or droplets before the solvent evaporates. The control of the diameter of the fibres is typically limited to a narrow window of appropriate concentrations. The main mechanical parameters that can be adjusted in electrospinning fabrication are: solution flow, target collector distance, applied voltage and needle diameter. The adjustment of these parameters is essential to obtain nanofibers with the desired morphologies and diameters. This has been justified in the extensive literature. Their optimization was an important preliminary phase prior to the main work reported in this thesis. There are also several environmental parameters including temperature, humidity and air composition, which may also influence the formation and morphology of nanofibers [12].

The final jet diameter of the polymeric solution is the result of the balance between surface tension and electrostatic repulsion [13].

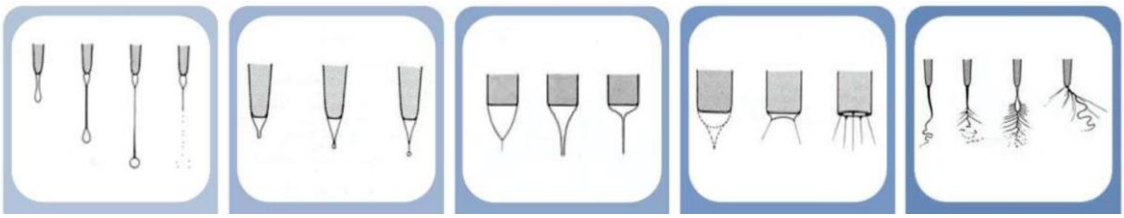

Figure 4.1 – Schematic representation of the applied electrical potential in the polymeric jet solution in the electrospinning technique. From low potential, left, to height potential, right.

When the applied voltage is too small, the electric forces cannot overcome the surface tension and no jet is emitted.

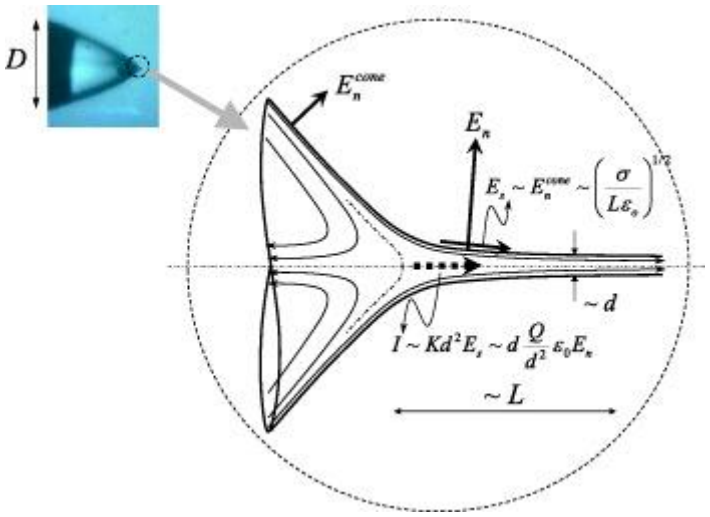

Figure 4.2 - Schematics of the Taylor cone–jet situation at the applied electrical potential and flow rate.

Therefore, there is a limit voltage needed to ensure that the fluid jet is continuous. Another very important choice is that of the solvent used in the precursor solution. For the formation of fibres, a solvent with a high vapor pressure is required. Insufficient vapor pressure can lead to excessive bead formation (droplets trapped on the fibres) and in the limiting case prevent the formation of fibers due to the lack of solvent evaporation. In these cases, increasing the applied voltage and the distance between the capillary and the collector can be beneficial [14]. Nevertheless, excessive high voltages can provoke higher solvent evaporation rates, which can lead to solidification at the tip and instability in the jet [15]. Morphological changes in the nanofibers can also occur upon changing the distance between the syringe needle and the collecting substrate. Increasing the distance or decreasing the electrical field decreases the bead density, regardless of the concentration of the solution polymer. When the electric field and the fluid flow rate are tuned such that the electric forces exceed the value of the liquid's surface tension a Taylor cone is formed. The tangential electric field then accelerates the charge carriers in the liquid, increasing the velocity of the surrounding fluid toward the counter electrode at the collector. Practically, the flow rate and the applied voltage are the main process parameters that were varied to study how they influence the SHG response of the resulting fibers.

The choice of polymer for the matrix is also crucial, as the local environment will determine how the *p*Na molecules self-assemble during the electrospinning process. There is a need for a combination of its transmissivity characteristic and the surface SHG of the self-assembling nanocrystals of *p*Na. Given the results of the second harmonic generation, it can be concluded that

PMMA presents a good choice for the polymer matrix [16,17]. The combination of its tensile strength, compression and transparency, which seem to encourage a self-assembly of the *p*Na molecules that possesses a strong macroscopic second order NLO response from this hybrid material.

4.1.1 Experimental procedure

The electrospinning device that produced fibers with a macroscopic SHG response, consisted of a capillary (tip diameter 0.6 mm), which included a wire electrode, a grounded counter electrode placed 12 cm from the capillary and a high voltage source. The potential between the electrodes was adjusted with a high-voltage power supply (Spellmann CZE2000).

The doped polymer nanofibers were prepared by electrospinning of a solution of PMMA with a molecular weight of 120000 (purchased from Alfa Aesar). The solutions containing a ratio of 2:1 between polymer and *p*Na (purchased from Sigma Chemical Co) by weight were dissolved in toluene and stirred for several hours under ambient conditions. To be able to perform the subsequent optical investigations, a transparent substrate in the form of a thin cover slide glass was placed on axis of the rotational collector (velocity of 100 rpm). The amount of the fibres deposited on the cover slides was controlled by the electrospinning time.

4.2 - Growth of layered structures

Several times in the previous chapters, it was emphasized that organic crystals have been receiving much attention for potential applications in optoelectronics. Underlying most of these possible applications is the ability to creating and manipulate radiation. One particular route to achieve this is to engineer of nano-tailored organic materials to self-assemble in a non-centrosymmetric crystal lattice. The absence of an inversion centre leads to a range of symmetry-dependent properties such as piezo- and pyroelectricity, chirality, circular dichroism and even order nonlinear optical properties [18]. Many potential applications, especially sensing and switching tasks, could benefit from the availability of large area, low-cost, thin and flexible radiation sources, but the currently available technologies, based on bulky and rigid inorganic semiconductors, have not been able to deliver such devices.

The noncentrosymmetric organization of molecular building blocks is an essential requirement for a bulk material to exhibit properties such second order nonlinear optical (NLO) effects and piezoelectricity. However, even centrosymmetric materials loose this symmetry at their surfaces, implying that large area thin centrosymmetric films have the potential to provide an interesting second order nonlinear optical response [19]. This would require growing large-area, high-quality thin organic crystals, which is challenging with current methods. The relationships between chemical structure, supramolecular order and the required optoelectronic properties are fundamental when attempting to optimize the performance of electronic devices, or to design novel devices with desired properties.

A portion of this thesis work was dedicated to exploring how surface effects might influence the nominally centrosymmetric structure of organic crystals during the construction supramolecular assemblies. As will be shown, several of the *p*Na supramolecular structures display strong macroscopic SHG responses, indicating a potential path in advancing beyond conventional synthetic methodologies.

These structures are low-dimensional systems, with a thickness slightly greater than one micron, produced under ambient conditions at a constant temperature. In this approach the growth of the *p*Na structures are spatially restricted to a narrow gap between the two glass slides, similar to the capillarity growth process reported in the literature [20,21].

Understanding the crystallinity of self-assembled *p*Na structures requires some considerations. First, to have nucleation, the anchor group and the end functional group that crystallizes must be similar or compatible. Secondly, the host matrix should show a certain flexibility and mobility to compensate for the space occupied by the growth of the organic superstructures [22]. Thirdly, the *p*Na molecules inside the host matrix must have mobility along the matrix space to facilitate the packing and epitaxial growth of the anchor group and the functional end group, and consequently their crystallization. Nevertheless, the possibility of a rearrangement of the polymer matrix toward a denser packing can be assumed, which in turn facilitates the organic chromophore crystallization, driven by attractive interaction between the anchor and end group of the individual molecules. Intuitively, the mobility of the organic chromophore will depend on the length of the polymeric matrix chain. The particular matrix scaffold structure can shape the variety of chromophore superstructures that are attainable, i.e., whether tilting, bending and twisting are possible, all of which facilitate crystallization.

4.2.1 Experimental procedure

Para-nitroaniline (*p*Na) was purchased from Sigma Chemical Co and used as received. Polystyrene (PS) was purchased from Alfa Aesar. Both Poly(hexano-6-lactone) (PCL) and Poly(methyl methacrylate) (PMMA) with medium and low molecular weights were acquired from Sigma Chemical Co. The polymeric raw materials were dissolved in toluene ($C_6H_5CH_3$, 99.8%), purchased from Sigma-Aldrich. The prepared solution was stirred for several hours under ambient conditions. *p*Na in powder form was subsequently added to the polymeric solution, together with a few drops of acetone to aid dissolution. The respective polymeric solutions with a concentration of 10 wt% and ratio of 2:1 by weight relative to *p*Na were deposited on clean glass microscope slides. The deposited solutions were covered with thin glass coverslips. The growth of the structures was a slow process, occurring over several days.

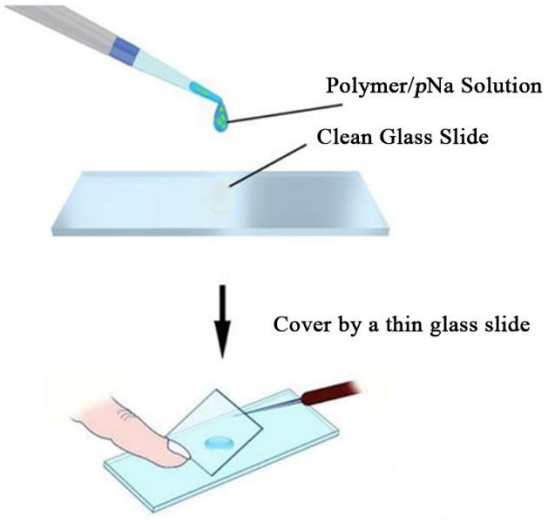

Figure 4.3 – Draw of the approach used to growth pNa structures in the different polymeric matrices.

The structures become visible to the naked eye after a few days. However, they continuously grow as long the polymeric matrix mobility exists, that is until complete evaporation of the toluene and the complete polymerization of its chains. As expected, the resultant structures depend on the respective host matrix; different polymeric matrices lead to distinct *p*Na nanostructures.

The different host matricies were selected in order to explore different aspects of the organic chromophore, polymeric matrix interaction. Due to its success in the fabrication of nanofiber with a strong SHG response by electro-spinning, large molecular weight PMMA was chosen. Given the above considerations on the potential effects of polymer mobility structure with low molecular

weight PMMA were also grown. In addition, high weight PS that shares many characteristics (transmissivity, height molecular weight and strength) with PMMA matrices, was chosen to allow a further basis of comparison. Finally, PCL a semi-crystalline polymer, was used to explore the effects of the host matrix scaffold rigidity.

4.3 Surface characterization

4.3.1 FLIM

The second harmonic response of the electrospun doped nanofibers was characterized using a custom-made FLIM microscope [23]. The embedded *p*Na superstructures were probed by femtosecond pulses from a Kerr mode-locked Ti:Sapphire laser emitting at a central wavelength of 800 nm focused onto the sample by a 100x long-working distance infinity corrected objective. Emitted photons were collected by the same objective and a dichroic mirror was used to separate the fundamental and second harmonic photons. The second harmonic photons were directed to a double monochromator, before entering a multichannel photon multiplier tube (PMT) Hamamatsu to the emission's temporal decay profile. At each incident spot on the fiber mat, the second harmonic signal was obtained by accumulating the time correlated signals over a period of few seconds. A piezo-scan motor with an active x–y feedback was translated the sample with sub-micron spatial resolution. Overall the sample was scanned over a grid of (128 × 128 pixels) producing two-dimensional decay time intensity images. Custom LabView software was used to control the scanning process and for data acquisition.

4.3.2 SEM

The morphology, size and shape of *p*Na-PMMA nanofibres was verified by using a Nova Nano SEM 200 Scanning Electron Microscope (SEM) operated at an accelerating voltage of 10 kV.

4.3.3 AFM

Atomic force microscopy (AFM) imaging was performed under ambient conditions in air with a Nanosurf FlexAFM (Paralab SA, Portugal) instrument using a head with a range of 100×100 μm^2 area. The measurements were carried out in tapping mode employing a Tap190Al-G from BudgetSensors, with a resonance frequency ~190 kHz and a force constant of 48 N/m.

4.4 Bulk Characterization

4.4.1 Synchrotron radiation

The first generation of synchrotron radiation sources were the X-rays generated by the twisting magnets of the electron accelerators used in high-energy physics experiments. Gradually these sources were optimized by designing purpose built electron storage rings for dedicated high brilliance X-ray sources (2nd generation). Using electron undulator[1] radiation, which is brighter than that created by the bending magnets of storage rings, led to a 3rd generation of even more brilliant synchrotron radiation sources. Several large- scale facilities based on these advances were designed and constructed in the 1980s. Some examples are the European Synchrotron Radiation Facility (ESRF) in France, the Advanced Photon Source (APS) in the US and SPring-8 in Japan with electron storage ring energies of 6, 7 and 8 GeV, respectively. With the development of a multi-bend-achromat lattice, the electron beam in a storage ring can be more tightly focused, thus further improving the X-ray brilliance. The Swedish MAX IV, Italian Electra 2.0 and the Brazilian 5 SERIUS, three medium-sized storage rings, adopted this new technology to advance the performance of current storage ring sources. As of date, PETRA III in Germany is the most brilliant synchrotron radiation source.

Two separate synchrotron radiation studies of the fabricated *p*Na hybrid materials and self-assembling structures were carried out in an attempt to characterize the bulk nature of the respective materials.

The first experiment took place at the Austrian SAXS/WAXS end station in the Electra synchrotron, located at Trieste, Italy. The objective was characterize the morphology, orientation and micro strain of the *p*Na nanocrystals along the longitudinal axis of the polymeric nanofibers, correlating these results with the SHG response of these hybrid materials.

[1] The periodic array of dipole magnets forces the traveling electrons to undergo oscillations and thus to radiate energy as they traverse the magnet structure. This can lead to the production of intense, collimated and spectrally narrow X-ray radiation.

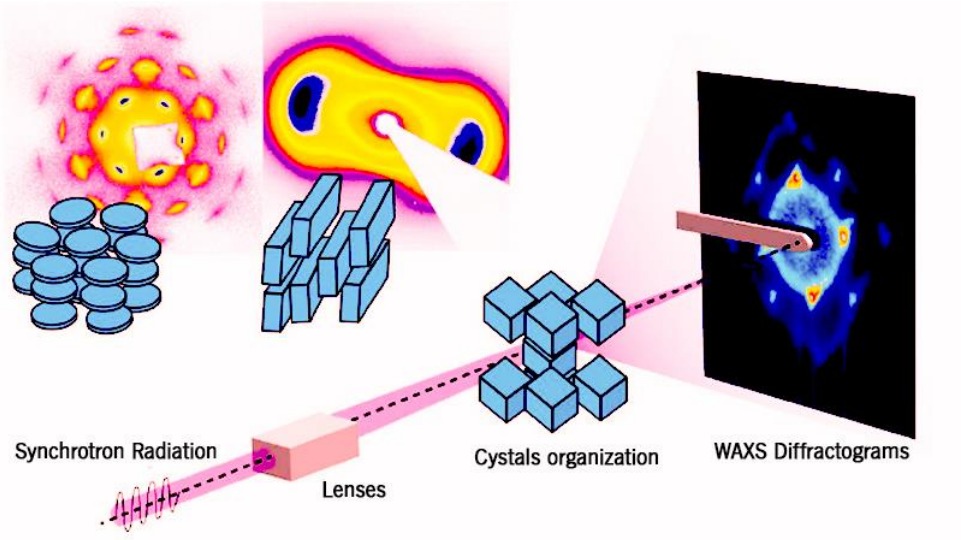

Figure 4.4 – Illustration of the synchrotron experiments carried out.

Wide angle X-ray scattering (WAXS) was employed using an energy of 8 keV. The highly collimated high intensity X-ray beam facilitated the acquisition of high-quality spectra with sufficient resolution to enable fitting using a Pseud-Voight function. In these X-ray studies, the detailed analysis of the peak width and shift enables one to infer the mean size and micro-strain experienced by the *p*Na nanocrystals.

The second experiment took place at the end station MINAXS in Petra III at DESY synchrotron, Hamburg, Germany [24]. The high spatial resolution, high intensity of photons, the micro dimension of the beam in combination with the detection microscope permitted acquiring spatially resolved micro X-ray diffractograms. The measurement technique, Scanning Nano diffraction WAXS, with an energy of 13 keV permitted correlating the structural information from the X-ray diffractograms with the different physical and optical characteristics of the *p*Na structures, as a function of spatial coordinates along the polymeric matrix. This association allows one to infer characteristics of the self-assembly mechanism as well the growth orientation and the crystallinity of the structures. The results are then correlated with the local second order NLO response of these low dimensional structures.

4.4.2 Polarimetry

A common technique used to measure the local second order NLO response of a variety of nonlinear materials is microscopic SHG polarimetry. The intensity and polarization of the detected

SHG can provide information regarding the domain shapes, orientation, domain phase and local symmetry of the material under study.

The setup used to preformed the SHG polarimetry is schematically represented in Figure 4.5. A linearly polarized femtosecond laser beam is used as the fundamental light with a central frequency, ω. The beam is focused onto the sample at normal incidence, while the SHG signal of frequency 2ω generated by the sample is collected in transmission and detected by a spectrograph.

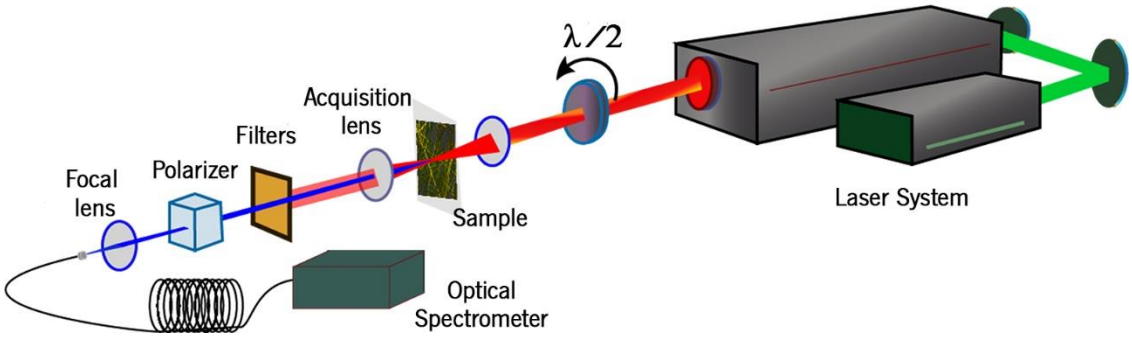

Figure 4.5 – Polarimetry setup.

In the case of *p*Na in electro-spun nanofibers, the incident fundamental beam enters the sample first and then is transmitted through the substrate. A thin glass cover slide with a thickness of $\approx 0.6\ \mathrm{mm}$ is used as support and substrate. These glass slides are amorphous hence non-SHG active while being highly transmissive to both fundamental and second harmonic light. In the case of the 2-dimensional *p*Na structures, the incident fundamental beam enters the cover slide first before impinging on the sample under study.

The dipoles ($\vec{\mu}$) excited by the incident fundamental light lie parallel to the image plane. To analyse the observed SHG intensities, it is convenient to introduce a laboratory coordinate systems (x y z), where z is parallel to the longitudinal axes of the nanofiber and y is the propagation direction of the incident fundamental light.

The corresponding electric field of the fundamental light has components in the laboratory frame of $(E_x, E_y, E_z) = (E_0 \cos\varphi,\ 0,\ E_0 \sin\varphi)$. Here, φ is the azimuthal angle of the fundamental light polarization, as depicted in Figure 4.6. The light-induced nonlinear polarization is given by

$$P^{2\omega} = \begin{pmatrix} P_x \\ P_y \\ P_z \end{pmatrix} = \chi_{ij} E_i^{\omega} E_j^{\omega} \tag{4.1}$$

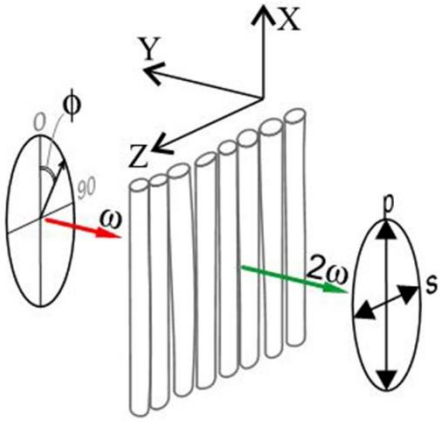

Figure 4.6 - Sketch of the SGH polarimetry experiment carried out in pNa-PMMA nanofibers.

In this particular case, the two experimentally accessible components of the SHG intensity generated at the surface of the nanocrystals of *p*Na are,

$$\begin{aligned} I_x^{2\omega} &\propto \hat{n}_x \left(\chi^{2s} \cdot P^{2\omega} \cdot \right)^2 \\ I_z^{2\omega} &\propto \hat{n}_z \left(\chi^{2s} \cdot P^{2\omega} \right)^2 \end{aligned} \tag{4.2}$$

Let $\hat{n}_i$ correspond to the orientation of the output analyser in position i expressed in the lab coordinate system. Here, χ^{2s} is the quadratic response of *p*Na nanocrystals surface polarization (small correction factors related to the Fresnel reflection and transmission coefficients are ignored). The polarimetry data show that the dominant SHG signal generated by the *p*Na nanocrystals, is oriented along the longitudinal fibre direction or laboratory z-axis. This implies a predominantly dipolar response with the two-fold polar axis aligned with the longitudinal fibre axis.

Following the work of Brevet [25], if the SHG power were to originated from a single surface of an embedded *p*Na crystal its magnitude would be given by

$$P_{2\omega}^{pNa} = \frac{\omega^2}{2\varepsilon_0 n_1^2 n_2 c^3} \left[\chi^{(2s)} \right]^2 \frac{1}{\mathcal{A}} P_{\omega}^2 \tag{4.3}$$

Assuming this to be the case we can estimate the magnitude of the nonlinear surface susceptibility, $\chi^{(2s)}$ of the *p*Na nanocrystals embedded within the nanofibers by comparing the response to that

of a $4\,\mathrm{mm}$ KDP crystal acquired under the same experimental conditions. The KDP crystal signal effectively allows us to calibrate the overall detection efficiency of our system.

In the case of KDP, within the plane wave approximation, the generated SHG power is described by the well-known expression,

$$P_{2\omega}^{KDP} = \frac{2\omega^2}{\varepsilon_0 n_1^2 n_2 c^3}\left[d_{eff}\right]^2 \frac{L^2}{\mathcal{A}}\mathrm{sinc}^2\left(\frac{\Delta kL}{2}\right)P_{\omega}^2 \tag{4.4}$$

Here $\Delta k = 2k_1 - k_2$ is the wave vector mismatch between the fundamental beam (k_1) and the second harmonic beam (k_2) within the medium, $\mathcal{A}$ is area of the focused beam waist and d_{eff} is the effective nonlinear coefficient. For type I phase matching in KDP at the wavelength of the fundamental beam, the appropriate second order coefficient is $d_{eff} = \sin(\theta_{pm})d_{36}$, where the phase matching angle is $\theta_{pm} = 44.9^{\circ}$ and $d_{36} = 0.39\ pm\cdot \mathrm{V}^{-1}$ [26]. Due to the birefringence of the KDP crystal, there is a walk-off angle between the wave-vector propagation and the direction of energy flow. In KDP at the phase matching orientation for the fundamental beam incident light this walk-off angle is $28\ mrads$ and will reduce the efficiency by roughly a factor of 2 under our conditions.

Taking this in consideration and assuming that the observed *p*Na nanofibre SHG signal is due to a single *p*Na nanocrystal, one can estimate the effective surface quadratic response via the relation.

$$\chi^{(2s)} = d_{eff}^{KDP} L\sqrt{\frac{\mathcal{P}_{2\omega}^{pNa}}{2\,\mathcal{P}_{2\omega}^{KDP}}} \tag{4.5}$$

4.4.3 Raman spectroscopy

Raman spectroscopy is a respected technique for probing the chemical composition of materials. It is widely applied in the chemical analysis of molecular species [27]. Being sensitive to the structure of chemical bonds, it is widely used as a characterization technique in organic condensed matter studies. Raman spectroscopy is a non-invasive and label-free tool, intrinsic to the molecules contained in the respective sample, effectively probing the molecular vibrational properties. Initially the application of the techniques was limited by low spatial resolutions due to the longer wavelength involved and the vibrational absorption of the matrix and environmental atmosphere. However, the

use of powerful well-collimated laser sources has allowed increased spatial resolution and improved signal to noise ratios. Currently high resolution Raman spectroscopy provides good molecular specificity with high-speed analysis making it a favourite imaging technique in the bio sciences.

Raman spectroscopy is associated with a coupling between the incident photons and the natural vibrionic modes of the sample. This coupling allows the incident light with a frequency (ν), to excite one of the vibrational modes, leading to a scattered photon with a lower frequency at (ν'). By energy conservation the difference in energy between the incident and scattered photon is equal to a quanta of the excited vibrational mode.

$$\Delta E_{vi} = h(\nu - \nu') \tag{4.6}$$

Typically in Raman spectroscopy, an incident laser beam is focused tightly onto the sample. The scattered photons are then collected by a condenser lens and sent into a spectrometer. A double monochromator is usually used to ensure adequate discrimination against the incident light and to resolve the various Raman peaks. Often, a cooled CCD array is used as a detector.

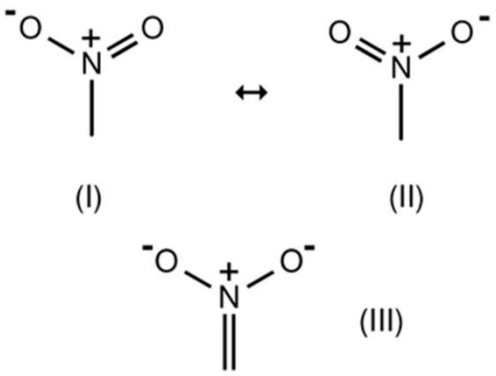

Figure 4.7 – Resonance structure for *p*Na.

Information regarding the vibrational modes that can be sensitive to the phase and local structural confinement of the *p*Na moelcules inside of the polymeric nanofiber produced by electrospinning was obtained using a high resolution dispersive Raman microscope Horiban Jobin Yvon, LabRAM HR with a CW laser with a wavelength of $\lambda = 514.5\ \mathrm{nm}$ at room temperature. The same setup was used as well to study the 2-dimenstional *p*Na structures growth in different polymeric matrices.

In the case of *p*Na the nitro group can be viewed as a hybrid of the two resonance structures (I) and (II) represented in figure 4.7. However, it is also necessary to take into consideration the canonical resonant structure (III) of the nitro group because it is the responsible for most of the chemical properties of the aromatic compounds such as acidity, reaction speed, spectral shift and high polarizability [28]. The positive charge of the nitrogen atom leads to a high electronegativities of the electron cloud which manifests as a large dipole moment. In a simplified two-state model, the electronic state of *p*Na can be viewed as a linear combination between the resonant structures (I) and (II) leading to the neutral state $\left(\Psi_{\mathrm{VB}}\right)$ and the zwitterionic structure $\left(\Psi_{\mathrm{CT}}\right)$ based on resonance structure (III) [29,30].

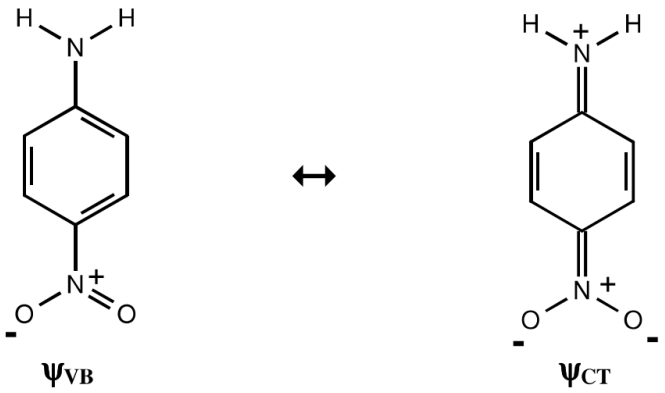

Figure 4.8 – The two characteristic electronic structures for *p*Na.

The local environment can provoke mixing between these states and in general, the electronic ground state $\left(\Psi_{g}\right)$ and the first electronic state $\left(\Psi_{\mathrm{E}}\right)$ of *p*Na will be given as the linear combination of these two structures,

$$\begin{aligned}\Psi_{g} &= \left(1-f\right)^{\frac{1}{2}}\Psi_{\mathrm{VB}} + f^{\frac{1}{2}}\Psi_{\mathrm{CT}} \\ \Psi_{\mathrm{E}} &= f^{\frac{1}{2}}\Psi_{\mathrm{VB}} - \left(1-f\right)^{\frac{1}{2}}\Psi_{\mathrm{CT}}\end{aligned} \tag{4.7}$$

Ordinarily, the ground state is mostly the neutral state Ψ_{VB} while the exited state is predominantly the zwitterionic state Ψ_{CT}. This implies a certain amount of charge transfer when the molecule is excited. Furthermore, in polar environments the molecule is more stable in zwitterionic structure.

In this case the molecule presents a large transition diploe moment $\left(\mu_{ge}\right)$. The intensity of the Raman $\left(I_{\mathrm{R}}^{2}\right)$ spectrum is direct related with the resonate structures of the molecule

$$I_{\mathrm{R}}^{2}\alpha\mu_{ge}=\int_{-\infty}^{+\infty}\Psi_{g}\mathrm{M}\Psi_{e}\,d\tau \tag{4.8}$$

Where M is the vector moment and $d\tau$ is the product of the volume of all atomic elements.

Using this simple model one can understand how the Raman spectrum might be influenced by the phase and local environment of the *p*Na molecule. However, several peaks have nearly the same frequencies independent of its state, they are listed in table 3 [31].

Table 3. Raman frequency of the coincident peaks in bulk *p*Na and the electro-spun nanofibres together with the identification of the corresponding vibrational mode.

Raman Shift (cm^{-1})	Relative Intensity (Nanofibres)	Relative Intensity (bulk)	Vibrational modes[a]
860	0.34	0.24	$\delta(NO_2)$
1109	0.34	0.12	ν(C-NO_2)
1137	0.12	0.08	φ(13)
1178	0.12	0.07	φ(9a)
1397	0.07	0.08	φ(19b)
1452	0.09	0.06	φ(19a)
1507	0.11	0.06	$\nu_{as}(NO_2)$
1598	0.20	0.08	φ(8a)

[a] ν =stretching, δ =in-plane deformation, γ =out-of-plane deformation, φ vibrations of benzene; nomenclature according to G. Varsanyi .

The reported Raman spectra of *p*Na show several anomalies, some of them due to its molecular structure, others to its crystalline structure [29,30,32,33]. In the region 1270-1350 cm^{-1} differences are greatest, both for the frequencies and for the intensities. In the solid phase, the ν_3 line 1287 cm^{-1} (assigned to a ring vibration), is by far the strongest in the Raman spectrum. The contrary behaviour is present for the $\nu_{NO_2}^{s}$ line at 1338 cm^{-1} of the group NO_2. In the molten fase these two Raman lines are strong but in solutions the ν^3 line is no longer visible while the $\nu_{NO_2}^{s}$ line splits into two components, whose intensities depend on the nature of the solvent and on the concentration of *p*Na [34].

4.5 Bibliography

1. M. N. O'Brien, M. R. Jones, and C. A. Mirkin, "The nature and implications of uniformity in the hierarchical organization of nanomaterials," Proc. Natl. Acad. Sci. **113**(42), 11717–11725 (2016).

2. P. Wang, Y. Wang, and L. Tong, "Functionalized polymer nanofibers: A versatile platform for manipulating light at the nanoscale," Light Sci. Appl. **2**(OCTOBER), e102 (2013).

3. S. Editor and D. J. Lockwood, *Electrospun Nanofibers for Energy and Environmental Applications* (2014).

4. H. Liu, J. B. Edel, L. M. Bellan, and H. G. Craighead, "Electrospun polymer nanofibers as subwavelength optical waveguides incorporating quantum dots.," Small **2**(4), 495–9 (2006).

5. K. M. Sawicka and P. Gouma, "Electrospun composite nanofibers for functional applications," J. Nanoparticle Res. **8**(6), 769–781 (2006).

6. H. Cho, S. Y. Min, and T. W. Lee, "Electrospun organic nanofiber electronics and photonics," Macromol. Mater. Eng. **298**(5), 475–486 (2013).

7. J. Xu, C. Liu, P. C. Hsu, K. Liu, R. Zhang, Y. Liu, and Y. Cui, "Roll-to-Roll Transfer of Electrospun Nanofiber Film for High-Efficiency Transparent Air Filter," Nano Lett. **16**(2), 1270–1275 (2016).

8. R. Sahay, P. S. Kumar, R. Sridhar, J. Sundaramurthy, J. Venugopal, S. G. Mhaisalkar, and S. Ramakrishna, "Electrospun composite nanofibers and their multifaceted applications," J. Mater. Chem. **22**(26), 12953 (2012).

9. N. Bhardwaj and S. C. Kundu, "Electrospinning: A fascinating fiber fabrication technique," Biotechnol. Adv. **28**(3), 325–347 (2010).

10. B. Ghorani and N. Tucker, "Fundamentals of electrospinning as a novel delivery vehicle for bioactive compounds in food nanotechnology," Food Hydrocoll. **51**, 227–240 (2015).

11. C. L. Zhang and S. H. Yu, "Nanoparticles meet electrospinning: Recent advances and future prospects," Chem. Soc. Rev. **43**(13), 4423–4448 (2014).

12. K. H. Lee, H. Y. Kim, H. J. Bang, Y. H. Jung, and S. G. Lee, "The change of bead morphology formed on electrospun polystyrene fibers," Polymer (Guildf). **44**(14), 4029–4034 (2003).

13. H.-S. Wang, G.-D. Fu, and X.-S. Li, "Functional polymeric nanofibers from electrospinning.," Recent Pat. Nanotechnol. **3**, 21–31 (2009).

14. Y.-F. Qian, Y. Su, X.-Q. Li, H.-S. Wang, and C.-L. He, "Electrospinning of Polymethyl Methacrylate Nanofibres in Different Solvents," Iran. Polym. J. **19**(2), 123–129 (2010).

15. Y. Liu, L. Dong, J. Fan, R. Wang, and J. Y. Yu, "Effect of applied voltage on diameter and morphology of ultrafine fibers in bubble electrospinning," J. Appl. Polym. Sci. **120**(1), 592–598 (2011).

16. S. Piperno, L. Lozzi, R. Rastelli, M. Passacantando, and S. Santucci, "PMMA nanofibers production by electrospinning," Appl. Surf. Sci. **252**(15), 5583–5586 (2006).

17. C. B. Walsh and E. I. Franses, "Ultrathin PMMA films spin-coated from toluene solutions," Thin Solid Films **429**(1–2), 71–76 (2003).

18. S. a. Denev, T. T. a Lummen, E. Barnes, A. Kumar, and V. Gopalan, "Probing ferroelectrics using optical second harmonic generation," J. Am. Ceram. Soc. **94**(9), 2699–2727 (2011).

19. R. W. Munn, "Molecular crystal surface dielectric properties: Microscopic theory for linear response," J. Chem. Phys. **97**(6), 4532 (1992).

20. J. N. Sherwood and G. S. Simpson, "The growth, structural and optical characterization of large area, single crystalline thin films of 3-nitroaniline (mNA)," J. Cryst. Growth **128**(1–4 PART 2), 981–985 (1993).

21. S. Manetta, M. Ehrensperger, C. Bosshard, and P. Günter, "Organic thin film crystal growth for nonlinear

optics: Present methods and exploratory developments," Comptes Rendus Phys. **3**(4), 449–462 (2002).

22. S. Conti and M. Cecchini, "Predicting molecular self-assembly at surfaces: a statistical thermodynamics and modeling approach," Phys. Chem. Chem. Phys. **18**(46), 31480–31493 (2016).

23. C. Bernardo, M. Belsley, E. de Matos Gomes, H. Gonçalves, D. Isakov, F. Liebold, E. Pereira, V. Pires, A. Samantilleke, M. Vasilevskiy, and P. Schellenberg, "A versatile fluorescence lifetime imaging system for scanning large areas with high time and spatial resolution," in *Proc. SPIE*, M. F. P. C. Martins Costa and R. N. Nogueira, eds. (International Society for Optics and Photonics, 2014), **9286**, pp. 928637–928638.

24. A. Buffet, A. Rothkirch, R. Döhrmann, V. Körstgens, M. M. Abul Kashem, J. Perlich, G. Herzog, M. Schwartzkopf, R. Gehrke, P. Müller-Buschbaum, and S. V. Roth, "P03, the microfocus and nanofocus X-ray scattering (MiNaXS) beamline of the PETRA III storage ring: The microfocus endstation," J. Synchrotron Radiat. **19**(4), 647–653 (2012).

25. P. F. Brevet, "Phenomenological three-layer model for surface second-harmonic generation at the interface between two centrosymmetric media," J. Chem. Soc. Faraday Trans. **92**(22), 4547 (1996).

26. G. Anandha babu, R. P. Ramasamy, and P. Ramasamy, "Synthesis, crystal growth and characterization of an efficient nonlinear optical D-??-A type single crystal: 2-Aminopyridinium 4-nitrophenolate 4-nitrophenol," Mater. Chem. Phys. **117**(1), 326–330 (2009).

27. H. G. M. Edwards, *Modern Raman Spectroscopy—a Practical Approach.Ewen Smith and Geoffrey Dent. John Wiley and Sons Ltd, Chichester, 2005. Pp. 210. ISBN 0 471 49668 5 (Cloth, Hb); 0 471 49794 0 (Pbk)* (2005), **36**(8).

28. T. Gunaratne, J. R. Challa, and M. C. Simpson, "Energy flow in push-pull chromophores: vibrational dynamics in para-nitroaniline," ChemPhysChem **6**(6), 1157–1163 (2005).

29. M. Harrand, "Raman study on para nitroaniline single crystal. II: Internal Vibrations," J. Raman Spectrosc. **4**(1), 53–73 (1975).

30. M. Harrand, "Raman study on p-nitroaniline: Molecular structure in the molten phase," J. Raman Spectrosc. **8**(3), 161–164 (1979).

31. G. Varsányi, *Vibrational Spectra of Benzene Derivatives*, 1st editio (Academic Press, 1969).

32. F. Marlow, W. Hill, J. Caro, and G. Finger, "Raman-Study on P-Nitroaniline in Channels of the Molecular-Sieve Alpo(4)-5," J. Raman Spectrosc. **24**(9), 603–608 (1993).

33. J. Xia, L. Zhu, Y. Feng, Y. Li, Z. Zhang, L. Xia, L. Liu, and F. Ma, "Unusual Raman spectra of para-nitroaniline by sequential Fermi resonances," Spectrochim. Acta - Part A Mol. Biomol. Spectrosc. **120**(2), 616–620 (2014).

34. W. S. Wang, M. D. Aggarwal, J. Choi, T. Gebre, A. D. Shields, B. G. Penn, and D. O. Frazier, "Solvent effects and polymorphic transformation of organic nonlinear optical crystal L-pyroglutamic acid in solution growth processes I. Solvent effects and growth morphology," J. Cryst. Growth **198–199**(PART I), 578–582 (1999).

5 Papers Reprints

In the next chapter are present the reprints of the papers published during this thesis. We discussed the properties of hybrid nanofibers and the *p*Na structures, the nano crystals size, the influence of surface, bulky strain, polymeric matrix, depositions parameters and growth orientation.

Efficient second harmonic generation by *para*-nitroaniline embedded in electro-spun polymeric nanofibres

Hugo Gonçalves[1], **Inês Saavedra**[1], **Rute AS Ferreira**[2], **PE Lopes**[3], **Etelvina de Matos Gomes**[1], **Michael Belsley**[1]

[1] Centre of Physics, University of Minho, Campus de Gualtar, 4710-057 Braga, Portugal

[2] Department of Physics, CICECO – Aveiro Institute of Materials, University of Aveiro, 3810-193 Aveiro, Portugal

[3] Institute for Polymers and Composites/i3N, University of Minho, Guimarães, Portugal

E-mail: belsley@fisica.uminho.pt

Abstract: Intense well polarized second harmonic light was generated by Poly(methyl methacrylate) nanofibres with embedded *para*-Nitroaniline nanocrystals. Subwavelength diameter fibres were electro-spun using a 1:2 weight ratio of chromophore to polymer. Analysis of generated second harmonic light indicates that the *p*Na molecules, which nominally crystalize in the centrosymmetric space group, were organized into noncentrosymmetric structures leading to a second order susceptibility dominated by a single tensor element. Under the best deposition conditions, the nanofibrers display an effective nonlinear optical susceptibility approximately two orders of magnitude greater than that of potassium dihydrogen phosphate. Generalizing this approach to a broad range of organic molecules with strong individual molecular second order nonlinear responses, but which nominally form centrosymmetric organic crystals, could open a new pathway for the fabrication of efficient sub-micron sized second harmonic light generators.

PACS: 42.65.-k Nonlinear optics**; 42.65.An** Optical susceptibility; hyperpolarizability, **42.65.Ky** Frequency conversion; harmonic generation; **42.70.Jk** Polymers and organics

1. Introduction

New materials with tailored linear and nonlinear optical (NLO) properties are actively being sought to extend the frontiers that limit many photonic devices. Currently the majority of commercial nonlinear photonic components are based on inorganic materials [1]. Despite the successful development of many new inorganic crystalline materials over the past several decades, the applications of these materials is often limited by the magnitude of the available optical nonlinearities as well as the associated fabrication costs. In particular, efficient generation of second harmonic light by sub-micron sized systems is not routinely available from inorganic materials. Recently, several different processing approaches to extend the range of available nonlinear optical materials have been explored, including self-assembly [2,3], poling [4], lithography [5,6], molecular beam epitaxy [7] and electrospinning deposition [8-12]. Concurrently, researchers have developed a variety of alternative building blocks such as metallic nanoparticles[13], semi-conductors quantum dots [14], 2D-Materials [15] and tailored organic molecules [16].

In particular, organic systems have been widely investigated for nonlinear optical applications. They possess several attractive features including their low cost, fast, large nonlinear responses over a broad frequency range and tailorability [4,16]. A paradigmatic example is the organic molecule of *para*-Nitroaniline (*p*Na) [17-20]. It has a delocalized π-electron system and unsaturated bridge linking a donor amino group (NH_2) and an acceptor nitro group (NO_2). The delocalization of the π-electrons leads to an asymmetric charge distribution resulting in a strong molecular hyperpolarizability (β) [21]. Unfortunately, because it crystallizes in a centrosymmetric space group $\left(P2_1/n\right)$ [17], the bulk second order nonlinear response of *p*Na crystals vanishes. This commonly occurs in donor-pi bridge-acceptor organic crystals: the dominant dipole–dipole interactions result in a pairwise, side-by-side antiparallel molecular alignment within the unit cell [22]. Experimentally, several different approaches have sought to achieve useful SHG when employing *p*Na as the active molecular building block [10,18,20,23]. These range from modifying the surface of *p*Na crystals [18] to the incorporation of the organic dye within carbon nanotube structures [24]. Recently we reported observing strong SHG from *p*Na embedded in electro-spun poly(L-lactic acid) (PLLA) polymer nanofibres [10]. Here we report on similar results obtained using Poly(methyl methacrylate) (PMMA) as the polymeric host. Contrary to the situation with PLLA, the pNa-PMMA fibres produce an intense well-polarized second harmonic response dominated by a single tensor element of the effective second order susceptibility.

Electrospinning deposition is a versatile technique with deposition parameters that can be tuned to induce long range molecular order organic molecular dopants, leading to enhanced optical and NLO coefficients

[13,25]. The sub wavelength size of the resultant hybrid nanostructures promotes localized coherent interactions in the transverse direction and allows as well as waveguiding effects along the longitudinal direction [26].Furthermore, the technique is relatively low cost and can be easily scaled-up to an industrial level [9].

In this study, *p*Na molecules were embedded in a one dimensional (1D) nanostructured Poly(methyl methacrylate) (PMMA) matrix, using different deposition rates during the electrospinning process. With this technique, the growth of the *p*Na crystals is encouraged along the longitudinal axis. Strong coherent SHG radiation was produced when 100fs pulses from a mode-locked Ti:Sapphire laser operating at a central wavelength of 800nm were focused onto these nanofibres. The polarization dependence of the SHG generated by these fibres allows us to comment on how the electrospinning deposition rate influences the degree of *p*Na alignment with the fibres. The complementary characterization techniques of Scanning Electron Microscope (SEM), X-ray diffraction, Raman spectroscopy, Fluorescence Lifetime Imaging Microscopy (FLIM) and Hyperspectral Microscopy were employed to obtain insights regarding the local nanostructured environment of the embedded *p*Na molecules.

2. Methods

2.1 Materials

Para-nitroaniline (*p*Na) was purchased from Sigma Chemical Co and used as received. Poly(methyl methacrylate) (PMMA, Mw 120000) was purchased from Alfa Aesar. The raw materials were dissolved in dimethyl formamide (DMF) and toluene at a 1:2 volume ratio. DMF (C_3H_7NO, 99.8%) and toluene ($C_6H_5CH_3$, 99.8%) were purchased from Sigma-Aldrich as used as received. The relative weight ratio of *p*Na to PMMA in the final precursor solution was 1:2. The prepared solutions were stirred for several hours under ambient conditions prior to deposition by electrospinning.

2.2 Nanofibre Production

The polymeric nanofibres were electro-spun. The precursor solution was loaded into a syringe with its needle connected to the anode of a high voltage power supply (Spellmann CZE2000). To produce the in-plane aligned fibre arrays, 17 kV were applied to the needle while the grounded rotating drum collector was rotated at 100 rpm. In this technique, the nanofibres are the result of a rapid solidification of a jet of polymeric solution created by the intense electric field between the tip and the support. The nanofibres are deposited on a glass slide attached to a rotating drum collector, while the distance between anode and collector was 12 cm. Precursor solution flow rates of 0.05 mL/h, 0.40 mL/h and 0.75 mL/h were used. These rates were controlled by a dedicated syringe pump.

2.3 Material Characterization

The morphology, size and shape of *p*Na-PMMA nanofibrers was verified by using a Nova Nano SEM 200 Scanning Electron Microscope (SEM) operated at an accelerating voltage of 10 kV. A homebuilt Fluorescent Lifetime Image Microscope (FLIM) [27] was used as a complementary analysis of the morphology and alignment of the *p*Na-PMMA nanofibres. FLIM analysis gives information about the individual SHG response of each nanofibre.

Crystallinity and crystallographic orientation of the *p*Na nanocrystals inside the nanostructured fibres was studied by X-ray diffraction. The X-ray diffraction pattern of nanofibres was measured from $\theta - 2\theta$ scans recorded between 10 and 60° on a Philips PW-1710 X-ray diffractometer using Cu-K_α radiation of wavelength 1.5406 Å. The lattice planes parallel to the substrate surface were determined from the *q* vector perpendicular to the nanofibres mat plane and thus perpendicular to the longitudinal nanofibre axes.

A high-resolution Raman spectrometer, Horiba LabRAM HR Evolution confocal microscope using a laser excitation of 532 nm (2.33 eV), was employed to characterize the local molecular order and orientation of the *p*Na inside of the PMMA host matrix. A 100x objective lens was used to focus the laser onto the sample. Polarized Raman spectra were obtained at room temperature between 600-1800cm^{-1}.

The bright field microscopic images were recorded using an Olympus BX51 microscope (10×, 50×, 100× objectives), in the transmission mode, equipped with a digital CCD camera (Retiga 4000R, QImaging) used to capture the microphotographs (exposure time: 0.1 s) of the samples under illumination of white light of a DC regulated illuminator (DC-950, Fiber-Lite). The dark field images were acquired by replacing the standard microscope condenser, used for bright field transmission mode, by the CytoViVa enhanced darkfield illumination system. The hyperspectral microscope images were obtained with a digital camera (IPX-2M30, Imperx) coupled to a spectrograph (V10E 2/3″, Specim, 30 μm slit, nominal spectral range of 400–1000 nm, and nominal spectral resolution of 2.73 nm). A UV-IR Cut Filter (IF 486, Schneider Kreuznach) with transmission range from 390 to 690 nm was placed in front of the cameras. Each pixel field-of-view on the hyperspectral images corresponds to an area of 128×128 nm^2 on the sample plane.

2.4 Polarimetry measurements

The SHG response of the *p*Na-PMMA nanofibres was analysed by polarimetry measurement using the experimental set-up shown schematically in figure 1. The incident fundamental light at frequency ω was provided by a femtosecond Ti:Sapphire mode-locked laser (Coherent Mira 900F) pumped by a frequency doubled CW Neodymium-laser (Coherent Verdi 5W), with a 100 femtosecond (fs) temporal pulse width and a central wavelength of 800nm. The measurement consists in illuminating *p*Na-PMMA nanofibres with

linearly polarized fundamental light and analysing the polarization of the transmitted SHG field. An achromatic half-wave plate ($\lambda/2$) is placed before a 50mm focal length plano-convex lens, in order to continuously vary the polarization direction of the incident light (0 – 360º). The generated SHG field is collected by a microscope objective 100× Mitutoyo Plan Infinity-Corrected Long working distance objective (NA=0.7). A set of filters was used to eliminate the transmitted fundamental beam intensity and select the SHG field with a central frequency of 2ω. A polarizer was used to analyse the polarization of the generated SHG light. The polarizer was fixed to be either parallel (q-p configuration) or perpendicular (q-s configuration) to the nanofibre's longitudinal axis. The analysed SHG field was recorded by focusing the beam onto a multimode fibre optic cable coupled to the entrance slit of a 0.3m imaging spectrograph Andor Shamrock SR-303i, with 0.20nm resolution.

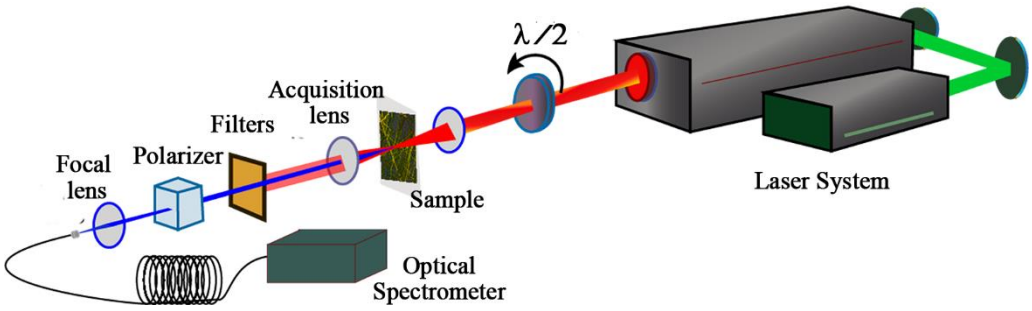

Figure 1. Polarimetry Setup. The sample is excited by a linearly polarized Ti:Sapphire laser beam. The polarization of the incident beam is continuously varied using an achromatic half-wave wave plate (WP – λ/2). After passing through a fixed polarization analyser the second harmonic signal is detected using a cooled CCD array coupled to a 0.3 m spectrograph.

3. Results and Discussion

3.1 Structural, Morphology and filled content analysis

The morphology, size and shape of the *p*Na-PMMA nanofibers were investigated using SEM. As shown in figure 2 and summarized in table 1. One clearly sees that they present a homogeneous cylindrical morphology with sub-micron diameters. A crucial aspect is the absence of *p*Na crystals grown outside of the PMMA fibres confirming that the SHG signal comes from *p*Na molecules located inside the polymeric matrix. No external beads are observed [28].

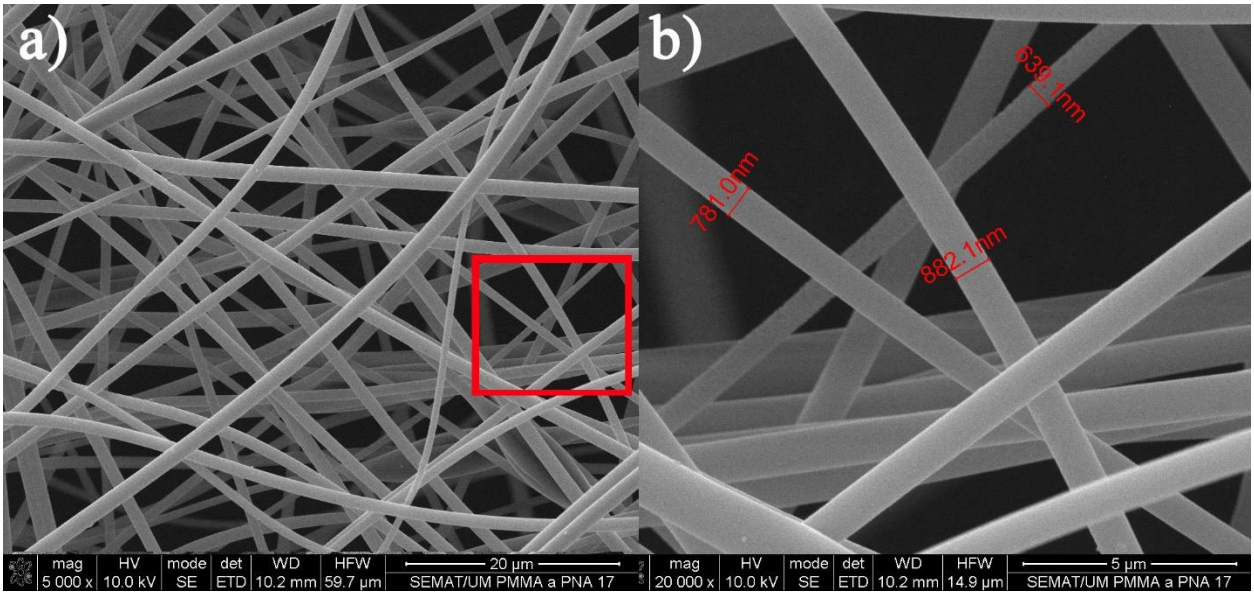

Figure 2. SEM image of *p*Na-PMMA nanofibres (a) deposited by electrospinning using a deposition rate of 0.05 mL/h. (b) Detail of the selected area in the left image with an indication of a few selected nanofibre diameters.

The high spatial and time resolution of the FLIM microscopy setup allows the measurement of the SHG signal of each individual nanofibre (figure 3). Illuminating the nanofibres by the femtosecond laser with a central wavelength of 800 nm the resulting second harmonic response (SHG) near 400 nm is collected and recorded. Each pixel of the image in figure 3 is coloured and corresponds to a single decay profile at the respective pixel's spatial coordinate. The overall temporal response is represented in the histogram. The prompt SHG emission is characteristic of a scattering process in a well-defined temporal window with a width that is close to the instrumental response time of the detection system. This eliminates the possibility of other effects, such as fluorescence induced by the absorption of two photons. FLIM microscopy demonstrates that each individual *p*Na-PMMA nanofibre presents a second order nonlinear response.

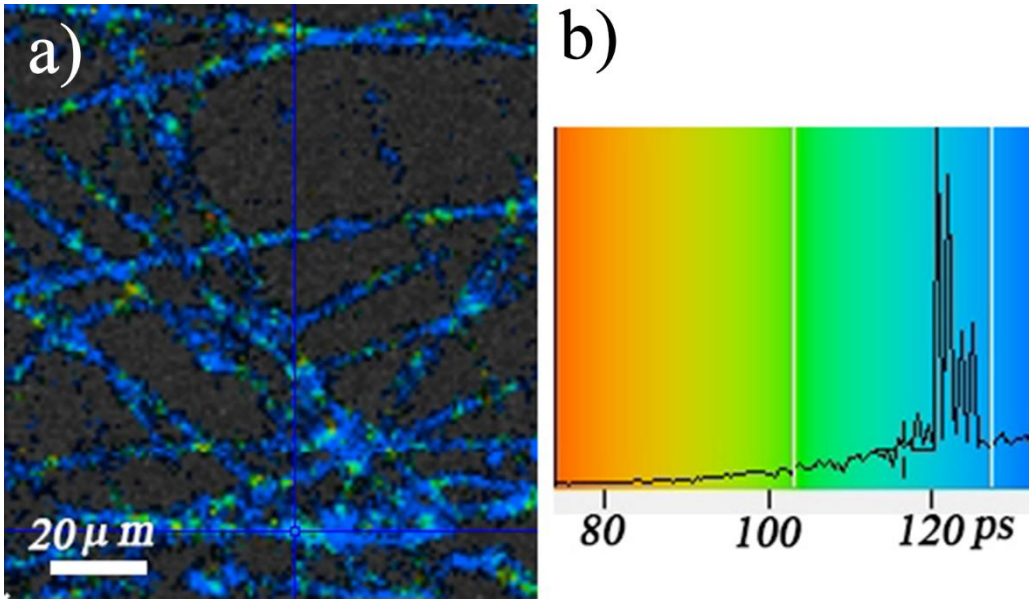

Figure 3. (a) Coloured FLIM microscope image of *p*Na-PMMA nanofibres using a deposition rate of 0.05 mL/h. (b) Temporal histogram of the SHG response. The sharp peaks in the histogram, with widths close to the instrument response time of the system, are a characteristic of a prompt nonlinear effect.

The mean diameter of the *p*Na-PMMA nanofibres tends to diminish as the deposition rate increases (table 1). Furthermore, the distribution of diameters broadens at higher deposition rates.

Table 1. Mean diameter of the *p*Na-PMMA nanofibres as a function of the deposition rate.

Deposition rate (mL/h)	**Mean** Fibre **Diameter (nm)**
0.05	786 ± 45
0.40	594 ± 64
0.75	578 ± 140

X-ray diffraction spectra acquired on *p*Na-PMMA fibre mats for each of the deposition rates listed in table 1 is shown in figure 4. The acquired diffraction patterns show evidence of well aligned nanocrystals dominated by a strong peak corresponding to the plane with the Miller indices (202) which is parallel to *p*NA natural cleavage plane (101) [19]. After performing a baseline subtraction, a Lorentzian was fit to the (202) peak for the different deposition rates as shown in the inset of figure 4.

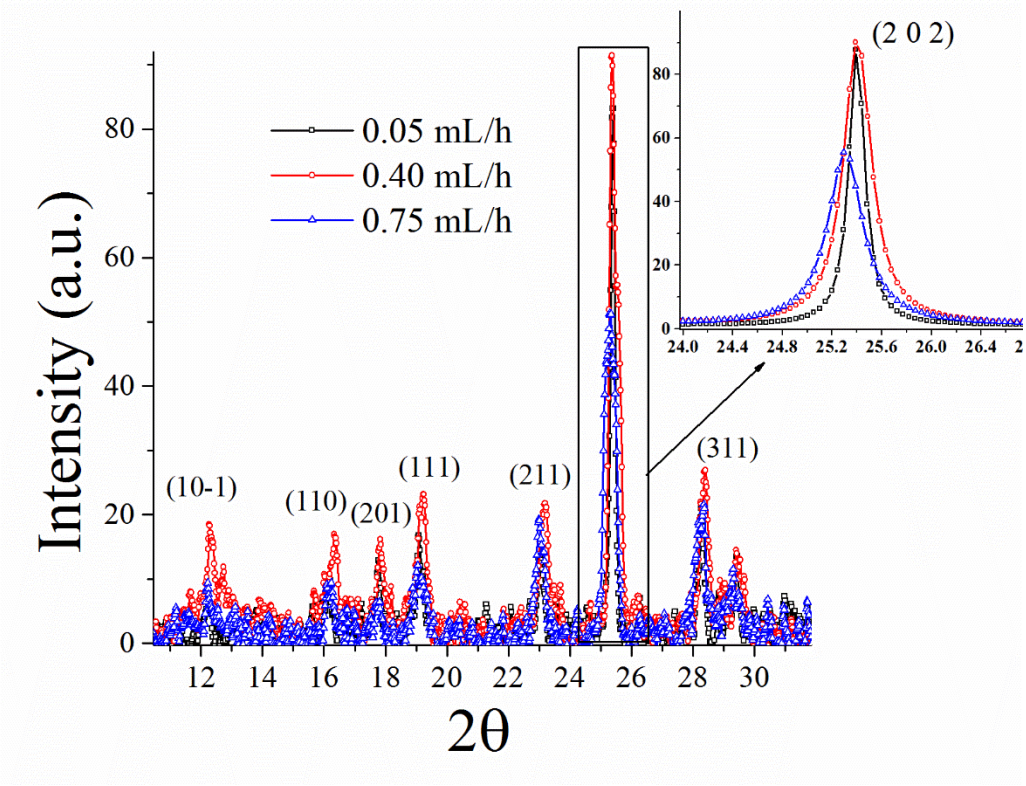

Figure 4. The X-Ray diffraction peaks of the PMMA nanofibres doped with *p*Na, deposited at different rates. (Inset) Lorentzian fit to the peak corresponding to dominant peak with the Miller indices (202).

The Lorentzian fit allows us to quantify the broadening of the (202) diffraction peak as the deposition rate is increased. This broadening could be due either to a reduction in the mean size of the *p*Na nanocrystals or an increase in strains to which they are subjected. When size effects dominate the broadening, the Scherrer equation [29] can be used to relate the width of the *hkl* diffraction peak in radians, to the mean crystal size through the equation:

$$\beta_{hkl} = \left(\frac{k\lambda}{D\cos(\theta)} \right) . \qquad (1)$$

Here D is the crystal size in the direction perpendicular to the lattice planes, λ is the wavelength of the radiation (1.5406Å), θ is the diffraction angle in radians and k numerical factor frequently referred to as the crystallite-shape factor. In the absence of detailed shape information, k=0.9 is generally accepted as a good approximation. This allows us to estimate a minimum size for the *p*Na crystals.

Table 2. The experimental values of β_{202} obtained by the Lorentzian peak fit of cleavage plane with the Miller indices (202) for the different deposition rate and the corresponding estimate for lower limit of the mean crystal size using equation 1.

Deposition rate (mL/h)	β_{202} (radians)	**Minimum** pNa **crystal size (nm)**
0.05	0.15	54.26
0.40	0.28	29.07
0.75	0.37	22.01

The experimental values of β_{202} and the corresponding minimum crystal size listed in table 2 together with the SEM results presented in table 1, suggest that nanofibres deposited at higher rates lead to thinner nanofibres containing smaller embedded *p*Na nanocrystals. Generally, thinner nanofibres are the result of a fast and efficient solvent evaporation [9] as the nanofibres solidify on their way to the grounded collection substrate. Another possible consequence of the rapid solidification can be the increase of the surface tension generating micro-strains, which in turn broadens the diffraction peaks. For a deposition rate of 0.75 mL/h the peak broadening is accompanied by a decrease of the peak area and maximum peak height. This suggests a lower degree of crystallinity accompanied by some combination of a decrease in the average size of the nanocrystals and an increase in the presence of micro-strains. The 0.05 mL/h deposition rate leads to a significantly larger lower limit on the mean crystal size. At this deposition rate the average nanofibre diameter is larger, consistent with a slower evaporation rate which should lead to more uniform crystallization within the nanofibres. The preferential orientation corresponds to the plane with Miller indices (202) which is parallel to the natural cleavage plane (101). Theoretical calculations of surface quadratic susceptibilities in *p*Na crystals [10,19] indicate that (101) and (202) surface terminations correspond to large quadratic susceptibilities and consequently strong surface nonlinear responses.

Hyperspectral microscopy was used to ascertain whether the concentration of *p*Na varied significantly along the fibres. Figure 5a shows an optical image of *p*Na fibres on a microscope slide. The fibre region was magnified (area marked with a rectangle) and the resulting hyperspectral image of a few *p*Na fibres under white light excitation is depicted in figure 5c. The hyperspectral curves collected randomly along the fibres (within pixels of size 128x128 nm^2) are spectrally uniform consistent with an overall homogenous concentration of embedded *p*Na molecules. We note that the intensity variations present in figure 5a, primarily occurs in regions of overlapping fibres which increases the amount of light scattered.

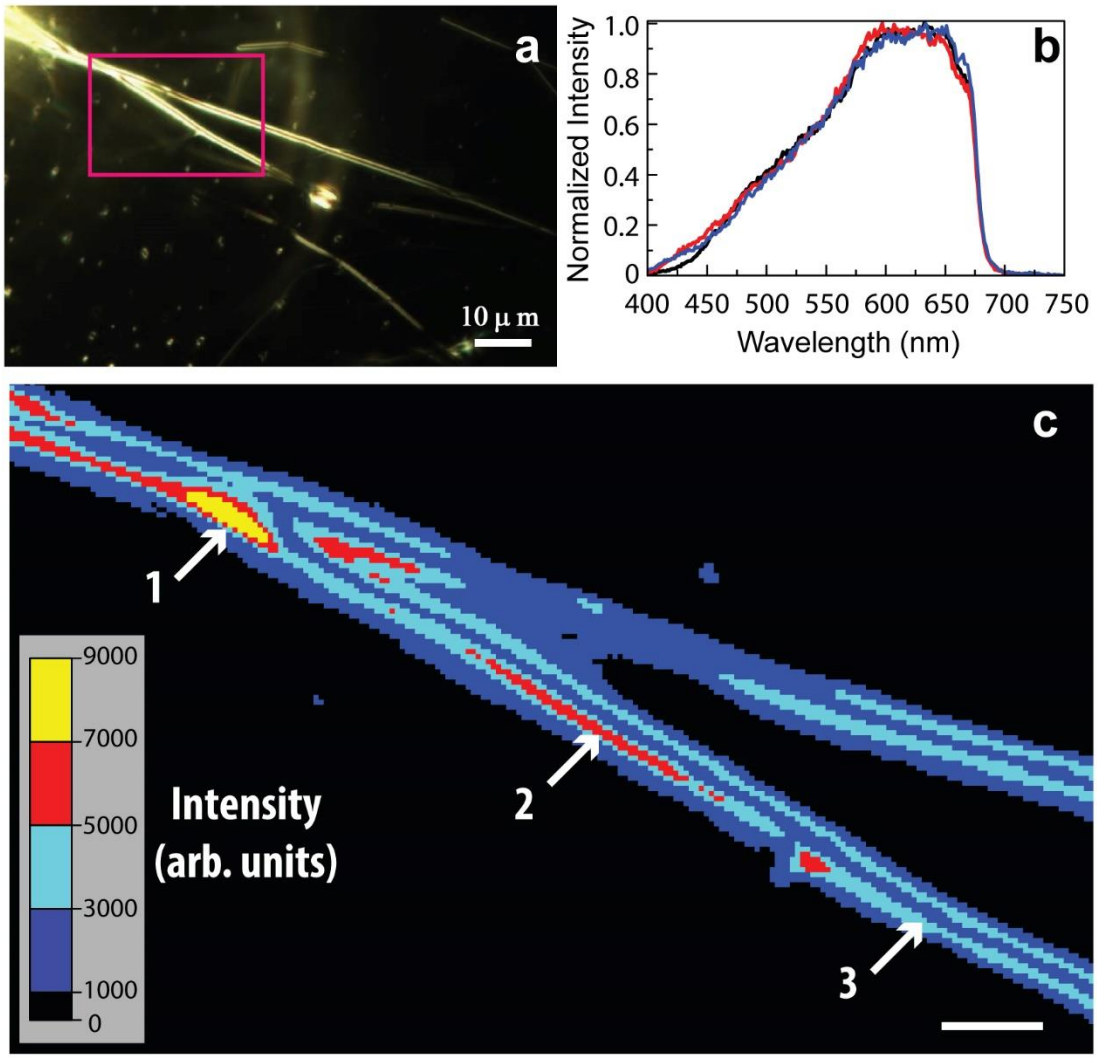

Figure 5. (a) Optical and (c) hyperspectral microscopy images of pNa fibres in transmission dark-field mode (b) Hyperspectral spectrum measured within the single pixel areas (1-3 in c).

Raman spectroscopy was used to better understand the nature of the *p*Na embedded within the polymeric fibres. Several peaks in the Raman spectrum have nearly the same frequencies in a thin sample of bulk crystalline *p*Na and the nanofibres, both acquired at room temperature. The most prominent of these peaks are listed in table 3.

In figure 6 the Raman bands in bulk crystalline *p*Na (solid line), and *p*Na-PMMA nanofibres (dashed line) are shown for the spectral region between 600-1700 cm^{-1}. Three intense lines at 1282 cm^{-1}, 1314 cm^{-1} and 1338 cm^{-1} characterize the Raman spectrum of bulk *p*Na crystals [32,33]. The most striking feature in figure 6 is the inexistence in the *p*Na-PMMA nanofibre Raman spectra of the band centered at 1282 cm^{-1},

which is the most intense peak in bulk crystalline *p*Na. Harrand [32] has identified this peak as resulting from a superposition of the benezene ring symmetric stretching mode, ω_3 , with a combination line arising from another ring stretching mode and a torsion of the amino group, $\omega_5 + \tau_{NH_2}$. The hydrogen bonding between the nitro and amine groups of neighboring molecules induces π−electron charge concentration in the C-N bonds as well as between the bonds connecting unsubstituted carbons in the benzene ring. This produces a quinodal-like structure that leads to an enhanced Raman response. In contrast, 1282 cm^{-1} peak is absent for pNa in solution where the lack of hydrogen bonding results in a more aromatic π-electron charge distribution. The absence of this prominent peak in the *p*Na-nanofibres suggests that the normal hydrogen bonds between the nitro and amine groups are somehow weakened by the electro-spinning production technique. Alternatively, it might be evidence that the majority of *p*Na molecules within the fibre are not incorporated into nanocrystals, but are rather embedded in a less organized structures. Nonetheless, the x-ray diffraction spectra does indicate that a significant fraction of *p*Na molecules do crystallize with their 202 planes oriented within the fibre mat.

Table 3. Raman frequency of the coincident peaks in bulk *p*Na and the electro-spun nanofibres together with the identification of the corresponding vibrational mode[1].

Raman Shift (cm^{-1})	**Relative Intensity (Nano**fibres**)**	**Relative Intensity (Thin Crystal)**	**Vibrational modes[a]**
860	0.34	0.24	$\delta(NO_2)$
1109	0.34	0.12	$\nu(C\text{-}NO_2)$
1137	0.12	0.08	φ(13)
1178	0.12	0.07	φ(9a)
1397	0.07	0.08	φ(19b)
1452	0.09	0.06	φ(19a)
1507	0.11	0.06	$\nu_{as}(NO_2)$
1598	0.20	0.08	φ(8a)

[a] ν=stretching, δ =in-plane deformation, γ=out-of-plane deformation, φ=vibrations of benzene; nomenclature according to G. Varsanyi [30] .

The doublet 1313/1332 cm^{-1} band, that is characteristic of *p*Na in solution and assigned predominately to symmetric NO_2 stretch, is unexpectedly the strongest band in *p*Na nanofibre Raman spectra. For *p*Na in solution, the relative intensities of the doublet varies with the solvent polarity. Interestingly, the observed ratio in the *p*Na nanofibres is similar to that of *p*Na in acetonitrile (a highly polar solvent), indicating that *p*NA molecules inside the PMMA matrix find themselves in a polar environment. This might indicate the presence of a residual electric field from the electro-spinning process that was frozen into the nanofibres as they solidified during the

flight from the needle to the collecting drum. There is also a noticeable enhancement in intensity of the of *p*Na nanofibre Raman peaks at 860 cm^{-1} which corresponds to NO_2 in plane deformation ("scissors"); at 1109 cm^{-1} corresponding to a phenyl-NO_2 stretch; and at 1598 cm^{-1} belonging to a phenyl ring stretching mode.

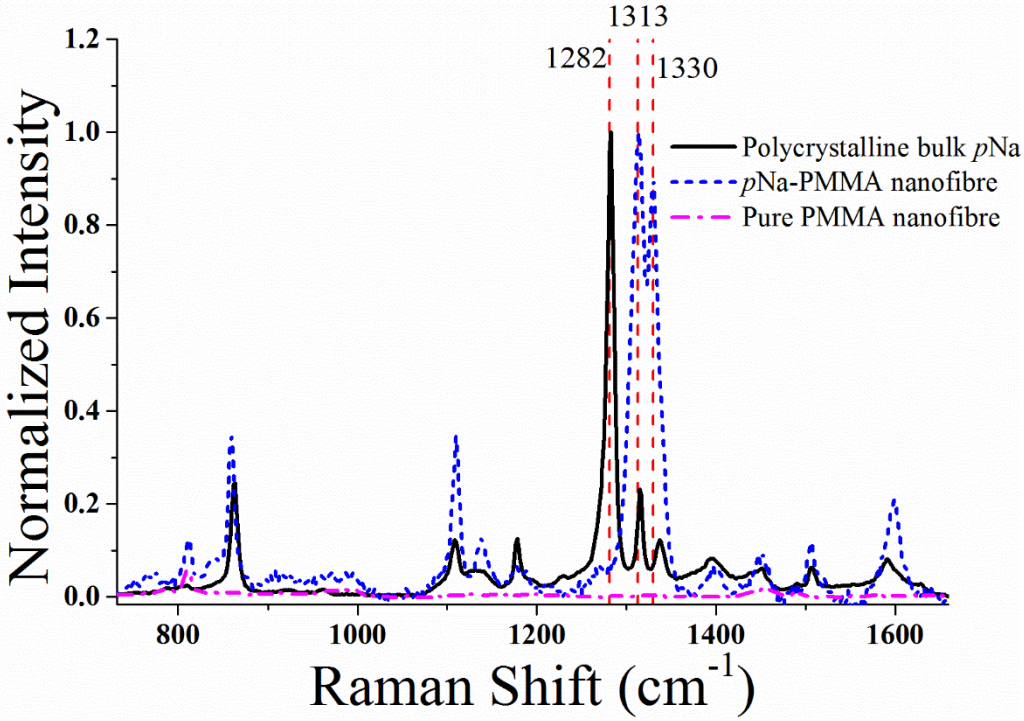

Figure 6. Raman spectra of a bulk sample of polycrystalline *p*Na, a *p*Na-PMMA nanofibre and a pure PMMA nanofibre (without *p*Na) between 600 cm^{-1} and 1700 cm^{-1}. The two spectra containing pNa were normalized to have the same maximum peak height, while the PMMA nanofibre spectrum is reported using the same scale as the *p*Na-PMMA nanofibre spectrum.

The Raman spectra of un-doped PMMA nanofibres is strongly polarized as shown in figure 7. The polymer chains are found to preferentially align along the nanofibre direction. The peak at 810 cm^{-1} corresponds to the stretching mode of the ν(C-O-C) bond; its intensity decreases for crossed polarization, indicating an alignment of the PMMA scaffold and consequently an anisotropic environment for the embedded *p*NA molecules. This may explain why the doublet intensity ratio observed for *p*Na-PMMA nanofibres is similar to that of *p*Na in a polar solvent.

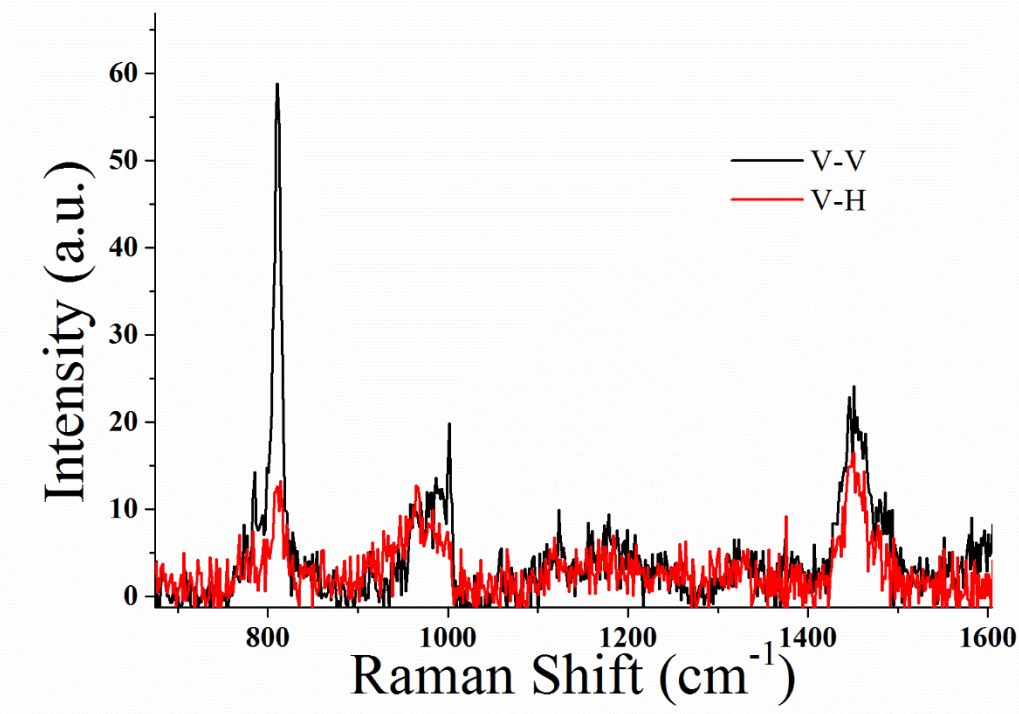

Figure 7. Raman spectra of PMMA nanofibres obtained with polarization configuration V-V and V-H.

3.2 Second harmonic polarimetry

The polarization properties of the second harmonic light was studied to assess the degree of orientational order of the *p*Na molecules embedded within the nanofibres, using the experimental set-up of figure 1. Whereas the polarization of the incident field varies continuously, the SHG field is collected in the so-called q-p and q-s configurations, i.e. with the analyser parallel and perpendicular to the longitudinal axis of the fibre respectively. A strong signal SHG resulted when the polarization of the incident fundamental light and the analyser were both aligned parallel to the selected fibre.

The SHG response of the *p*Na-PMMA nanofibres shows a quadratic dependence as a function of the incident power (figure 8) as expected for a second order nonlinear effect. The r-squared coefficient for the quadratic fit is 0.998.

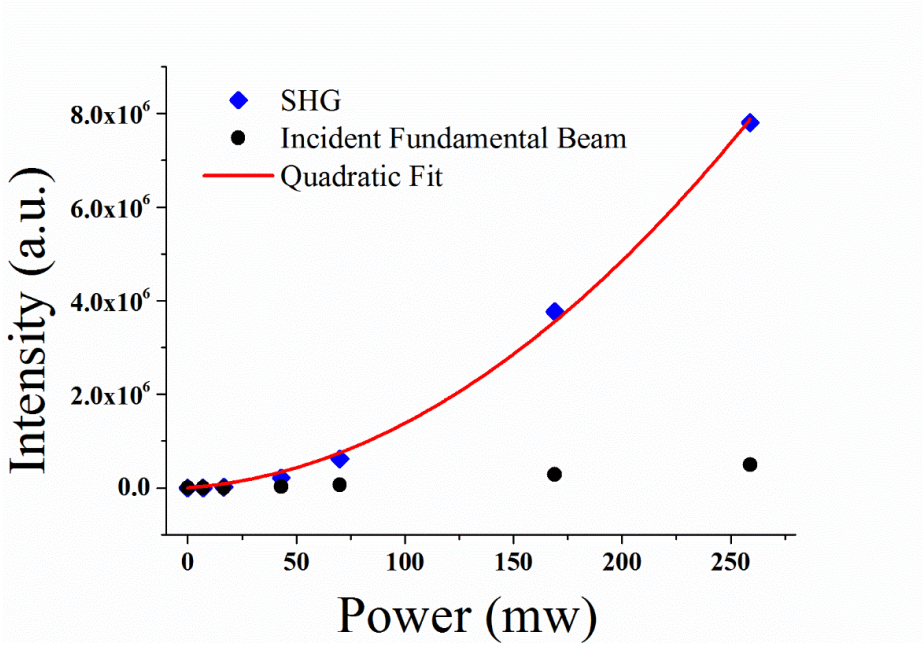

Figure 8. The SHG response of the *p*Na-PMMA nanofibres using a deposition rate of 0.05 mL/h as a function of the average incident power of the fundamental beam (repetition rate of 76 MHz).

The polarimetry curves display a polarization dependence that is characteristic of a SHG response dominated by a single diagonal second-order susceptibility tensor element, figure 9.

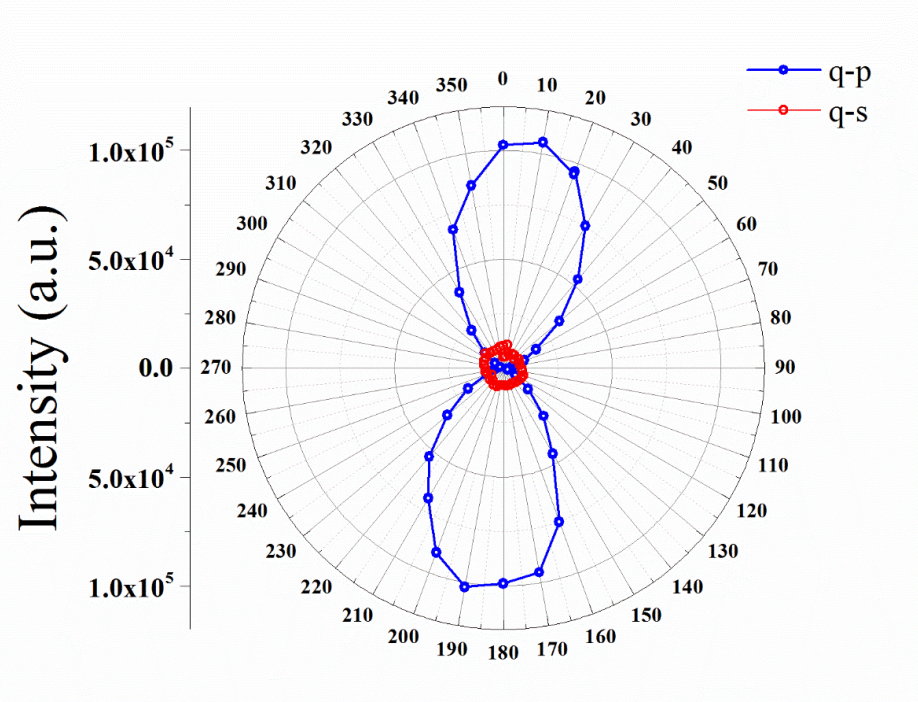

Figure 9. Polar plot of the SHG polarimetry data of *p*Na-PMMA nanofibres produced using a deposition rate of 0.05 mL/h.

When the polarization direction of the incident field is continuously varied, the intensity of the SHG field decreases and reaches a minimum at 90°. This minimum can be a function of the orientation, micro-strain and/or size homogeneity of the nanocrystals inside the nanofibres [34]. The very good alignment of the nanocrystals leads to a nearly vanishing SHG field at cross polarization. The maximum intensity of the SHG radiation for the different deposition rates represented in Figure 10 was normalized to the same value in order to explore the variation with the deposition rate of the minimum intensity (at crossed polarization) of the SHG (inset). The lowest cross-polarization intensity corresponds to the 0.05 mL/h deposition rate, consistent with the X-Ray diffraction data. This is the deposition rate that leads to a narrower diffraction peak indicating larger crystals or less micro-strain and consequently a slightly better degree of preferential alignment of the pNa crystals.

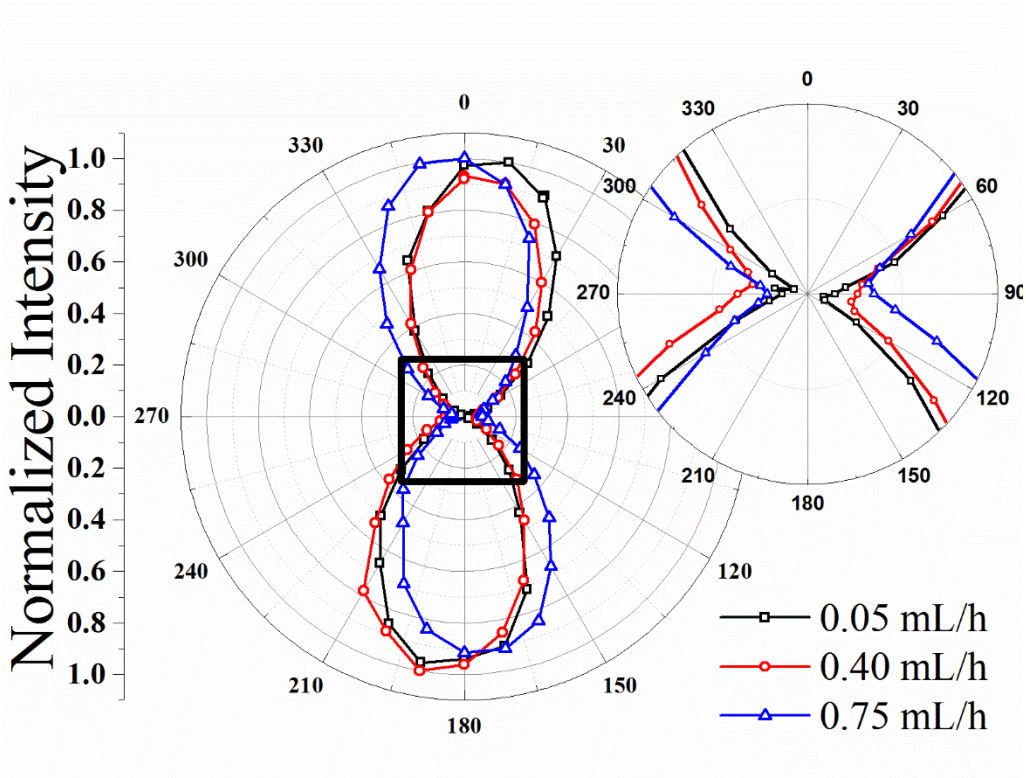

Figure 10. Polar plots of the normalized q-p SHG polarimetry data of PMMA nanofibres doped with *p*Na for the 3 different deposition rates. The close resemblance to a cosine squared polarization dependence is indicative of well-oriented SH generators. (Inset) Variation of the minimum of SHG field near the position of crossed polarizer and analyser.

In figure 11 the second harmonic response of a pNa embedded PMMA nanofiber mat taken at two different times separated by interval of one year is shown. Roughly 80% of the original response has been maintained.

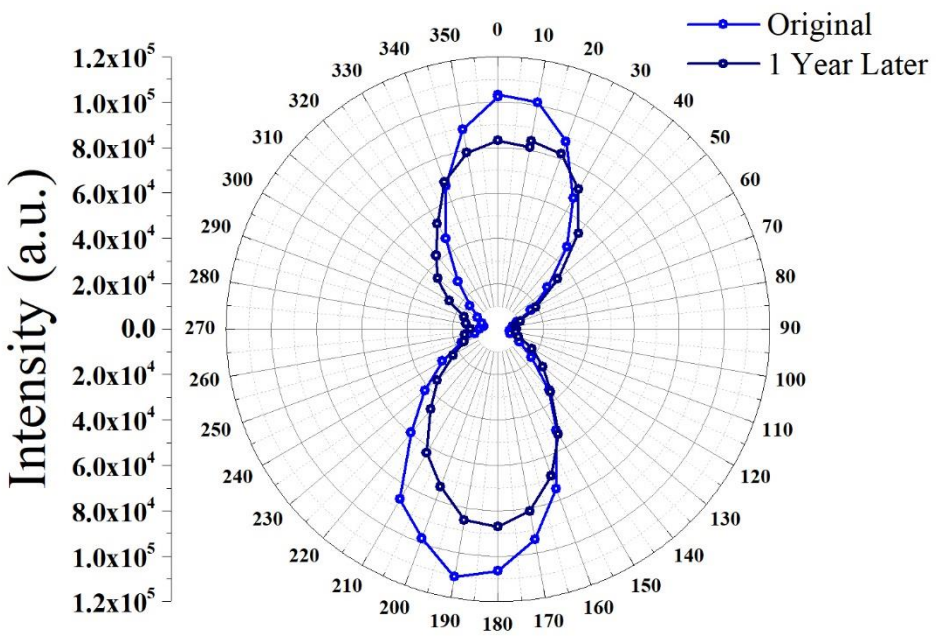

Figure 11. Polar plots of the integrated SHG polarimetry data of PMMA nanofibres doped with *p*Na produced at a deposition rate of 0.05mL/h. The two polarimetry curves were taken at an interval of one year.

3.3 *Effective nonlinear optical coefficient*

In this section, we explore two potential explanations for observed second harmonic signal from the *p*Na nanofibres. One possibility is that the signal is due to the surface polarization of the *p*Na nanocrystals embedded within the nanofibres. We focus our attention on the nanofibres deposited at speed of 0.05 mL/h, which have the strongest observed SHG response. The SHG signal generated by a 4 mm thick potassium dihydrogen phosphate (KDP) crystal under the same excitation and detection conditions is used to calibrate the overall detection efficiency of our system.

The incident fundamental light consisted of pulses with and energy of approximately 0.2 nJ, a FWHM duration of 100 fs and a $1/e^2$ diameter of 0.8 mm. A 50 mm focal length plano-convex lens focused the fundamental beam onto the fibre or KDP crystal. We estimate that the diameter of the focused fundamental beam is roughly 65 μm within the nanofibre or crystal with a corresponding confocal length, $b = k_1 D^2 / 4 \approx 1.2\,cm$. Here k_1 is the magnitude of the wave vector for the fundamental beam in the medium, while D is the 1/e2 diameter at the focus. The expression for the SHG light intensity from a bulk

crystal can be obtained from the solution of the nonlinear wave equation. When the confocal length of the incident fundamental beam is much greater than the crystal thickness the second harmonic power, $\mathcal{P}_{2\omega}^{KDP}$, generated by the crystal is well described by solution obtained using the plane wave approximation [35,36]:

$$\mathcal{P}_{2\omega}^{KDP} = \frac{2\omega^2}{\varepsilon_0 n_1^2 n_2 c^3}\left[d_{eff}\right]^2 \frac{L^2}{\mathcal{A}}\operatorname{sinc}^2\left(\frac{\Delta kL}{2}\right)\mathcal{P}_{\omega}^2 \tag{2}$$

Here $\Delta k = 2k_1 - k_2$ is the wave vector mismatch between the fundamental beam (k_1) and the second harmonic beam (k_2) within the medium, $\mathcal{A}$ is area of the focused beam waist and d_{eff} is the effective nonlinear coefficient. For type I phase matching in KDP at the fundamental wavelength of 800nm, the appropriate second order coefficient is $d_{eff} = \sin(\theta_{pm})d_{36}$, where the phase matching angle is $\theta_{pm} = 44.9^{o}$ and $d_{36} = 0.39\ pm\cdot \mathrm{V}^{-1}$ [36].

The birefringence of the KDP crystal, imparts a spatial walk-off angle between the wave-vector propagation and the direction of energy flow of the second harmonic beam that propagates as an extraordinary ray. In KDP at the phase matching orientation for 800nm incident light, this walk-off angle is 29.5 mrads [37]. Furthermore, the dispersion of KDP creates a group velocity mismatch of approximately 80 fs/mm [37] between the fundamental and second harmonic beams leading to a further temporal walk-off effect. Wang and Weiner [38] have developed a theoretical expression for the reduction in SHG efficiency in the presence of simultaneous spatial and temporal walk-off while taking into account the diffraction effects associated with Gaussian beam propagation. Using their expression we estimate that under our conditions these combined effects will reduce the SHG efficiency by roughly a factor of 3 from that predicted by the continuous plane-wave approximation implicit in equation (2) .

We couple the second harmonic light generated by the crystal or the nanofibre to the 0.3 m imaging spectrograph (Andor Shamrock SR-303i) via a multimode optical fibre bundle by employing a 100× infinity corrected long working length microscope objective from Mitutoyo (Plan Apo). This objective has a numerical aperture of 0.7 and an effective focal length of 2 *mm* both large enough to fully collect the second harmonic light generated by the crystal.

On other hand, following the calculations of Brevet [39] the SHG power arising from a single surface of a *p*Na crystal is given by,

$$\mathcal{P}_{2\omega}^{pNa} = \frac{\omega^2}{2\varepsilon_0 n_1^2 n_2 c^3}\left[\chi^{(2s)}\right]^2 \frac{1}{\mathcal{A}}\mathcal{P}_{\omega}^2 \tag{3}$$

Here $\chi^{(2s)}$ is the quadratic response of *p*Na nanocrystal's surface polarization and we have ignored small correction factors related to the Fresnel reflection and transmission coefficients. The ratio of second

harmonic signals experimentally measured using our set-up for KDP and the *p*Na nanofibres is roughly $P_{2\omega}^{KDP} \approx 150 P_{2\omega}^{pNa}$. Comparing equations (2) and (3) and ignoring the possibly different refractive index contributions, while including the factor of 3 reduction due to the spatial and temporal walk-off in the KDP crystal, we can estimate the effective surface quadratic response under the assumption that the observed *p*Na nanofibre SHG signal is due to a single pNa nanocrystal via the expression,

$$\chi^{(2s)} = d_{eff}^{KDP} L \sqrt{\frac{\mathcal{P}_{2\omega}^{pNa}}{3\,\mathcal{P}_{2\omega}^{KDP}}} \approx 5.2x10^{-17}\, m^2 / V \quad . \tag{4}$$

Here we have taken into account that a single crystal has two surfaces that will contribute coherently to the second harmonic electric field, leading to a multiplicative factor of four in right hand side of equation (3). Malagoli and Munn [19] predict that the dominant quadratic surface susceptibility tensor element for a *p*Na surface oriented along the (202) direction is $\chi_{yyy}^{(2s)} = 1.93x10^{-22}\, m^2 / V$, more than five orders of magnitude lower than the above estimate. This would seem to rule out surface SHG alone as a possible explanation for the observed SHG signal.

A possible alternative mechanism is that the strong electric fields applied during the electrospinning process manage to align a significant number of individual *p*Na molecules during the ejection process and this orientation is frozen into the nanofibres during the rapid solidification that occurs as the fibres travel from the needle to the collection drum. This possibility is consistent with the Raman spectra that indicate the majority of *p*Na molecules present spectra consistent with that of molecules with find themselves in a liquid state dispersed within a polar environment. In many ways this process might be viewed as an accelerated form of electric field poling. This would then allow one to make use of the high molecular polarizability of individual *p*Na molecules.

Assuming, for the sake of argument, that all the embedded *p*Na molecules were appropriately aligned by the applied electric field, the order of magnitude of the resultant second order susceptibility can be easily estimated through the relation,

$$\varepsilon_0 \chi_{pNa,eff}^{(2)}\left(-2\omega;\omega,\omega\right) = f\left(2\omega\right) f^2\left(\omega\right) N \left\langle \beta\left(-2\omega;\omega,\omega\right)\right\rangle \tag{5}$$

Here N is the number density of *p*Na molecules, while $\langle\beta\rangle$ is the average value of first molecular hyperpolarizability. The quantities $f\left(2\omega\right)$ and $f\left(\omega\right)$ represent the local field factors due to the presence of the surrounding PMMA matrix. Within the Lorentz approximation these factors can be estimated according to the relation

$$f\left(\omega\right) = \left(\varepsilon_\omega + 2\right)/3 \tag{6}$$

Together they result in an overall increase by a factor of 1.24 as estimated using the tabulated refractive indices of PMMA at the fundamental (1.484) and second harmonic (1.502) wavelengths. In this case the second harmonic generation mimics that of a crystalline material with the effective nonlinear coefficient d_{eff} in equation (2) replaced by $f(2\omega) f^2(\omega) N \langle \beta \rangle / \varepsilon_0$. Assuming that the density of *p*Na molecules in the nanofibres is approximately that of *p*Na in the crystalline phase (6.3×10^{27} m^{-3}) and disregarding the possible differences in the refractive indices, we can estimate the value of the mean molecular hyperpolarizability that would be required to generate the magnitude of SHG signals we observe,

$$\left\langle \beta_{eff}^{pNa} \right\rangle = \frac{\varepsilon_0}{f(2\omega) f^2(\omega) N_{pNa}} \left(\frac{L_{KDP}}{t_{pNa}} \right) \sqrt{\frac{\mathcal{P}_{2\omega}^{pNa}}{3\mathcal{P}_{2\omega}^{KDP}}} d_{eff}^{KDP} \tag{4}$$

Where t is the thickness of a typical *p*Na nanofibre, roughly 800 nm and we have taken into account the reduction in SHG efficiency of the KDP crystal by a factor of 3 due to spatial and temporal beam walk-off. Substituting the appropriate values into the above equation, we find that $\left\langle \beta_{eff}^{pNa} \right\rangle \approx 7x10^{-50} Cm^3 / V^2$. Huyskens et al. [40] have measured the average first hyperpolarizability of *p*Na in a variety of solvents. From their extensive list, the solvent that is chemically most similar to PMMA is methyl acetate, for which they measure a value of $9.5x10^{-50} Cm^3 / V^2$ at an incident wavelength of 1064nm when corrected for the most recent value based on second harmonic generation in quartz [41]. This agrees with the above order of magnitude estimate, suggesting that a large fraction of the second order optical response of the individual *p*Na molecules was translated into a macroscopic response of the doped electro-spun polymeric fibres. The equivalent effective second order susceptibility can be estimated as $\chi_{eff}^{(2)} \approx 65\ pm/V$, roughly the same magnitude as was reported by Miyazaki et al.[42] for guest-host mixtures of *p*Na and poly(ε-caprolactone). However, our electro-spinning method has the added advantage of producing fibres with a well-defined alignment and good optical quality leading to a coherent and strongly polarized response.

4. Conclusions

In this study, we have shown it is possible to obtain a strong macroscopic second harmonic response from *p*Na molecules embedded in PMMA electro-spun fibres with sub-micron diameters. Low deposition rates favour stronger SHG responses. The size of the effect indicates that it is not simply a result of symmetry breaking at the *p*Na-polymer surfaces, but rather suggest that a non-centrosymmetric arrangement has been induced, possibly as the result of strong hydrogen bonds between the pNa molecules and the polymeric host. We speculate that the high electric fields experienced during extrusion in the electro-spinning process, coupled to the unusually large ground state pNa electric dipole moment of nearly 7 Debye may lead to highly aligned molecular structures that are subsequently frozen into the 1D nanostructure by the rapid

solidification that occurs. This would in essence, amount to a highly accelerated version of electric field poling commonly done to align organic molecules with strong nonlinear responses in polymer substrates. However contrary to normal electric field poling, the electro-spun fibres retain their ability to generate significant second harmonic light over timescales extending to one year.

The electro-spinning should be extendable to other organic molecules with large dipole moments and strong second order nonlinear optical responses. Given the large number of NLO active organic compounds that crystallize in centrosymmetric structures; this technique has the potential to open up a new pathway to fabricate sub-wavelength photonic materials with large second order nonlinear optical responses.

5. Acknowledgements

Hugo Gonçalves thanks the Portuguese Foundation for Science and Technology (FCT) for the support under grant PD/BD/111873/2015. The equipment used to characterize the second harmonic response of the electro-spun fibres was acquired within the framework of the Portuguese National Program for Scientific Re-equipment, contract REEQ-25/FIS/2005 with funds from POCI 2010 (FEDER) and FCT. The Raman microscope was acquired through the project nSTeP Nanostructured Systems for Tailored Performance, NORTE-07-0124-FEDER-000039, ON.2. This work was in part developed in the scope of the projects CICECO − Aveiro Institute of Materials (UID/CTM/50011/2013), financed by national funds through the Fundação para a Ciência e a Tecnologia/Ministério da Educação e Ciência (FCT/MEC) and co-financed by FEDER under the PT2020 Partnership Agreement. The authors are grateful to A. M. P. Botas (University of Aveiro) for help in acquiring the hyperspectral microscopy data.

References

[1] Garmire E 2013 Nonlinear optics in daily life *Opt. Express* **21** 30532–44

[2] Rosenne S, Grinvald E, Shirman E, Neeman L, Dutta S, Bar-Elli O, Ben-Zvi R, Oksenberg E, Milko P, Kalchenko V, Weissman H, Oron D and Rybtchinski B, 2015 Self-assembled organic nanocrystals with strong nonlinear optical response *Nano Lett.* **15** 7232–37

[3] Xu J, Semin S, Niedzialek D, Kouwer PHJ, Fron E, Coutino E, Savoini M, Li Y, Hofkens J, Uji-I H, Beljonne D, Rasing T and Rowan AE 2013 Self-assembled organic microfibers for nonlinear optics *Adv. Mater.* **25** 2084–9

[4] Ray PC and Leszczynski 2006 J Nonlinear optical properties of highly conjugated push-pull porphyrin Aggregates: role of intermolecular interaction *Chem. Phys. Lett.* **419** 578–83

[5] Jeon S, Malyarchuk V, Rogers JA and Wiederrecht, GP Fabricating three-dimensional nanostructures using two photon lithography in a single exposure step *Opt. Express **14*** 2300–08

[6] Koh AL, Fernández-Domínguez AI, McComb DW, Maier SA and Yang JKW 2011 High-resolution mapping of electron-beam-excited plasmon modes in lithographically defined gold nanostructures *Nano Lett.* **11** 1323–30

[7] Shambat G, Ellis B, Petykiewicz J, Mayer M; Majumdar A, Sarmiento T, Harris J, Haller EE, and Vuckovic J 2012 Electrically driven photonic crystal nanocavity devices *IEEE J. Sel. Top. Quantum Electron.* **18** 1700–10

[8] Isakov DV., de Matos Gomes E, Vieira LG, Dekola T, Belsley MS and Almeida BG 2011 Oriented single-crystal-like molecular arrangement of optically nonlinear 2-methyl-4-nitroaniline in electrospun nanofibers *ACS Nan*o ***5*** 73–8

[9] Bhardwaj N and Kundu SC 2010 Electrospinning: a fascinating fiber fabrication technique *Biotechnol. Adv.* **28** 325–47

[10] Isakov DV, Belsley MS, de Matos Gomes E, Gonçalves H, Schellenberg P and Almeida B G 2014 Intense optical second harmonic generation from centrosymmetric nanocrystalline para-nitroaniline *Appl. Phys. Lett.* **104** 181903

[11] Isakov D, de Matos Gomes E, Belsley MS, Almeida B and Cerca N 2012 Strong enhancement of second harmonic generation in 2-methyl-4-nitroaniline nanofibers *Nanoscale* **4** 4978

[12] Chronakis IS 2005 Novel nanocomposites and nanoceramics based on polymer nanofibers using electrospinning process - a review *J. Mater. Process. Technol.* **167** 283–93

(13) Li J, Li H, Hu H, Zhao Y and Wang Q 2015 Preparation and application of polymer nano-fiber doped with nano-particles *Opt. Mater.* **40** 49–56

[14] Ren ML, Liu W, Aspetti CO, Sun L and Agarwal R 2014Enhanced second-harmonic Generation from metal-integrated semiconductor nanowires via highly confined whispering gallery modes *Nat. Commun.* **5** 5432

[15] Kravets VG, Marshall OP, Nair, RR, Thackray B, Zhukov A, Leng J and Grigorenko AN 2015 Engineering optical properties of a graphene oxide metamaterial assembled in microfluidic channels *Opt. Express* **23** 1265

[16] Verbiest T, Houbrechts S, Kauranen M, Clays K and Persoons A 1997 Second-order nonlinear optical materials: recent advances in chromophore design *J. Mater. Chem.* **7** 2175–89

[17] Shkir M, Riscob B, Hasmuddin M, Singh P, Ganesh V, Wahab MA, Dieguez E and Bhagavannarayana G 2014 Optical spectroscopy, crystalline perfection, etching and mechanical studies on p-nitroaniline (pNA) single crystals *Opt. Mater. (Amst).* **36** 675–81

[18] Kobayashi H and Kotani M 1994 Study of single crystal surface with second-harmonic generation : p -nitroaniline *Mol. Cryst. Liq. Cryst. Sci. Technol. Sect. A. Mol. Cryst. Liq. Cryst.* **252** 277–81

[19] Malagoli M and Munn, RW 2000 Microscopic calculation of surface-induced second-harmonic generation in crystals of para-nitroaniline *J. Chem. Phy*s. **112** 6757–62

[20] Marchewka MK, Ratajczak H and Debrus S 2003 Infrared spectrum and nonlinear optical properties of p-nitroaniline-l-tartaric acid (2:1) molecular complex *J. Nonlinear Opt. Phys. Mater.* **12** 113–21

(21) Kosenkov D and Slipchenko LV. 2011 Solvent effects on the electronic transitions of p-nitroaniline: a QM/EFP study *J. Phys. Chem. A* **115** 392–401

[22] Kuzyk M G, Pérez-Moreno J and Shafei S 2013 Sum rules and scaling in nonlinear optics *Physics Reports*. **529** 297–398

[23] Kato M, Kiguchi M, Sugita N and Taniguchi Y 1997 Second-order nonlinearity of mixtures Including p-nitroaniline derivatives *J. Phys. Chem. B*, **101** 8856–59

[24] Cambré S, Campo J, Beirnaert C, Verlackt C, Cool P and Wenseleers W 2015 Asymmetric dyes align inside carbon nanotubes to yield a large nonlinear optical response *Nat. Nanotechnol.* **10** 248–52

[25] Zhang CL and Yu SH 2014 Nanoparticles meet electrospinning: recent advances and future prospects *Chem. Soc. Rev.* **43** 4423–48

[26] Garreau A and Duvail JL 2014 Recent advances in optically active polymer-based nanowires and nanotubes *Adv. Opt. Mater.* **2** 1122–40

[27] Bernardo C, Belsley M, de Matos Gomes E, Gonçalves H, Isakov D, Liebold F, Pereira E, Pires V, Samantilleke A, Vasilevskiy M and Schellenberg P 2014 A versatile fluorescence lifetime imaging system for scanning large areas with high time and spatial resolution *Second International Conference on Applications of Photonics and Optics*, *Proc. SPIE* vol 9286 (Aveiro, Portugal, 26-30 May 2014) eds. Martins Costa MFPC and Nogueira, RN (Bellingham SPIE) pp 928637–8

[28] Piperno S, Lozzi L, Rastelli R, Passacantando M and Santucci S 2006 PMMA nanofibers production by electrospinning *Appl. Surf. Sci.* **252** 5583–6

[29] Zak AK, Majid, WHA, Abrishami ME and Yousefi R 2011 X-Ray analysis of ZnO nanoparticles by Williamson-Hall and size-strain plot methods *Solid State Sci.* **13** 251–6

[30] Varsányi G 1969 *Vibrational Spectra of Benzene Derivatives*, 1st edition (New York, Academic Press) 1969

[31] Marlow F, Hill W, Caro J and Finger G 1993 Raman-study on p-nitroaniline in channels of the molecular-sieve alpo(4)-5 *J. Raman Spectrosc.* **24** 603–8

[32] Harrand M 1975 Raman study on para nitroaniline single crystal. II: internal vibrations *J. Raman Spectrosc.* **4** 53–73

[33] Harrand M 1979 Raman study on p-nitroaniline: molecular structure in the molten phase *J. Raman Spectrosc.* **8** 161–4

[34] Brasselet S, le Floc'h V, Treussart F, Roch, JF, Zyss J, Botzung-Appert E and Ibanez A 2004 In situ diagnostics of the crystalline nature of single organic nanocrystals by nonlinear microscopy. *Phys. Rev. Lett.* **92** 207401–1

[35] Boyd, RW 2003 *Nonlinear Optics* 3rd. ed. (Rochester Academic Press)

[36] Nikogosyan DN 1991 *Handbook of Nonlinear Optical Crystals*, 3rd Revised ed. (Berlin, Springer Verlag)

[37] SNLO nonlinear optics code available from A. V. Smith, AS-Photonics, Albuquerque, NM

[38] Wang H and Weiner AM 2003 Efficiency of short-pulse type I second harmonic generation with simultaneous spatial walk-off, temporal walk-off and pump depletion *IEEE J. Quantum Electronics* **39** 1600

[39] Brevet PF 1996 Phenomenological three-layer model for surface second-harmonic generation at the interface between two centrosymmetric media *J. Chem. Soc. Faraday Trans.* **92** 4547

[40] Huyskens FL, Huyskens PL and Persoons AP 1998 Solvent dependence of the first hyperpolarizability of p-nitroanilines: differences between nonspecific dipole–dipole interactions and solute–solvent H-bonds *J. Chem. Phys.* **108** 8161

[41] Reis H 2006 Problems in the comparison of theoretical and experimental hyperpolarizabilities revisited *J. Chem. Phys.* **125** 014506

[42] Miyazaki T, Wanntabe T, and Miyata S 1988 Highly efficient second harmonic generation in p-nitroanaline / poly(lactone) systems *Japanese J. of Appl. Phys.* **27** L1724

The influence of nanocrystal size on optical second harmonic generation by *p*ara-nitroanaline embedded in electro-spun polymeric fibres

Hugo Gonçalves[1], Inês Saavedra[1], Marlene Lúcio[1], Sigrid Bernstorff[2], Etelvina de Matos Gomes[1], Michael Belsley[1*]

[1] Centre of Physics, University of Minho, Campus de Gualtar, 4710-057 Braga, Portugal

[2] Elettra – Sincrotrone Trieste S.C.p.A., Strada Statale 14, Basovizza, 34149 Trieste, Italy

Abstract

Poly(methyl methacrylate) electro-spun fibres with embedded nanocrystals of the paradigmatic donor–acceptor nonlinear chromophore *para*-nitroaniline, have been recently demonstrated to be efficient generators of second harmonic light. To understand the influence of the size and local strain experienced by the embedded *para*-nitroaniline nanocrystals, a Williamson−Hall analysis was carried out on the X-ray diffraction intensity. Both the mean crystal size and strain can be tuned by simple changes in the deposition parameters of flow rate and applied voltage. The observed second harmonic signal is well correlated with the ratio of the fibre diameter to the mean *para*-Nitroaniline crystal size suggesting that surface effects are the main source of the strong nonlinear optical response. Adjusting the electro-spinning deposition parameters when producing polymeric fibres doped with strong nonlinear organic chromophores with high dipole moments has the potential to provide a versatile and efficient method for developing second order nonlinear optical materials.

*E-mail: belsley@fisica.uminho.pt Tel: +351 253 604320

ORCID identifiers: Hugo Gonçalves (0000-0002-1357-1764); Marlene Lúcio (0000-0003-2593-1672); Etelvina de Matos Gomes (0000-0002-0862-1683); Michael Belsley (0000-0001-7968-5038)

Keywords: second harmonic generation, electro-spun polymeric fibres, nanocrystal size and strain, Williamson-Hall analysis, breaking of centrosymmetry

Introduction

At the nanoscale, confinement effects can significantly influence the physical, electrical and optical properties of materials. A judicious application of these effects can lead to the strategic development of tailored micro/nanostructures to fabricate novel optoelectronic devices, or to enhance their performance (Boles 2016; Ni 2016; O'Brian 2016). Organic chromophores have attracted attention in the past decades because of their promising applications in electronic and photonic devices (Dvornikov 2009; Li 2017; Ostroverkhova 2016). Arrangements of multiple chromophores in well-defined structures with well-defined orientations or separations can be tuned to provide specific properties of optoelectronic nanocomponents (Duan 2016, Varughese 2014). Even simple variations in the ambient conditions present during the formation of nanocrystals can enable a tuning of their dimensions and optical responses (Ostroverkhova 2016).

The *para*-nitroaniline (*p*Na) ($C_6H_6N_2O_2$) molecule and its derivatives are model push–pull charge transfer organic molecules (Shkir 2014). Due to strong intra-molecular charge transfer from the NH_2 electron-donor group through the phenyl ring to the electron-acceptor NO_2 group, *p*Na is one of the simplest organic molecules that allow optical second harmonic generation (SHG) (Islam 2011). This and other photo and chemical features of *p*Na have long been the subject of various investigations (Shkir 2014; Malagoli 2000; Isakov 2014; Kato 1997; Werner 1992) . However, despite having a large effective hyperpolarizability, *p*Na crystallizes in a centrosymmetric structure where the individual molecular dipoles interfere destructively, cancelling the macroscopic second order nonlinear optical response (Lalama 1979) . *p*Na crystalizes in a monoclinic system with a space group $P2_1/n$ and the respective unit cell parameters are *a=9.0335(8) Å, b=6.9356(5)Å, c=6.8008(6)Å (*Shkir 2014*).* The general tendency of organic push-pull molecules to crystallize in centrosymmetric forms has so far limited the extent to which they have been employed in opto-electronic applications.

Our group has been developing strategies to modulate the organization of *p*Na nanocrystals by embedding them inside a 1D polymeric matrix (Isakov 2014) through the electro-spinning technique. For example, controlling the mean fibre diameter, imposes restrictions the kinetic growth of the organic nanocrystals. Furthermore, since nanocrystals have a high surface to volume ratio they are sensitive to the local environment in which they form. In the case of *p*Na embedded in a 1D polymeric matrix fabricated via electro-spinning via a strong DC electric field, the cleavage plane with

Miller indices (202) predominates as the preferential orientation and is parallel to the nanofibre elongation direction (Isakov 2014). This crystalline plane has been reported to be an efficient surface for optical second harmonic generation (SHG) (Malagoli 2000).

Electro-spinning efficiently incorporates *p*Na molecules into sub-wavelength polymeric fibres. This has been proven to be a simple and versatile technique were a number of processing parameters can be tuned to influence the resultant morphology and diameter of the fibres (Chronakis 2005; Naseri 2016). The viscosity and conductivity of the main solution, the molecular weight of the components, and needle diameter are a few examples of parameters that determine the final fibre morphology. Additionally, the applied voltage, the distance between the needle and collector, the type of collector and the flow rate of the solution, as well as ambient temperature and humidity, play important roles in governing the physical properties of the fabricated fibres.

This work investigates the influence of the flow rate and applied voltage on the mean *p*Na crystal size and strain, employing synchrotron X-ray radiation at the synchrotron ELETTRA, Italy. Analysing the diffraction line width of the Bragg reflections, the size and local strain of the *p*Na nanocrystals inside the poly(methyl methacrylate) (PMMA) fibres are estimated using the Williamson−Hall method (Williamson 1953; Zak 2011). Here focus is on the x-ray diffraction peaks at low Bragg angles since they are the most sensible to the specimen geometry (Pecharsky 2009).

Experimental details

Several sets of PMMA fibres containing *p*Na in a 2:1 ratio by weight, were produced by electro-spinning employing different flow rates and applied voltages. The *p*Na with 99.98% purity was purchased from Sigma Chemical Co. and was dissolved in dimethyl formamide (DMF). PMMA with a molecular weight of 120000 was purchased from Alfa Aesar, and was dissolved in toluene, producing a precursor solution with a concentration of 10 % by weight. The precursor solution for the production of the fibres was stirred under ambient conditions for several hours, before deposition by electro-spinning. The DMF (C_3H_7NO, 99.8%) and toluene ($C_6H_5CH_3$, 99.8%) were purchased from Sigma-Aldrich and used as received.

The precursor solution was loaded into a syringe with a 0.6 mm diameter needle and connected to the anode of a high voltage power supply (Spellmann CZE2000). To produce well-aligned nanofibre arrays, a high voltage was applied between the needle and a grounded drum collector rotating at 100 rpm. The distance between the anode and collector was 12 cm. The fibres sets were produced using flow rates of 0.05 mL/h, 0.40 mL/h and 0.75 mL/h, with a fixed applied DC voltage of 17kV. A dedicated syringe pump controlled the flow rate. Another two sets of fibres were produced, fixing the flow rate at 0.05mL/h, and setting the applied voltage to 14kV and 19kV.

Images of the resulting fibres were acquired using a Scanning Electron Microscopic (SEM) Nova Nano SEM 200, operated at an accelerating voltage of 10 kV. The *p*Na nanocrystallite mean size and local strain were estimated using the synchrotron X-Ray diffraction patterns acquired at the Austrian SAXS/WAXS beamline in Elettra, Italy employing a wavelength of 1.54 Å. To obtain the intensity patterns, undoped PMMA fibres, PMMA/*p*Na fibres or polycrystalline *p*Na powder were loaded into a 1.5 mm diameter, borosilicate capillary. The corresponding X-Ray diffraction patterns were recorded using a Pilatus 100K 2D detector system with a pixel size of 172 μm.

The SHG efficiency of the PMMA/*p*Na fibre sets were measured using a polarimetry setup based on a mode-locked Ti:Sapphire laser (Coherent, Mira) with a 100fs temporal pulse width and a 76 MHz repetition rate. These measurements consisted in illuminating the sample at normal incidence with fundamental light whose linear polarization was rotated about the incident beam axis, and collecting the SHG response through a polarization analyser orientated either along the fibres longitudinal axes (q-p configuration) or perpendicularly to the fibres axes (q-s configuration), see figure 1.

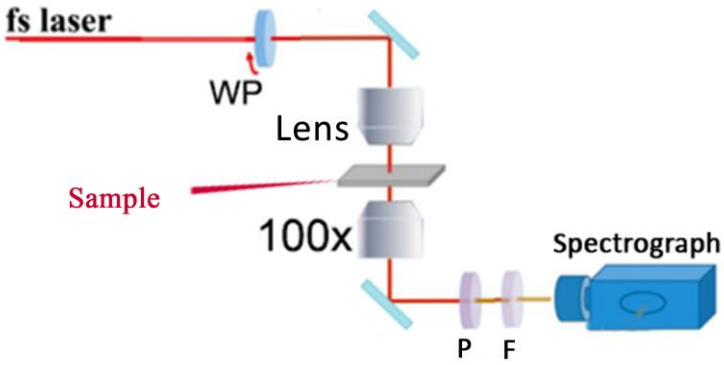

Figure 1 – Polarimetry Setup consisting of a linearly polarized Ti:Sapphire laser beam emitting pulses centred at 800nm with a 100 fs temporal width that is focused onto a single nanofibre by a 5mm focal length lens. The SHG was collected using a 100× microscope objective with a numerical aperture of 0.7. The collected signal is registered by a cooled CCD after passing through a 0.3m Spectrograph with a 0.20 nm spectral resolution. An achromatic half-wave wave plate (WP – λ/2) is used to continuously vary the polarization orientation of the incident field. A fixed polarizer (P) and a set of filters (F) selects the SHG component polarized along or perpendicular to the longitudinal fibre axis

The SHG emission was collected through an infinity corrected long working distance (x100) microscope objective with a numerical aperture of 0.7 (Mitutoyo). A set of filters reduces the incident beam intensity and isolates the SHG signal. The resulting spectra were recorded by focusing the signal beam onto a multi-mode optical fibre coupled to a 0.3m spectrograph (Andor, Shamrock) outfitted with a cooled CCD array (Andor, Newton DU920P-BVF)

Results and Discussion

Figure 2 shows a SEM image of several PMMA/*p*Na fibres. These fibres were deposited using an applied accelerating voltage of 17kV and a flow rate of 0.4mL/h. The fibres have a homogeneous morphology with sub-micron diameters. The mean diameter of the nanofibers tends to decrease as the flow rate is increased, while both higher and lower accelerating voltages result in larger diameter fibres with a large size dispersion. Table 1 summarizes the data characterising these observations. A statistical comparison between the fibre groups was carried out using the parametric method of one-way ANOVA, followed by Tukey post hoc test for multi-group comparison. Only the fibres produced at a voltage of 17 kV and flow rates of 0.05 and 0.4 mL/h can be labelled as statistically distinct at a significance of $p<0.05$.

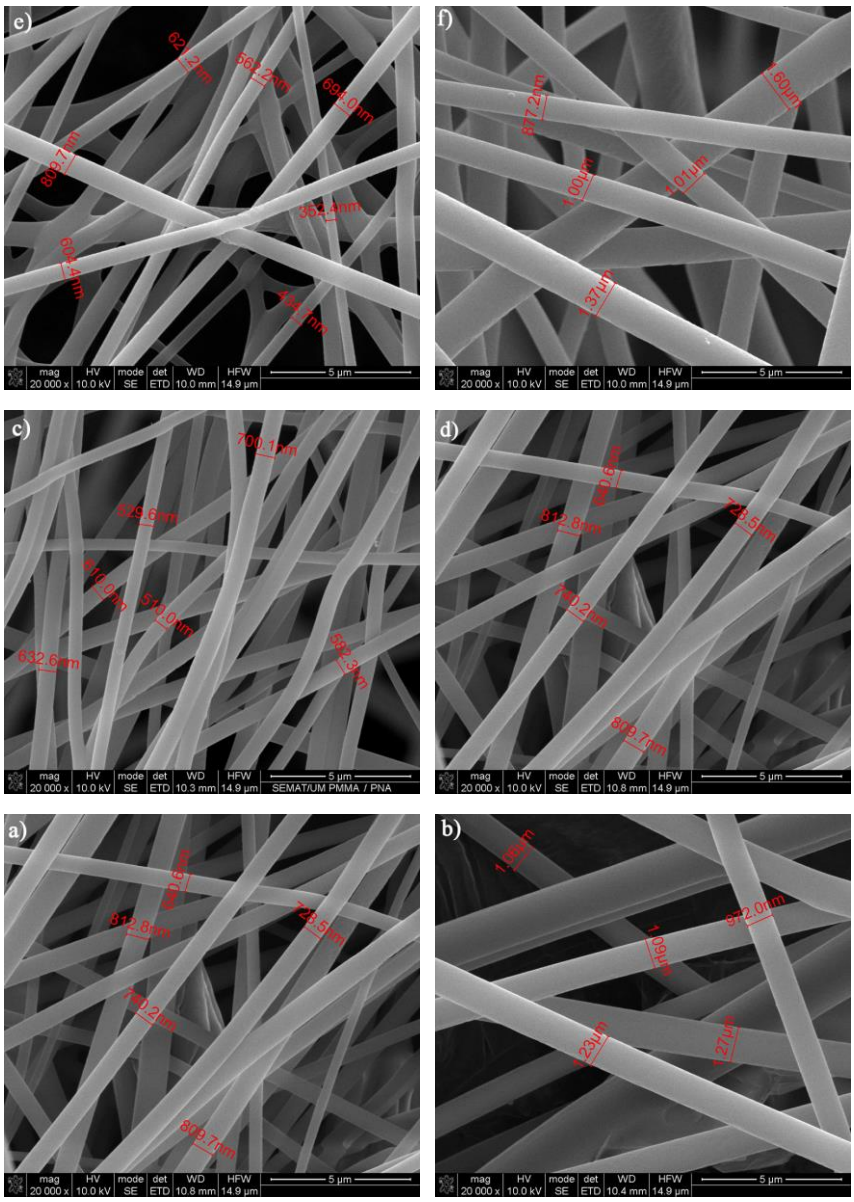

Figure 2 - SEM microscopy images of PMMA/*p*Na fibres produced by electro-spinning. The different images in the left-hand column were obtained for fibres produced with different flow rates, but a constant applied voltage of 17 kV; for those in the right-hand column the flow rate was held fixed at 0.05 mL/h and the applied voltage varies. Specific values of the flow rate and applied DC voltage are: a) 0.05 mL/h and 17 kV; b) 0.05 mL/h and 14 kV; c) 0.40 mL/h and 17 kV; d) 0. 05 mL/h and 17 kV; e) 0.75 mL/h and 17 kV; f) 0.05 mL/h and 19 kV. Several representative fibre diameters are indicated in the images.

Table 1 – Mean PMMA/*p*Na fibre diameters d_{fib} and the corresponding standard deviations quoted as uncertainties as a function of flow rate and the applied voltage.

Applied Voltage of 17kV			**Flow rate of 0.05 mL/h**	
Flow rate (mL/h)	d_{fib} (μm)		Applied Voltage (kV)	d_{fib} (μm)
0.05	0.80 ± 0.1		14	1.42 ± 0.4
0.40	0.55 ± 0.1		17	0.80± 0.1
0.75	0.50 ± 0.1		19	1.01 ± 0.3

The Williamson−Hall method was applied using the observed XRD intensity patterns of the different PMMA/*p*Na fibre sets, in order to evaluate how the flow rate and the applied voltage influence the mean *p*Na crystal size and average induced local strain. The X-ray profile of *p*Na powder at low-angles is shown in figure 3 together with the respective Miller indices of the main peaks. The $2\theta_c$ values for the peaks were obtained by summing the pixel intensities at each diffraction angle and subsequently performing a Pseudo-Voigt fit to each peak (I) according to the expression in equation 1.

$$I = I_0 + A\left[m_u \frac{2}{\pi}\left(\frac{\beta}{4(2\theta - 2\theta_c)^2 + \beta^2} + (1-m_u)\frac{\sqrt{4\ln 2}}{\sqrt{\pi}\beta} e^{-\frac{4\ln 2}{\beta^2}(2\theta - 2\theta_c)^2} \right) \right] \quad \textbf{(1)}$$

Various mathematical functions have been investigated and classified according to their ability to adequately model Bragg reflections (Pecharsky 2009) . The pseudo-Voigt function is obtained from a weighted linear superposition of Lorentz and Gauss functions where the parameter m_u represents the fractional contribution of the Lorentz function. The parameter (A) estimates the amplitude of the diffraction peak above the background, I_0, while the full width at half maximum of the peak is given by the parameter β . The width of a given Bragg peak is typically a convolution of the instrument response with the sample dependent width.

The broadening due to the instrumental response β_{instr} was characterized by collecting the diffraction pattern of a standard sample of *p*-bromo benzoic acid (PBB), yielding $\beta_{instr} < 0.001^{o}$. This is negligible compared to the widths of observed diffraction peaks for the PMMA-*p*Na fibres.

The powder profile of the *p*Na powder shown in figure 3 is dominated by an intense peak ascribed to the (110) Bragg plane. Due to the symmetry-equivalent planes a split is observed in this peak. Figure 3 also displays the diffraction profiles arising from the *p*Na crystals within the electro-spun PMMA fibres. The applied voltage for these cases was held constant at 17kV, while the employed flow rates were 0.05, 0.40 and 0.75 mL/h. All peaks observed for the *p*Na doped fibres were significantly broadened in comparison with the *p*Na powder sample, principally due to the small sizes of the embedded *p*Na crystals. Small deviations in angles are also observed, indicating the presence of uniform local strain. Furthermore, the flow rate value influences the relative intensities of the X-Ray diffraction patterns of the embedded *p*Na nanocrystals.

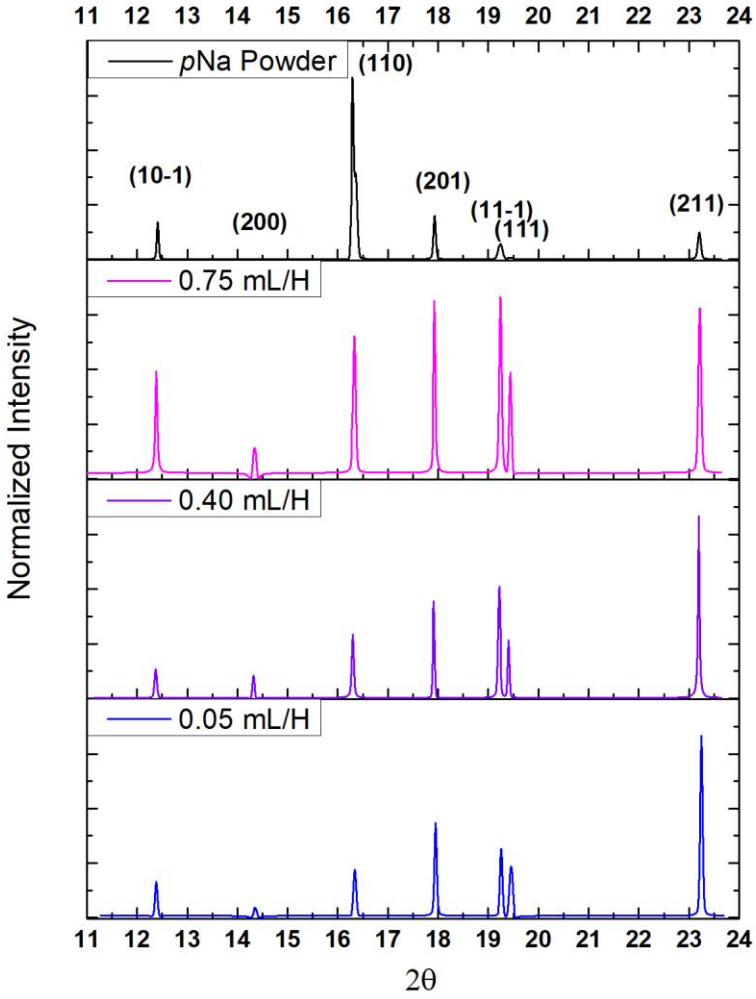

Figure 1- X-Ray diffraction patterns of pNa polycrystalline powder (a) and those of pNa embedded in the PMMA fibres. The profiles shown in (b), (c) and (d) correspond to fibres produced at an applied voltage of 17kV with flow rates of 0.05, 0.40 and 0.75 mL/h respectively. The corresponding Miller indices indicated in (a) are shared by all of the profiles.

The average crystal diameter (D) and the maximum apparent strain (ε) was estimated following the Williamson-Hall (W-H) (Williamson 1953; Zak 2011) method through the equation

$$\beta_{\mathrm{hkl}} \cos(\theta) = \frac{K\lambda}{D} + 4\varepsilon \sin(\theta) \ . \qquad \textbf{(2)}$$

The Williamson-Hall analysis assumes that the broadening due to size effect and inhomogeneous strain are simply additive. Since they have different angular dependences their respective contributions can estimated by plotting the product of $\beta\cos(\theta)$ as a function of $4\sin(\theta)$, and fitting a straight line to the experimental points. The width of each peak, β_{hkl}, in radians, was obtained from the Pseudo-Voigt function fits according to (eq.1). In equation (2) the constant K, known as the Scherrer is a factor that takes into account the crystallite habit and can vary between 0.87 and 1 (Holzwarth 2011). Although the differences between the powder *p*Na XRD pattern and those of the *p*Na-PMMA fibres suggests that the *p*Na nanocrystals do not grow isotropically within the fibres, for all the analyses reported here a value of $K = 0.94$ corresponding to spherical crystals was assumed as is common in the literature (Zak 2011). This amounts to making a simplifying assumption regarding the overall scaling factor for the mean nanocrystal sizes that has an uncertainty of at most 8% given the range of possible Scherrer factors.

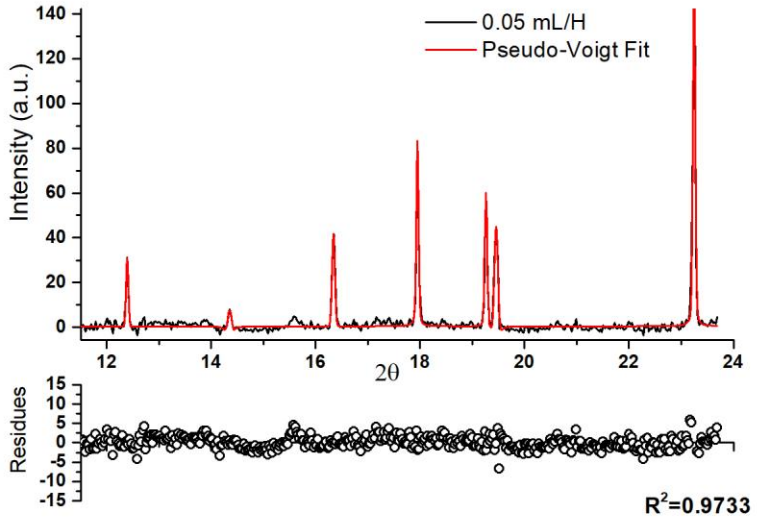

Figure 2 – An example of the Pseudo-Voigt fit to the X-ray profile corresponding to fibres produced with an applied voltage of 17kV at a flow rate of 0.05 mL/h with typical residues shown.

Plots of $\beta\cos(\theta)$ as a function of $4\sin(\theta)$ for the three x-ray profiles of figure 3 are shown in figure 5. The average internal crystalline strain and mean crystallite size are estimated, respectively, from the slope and the intercept of the linear fit to the experimental data corresponding to the seven fit diffraction peaks.

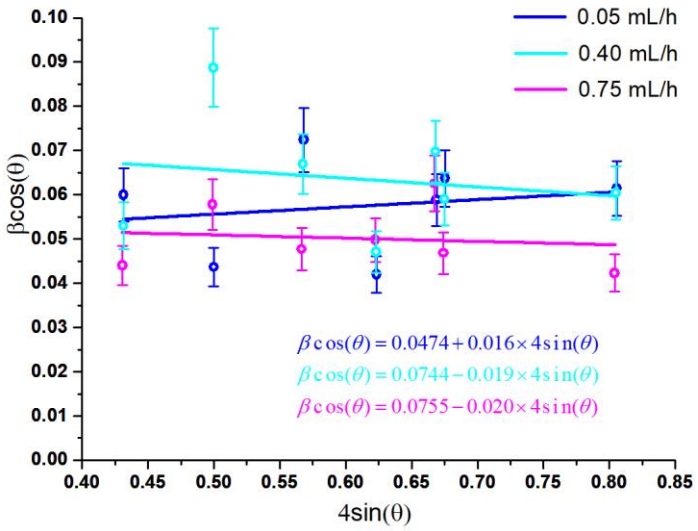

Figure 3 - The W-H plots of the *p*Na embedded in PMMA fibres for the three different flow rates employed in the electro-spinning process. The applied voltage was fixed at 17 kV.

For a flow rate of 0.05mL/h and an applied voltage of 17kV, the mean crystal diameter is estimated to be 30.5 ± 0.2 nm with a strain value of 0.016. As a note of caution one should keep in mind that obtaining values of the local strain from the W-H plots is a practical empirical approach and indicative of general trends, but lacks a firm theoretical basis (Birkholz 2011). The same analysis was applied to the remaining fibre sets at this applied voltage and the resulting values for the deduced crystal sizes and micro-strains are summarized in figure 6.

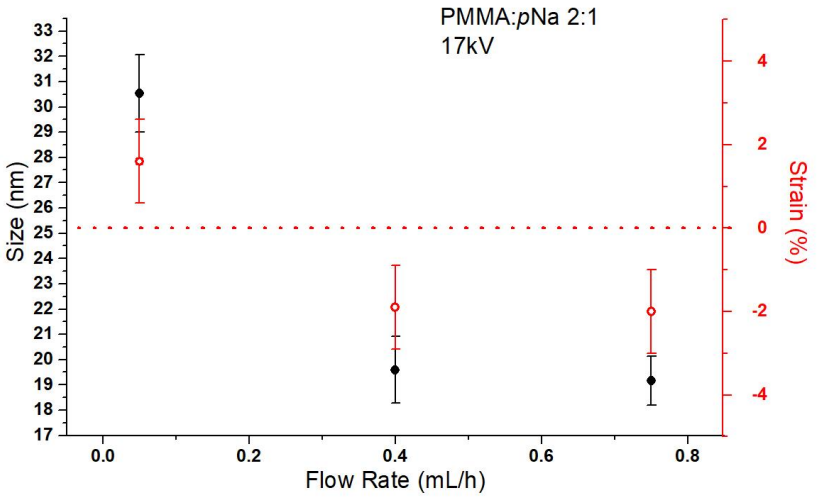

Figure 4 - The results of the W-H analysis of *p*Na embedded in electro-spun PMMA fibres as a function of the flow rate employed.

High flow rates tend to produce smaller crystals with negative local strain. The strain might be an indication of residual stress created by the strong DC electric field used in the deposition. To observe the influence of the applied voltage, the same analysis was performed for sets of fibres produced using 14kV and 19 kV at a flow rate of 0.05mL/H. Figure 7 presents the results of the respective W-H analysis. The highest applied voltage resulted in significantly smaller *p*Na crystals. The SEM images (see results summarized in table 1) show that the mean diameter as well as the width of the diameter distribution (indicated by the standard deviation) for these two fibre sets produced at 14kV and 19kV are larger than the corresponding values for the fibres produced at 17kV.

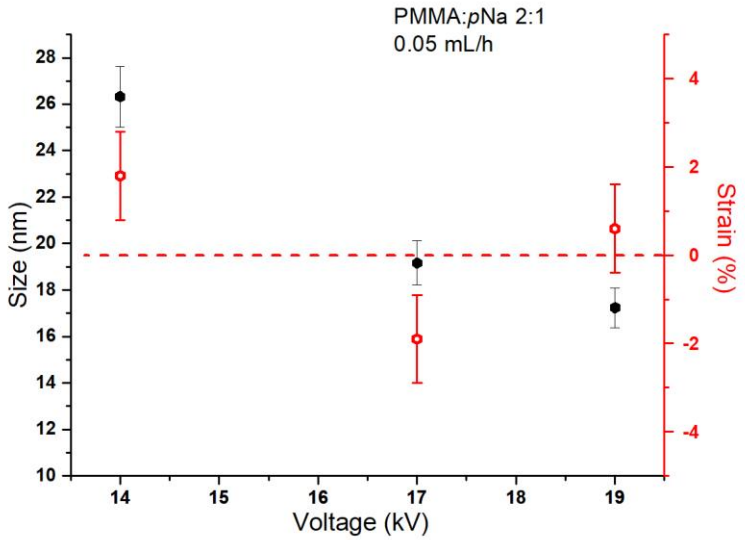

Figure 5 - The W-H analysis of *p*Na –PMMA for different applied voltages keeping the flow rate constant at 0.05mL/h.

Either higher flow rates or a large applied voltage lead to significantly smaller mean *p*Na crystal sizes. We hypothesize that both high flow rates and elevated applied voltages, which provoke higher ejection rates, induce a more rapid solidification of the polymeric jets, reducing the time for nanocrystal growth. The Williamson-Hall analysis indicates that this affects the size of *p*Na nanocrystals as well as their internal strain. The results presented in figure 6 indicate that for a fixed applied voltage, the sign of the local strain is opposite for the smaller and larger nanocrystals. This could be connected with an increase in the surface to volume ratio, leading to an increased interaction with the surrounding matrix. Additionally, the strain can correspond to a combination of radial, axial and shear deformations and the relative weights may vary with the applied voltage which creates a longitudinal electric field along the polymer jet as it initially forms. Overall the estimated effective strain values are relatively high. A possible explanation is that the polymeric solution jet suffers severe torsion and stretching as it forms the Taylor cone. The strain could induce a deformation in the centrosymmetric structure of the nanocrystals, one possible source for the intense macroscopic second harmonic generation (SHG) observed in these fibres. On the other hand, the increase of the surface to volume ratio leads, as well, to a SHG high efficiency, as shown below.

Our group has previously reported the efficient second harmonic generation by the *p*Na nanocrystals inside polymeric nanofibres (Isakov 2014). In this study, the SHG was measured using a polarimetry setup represented in figure 1, an example of which is shown

in Figure 8. Typically, the standard deviation of the maximum SHG signal is around 10%. Figure 9 displays the relation between the nanocrystals size, the local strain, the ratio of the nanofibre diameter to the nanocrystal size and the relative SHG intensity.

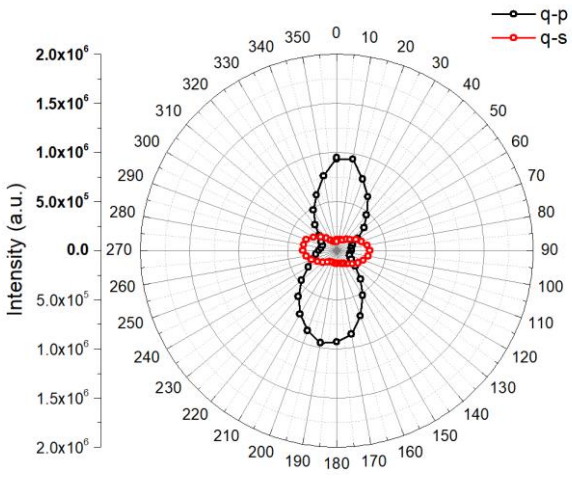

Figure 8 – SHG polarimetry carried out for set of fibres fabricated with a flow rate of 0.05 mL/h and an applied voltage of 14 kV. The q-s and q-p curves correspond to the polarization analyser being oriented perpendicular or parallel to the fibre's longitudinal axis, respectively.

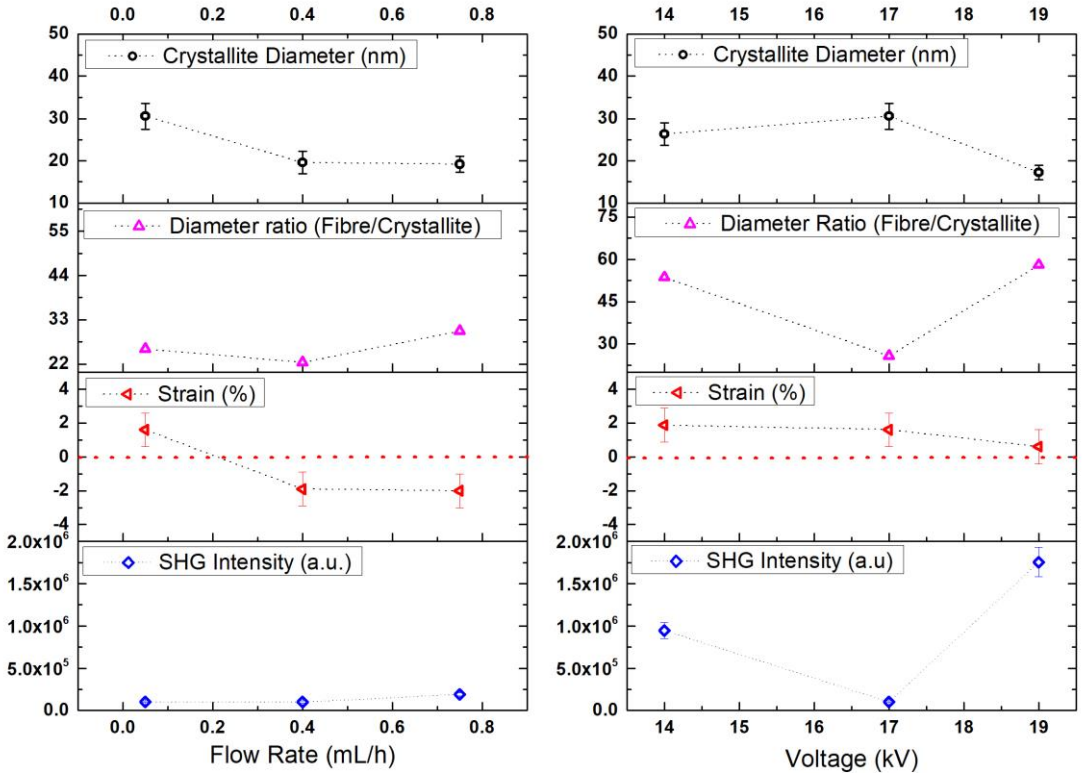

Figure 6 – The variation of the key characteristics of the *p*Na crystals embedded in PMMA fibres as a function of flow rate and applied voltage. The first column corresponds to fibres produced with an applied voltage of 17 kV, while in the second column the flow rate was 0.05 mL/h. The observed SHG intensity is higher for larger ratios of the fibre diameter to the mean *p*Na crystal size. The strains tend to be positive for larger nanocrystals and negative for smaller nanocrystals.

Carrying out a cross-correlation analysis on the different samples, the only parameter to which the SHG signal is statistically correlated is the ratio of the fibre diameter to the mean *p*Na crystal size with a p value of 0.014. This suggests that the strong SHG observed in these PMMA/*p*Na fibres is primarily a surface phenomenon. Given the 2:1 weight ratio used to prepare the precursor solutions, based on the relative densities of PMMA to *p*Na, we expect that on average, the volume fraction of the solidified fibre occupied by *p*Na nanocrystals is approximately 0.30. The total volume of the *p*Na nanocrystals encountered by the incident fundamental laser beam should scale as the square of the fibre diameter and should be independent of the mean *p*Na crystal diameter.

In Figure 10 we plot the variation of the observed second harmonic signal as a function of the mean fibre diameter to mean *p*Na crystal diameter. If the mechanism were simply due to the breaking of the *p*Na centrosymmetric crystalline structure at the *p*Na polymer interface, one would expect that the second harmonic signal would scale as the square of the fibre to *p*Na crystal diameters for a narrow size distribution of *p*Na nanocrystals of uniform shape. This assumes each individual nanocrystal contributes coherently to the SHG signal. The coherent superposition of SHG signals would be expected despite probable phase-mismatches, since the fibre thickness are at most only a few wavelengths of the incident light. However, the best fit to a power law, $SHG \sim \left(\langle D_{fibre} \rangle / \langle d_{pNa} \rangle \right)^n$, yields an exponent of 3.6 rather than a quadratic dependence, although there is a fair amount of uncertainty in this exponent as the 95% confidence interval is $n \in [2.0, 5.2]$. A higher than quadratic dependence might be an indication of a fractal nature for the *p*Na - polymer interfaces.

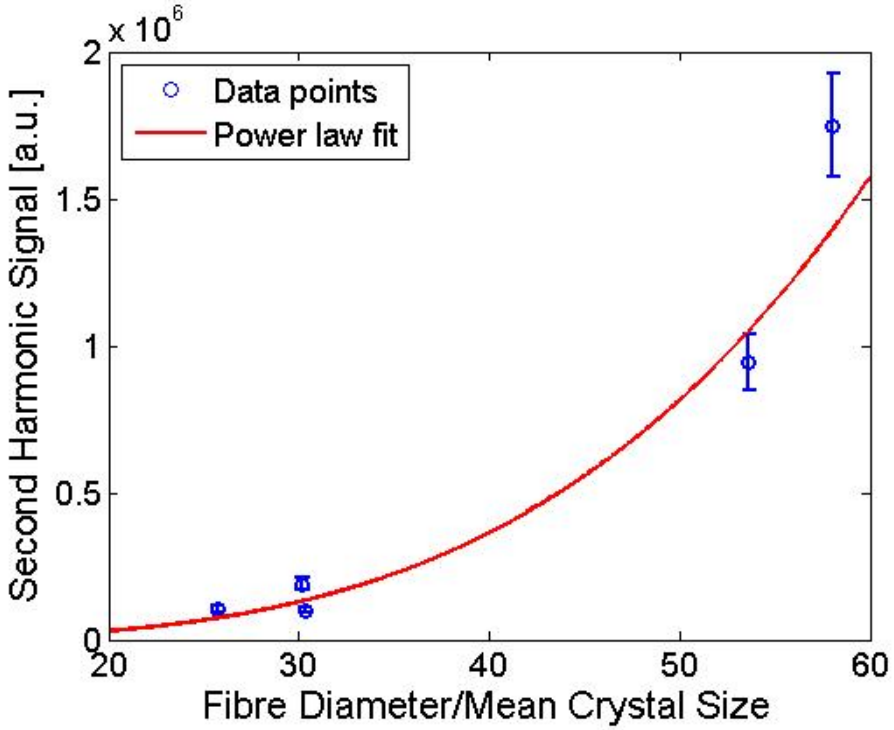

Figure 10: Variation of the measured second harmonic signal in function of the ratio between the mean fibre diameter to *p*Na crystal size ratio. The best nonlinear least weighted least squares power law fit to the data yields an exponent of 3.6 with a 95% confidence interval of [2.0, 5.2].

We note that the estimated response due to a simple symmetry breaking at the *p*Na/PMMA based on the theoretical work of Malagoli and Munn (Malagoli 2000) for the quadratic surface susceptibility of a bulk *p*Na crystal is not sufficient to explain the magnitude of the observed SHG response. Our estimates, described in detail our previous publication (Gonçalves 2018), indicated that the observed response of the fibre produced at a flow rate of 0.05mL/h with an applied voltage of 17 kV are roughly five orders of magnitude greater than the signal that can be expected from two *p*Na crystal surfaces summed coherently. The coherent superposition of the signal arising from N surface scales in intensity as N^2, but even accounting for the approximately 30 crystals that would be encountered, on average, within the fibre diameter, there still remains more than two orders of magnitude for which to account. One possibility is that the surrounding polymeric matrix might have a stronger influence on the structure of the organic crystals when they are smaller in size and that the size distribution of the *p*Na nanocrystals is highly skewed towards smaller sizes. Furthermore, even though, the overall strain estimated from the Williamson-Hall analysis is not well correlated with the observed SHG response, this does not entirely rule out a possible contribution of strain associated with a specific deformation, be it axial, radial or shear. The above Williamson-Hall

analysis can only give a sense of the magnitude of the global strain, not the contributions of the individual types that maybe are more or less effective in promoting a strong second harmonic response.

Conclusion

Detailed *in-situ* characterization of the morphology associated with confinement effects of nanoscale materials can provide crucial information regarding the strength of their response and their potential to be optimized for specific applications. In this study, PMMA-*p*Na nanofibres were produced by the electro-spinning technique and characterized by wide-angle X-Ray scattering at the Elettra synchrotron. The obtained X-ray diffraction patterns suggest that the *p*Na structure of the nanocrystals inside a PMMA matrix is nearly identical to the bulk centrosymmetric structure. The line broadening observed for the resulting nanocrystals was primarily due to the small crystallite size with a lesser contribution played by the average local strain. This broadening was analysed by the W-H method and the respective size-strain plot. From the results, we conclude that the mean *p*Na crystal size is lower at higher flow rates and higher applied voltages. The measured SHG scales with the ratio of the mean fibre diameter to nanocrystal size with a higher than quadratic dependence. While the exact physical origin of the strong SHG response of the electro-spun *p*Na/PMMA fibres remains to be established, this dependence strongly suggests that surface interactions between the *p*Na and the polymer host play an important role Our results suggest that the electro-spinning process is an effective means of producing a large number of *p*Na surfaces within a small volume, leading to a strong effective second harmonic response that is able to compete with the best non-organic nonlinear crystals when normalized for thickness. These electro-spun *p*Na/PMMA fibres are potentially attractive alternatives for applications in which it is advantageous to generate macroscopic second harmonic signals from micron thick materials, such as in the characterization of ultrafast laser pulses.

Acknowledgments

Hugo Gonçalves gratefully acknowledges support from the Portuguese Foundation for Science and Technology (FCT) through the grant PD/BD/111873/2015. The equipment used to characterize the second harmonic response of the electro-spun fibres was acquired within the framework of the Portuguese National Program for Scientific Re-equipment, contract REEQ-25/FIS/2005 with funds from POCI 2010 (FEDER) and FCT. The authors thank Elettra, Trieste Italy for beam time and support through the project 20170363.

Conflict of Interest: The authors declare they have no conflicts of interest

References

Birkholz M (2005), *Thin Film Analysis by X-Ray Scattering*. Weinheim, FRG: Wiley-VCH Verlag GmbH & Co. KGaA.

Boles MA, Ling D, Hyeon T, and Talapin DV (2016), "The surface science of nanocrystals," *Nature Materials,* **15**(2) pp. 141–153.

Chronakis IS (2005), "Novel nanocomposites and nanoceramics based on polymer nanofibers using electrospinning process - A review," *J. Mater. Process. Technol.* **167**(2-3) pp. 283–293.

Duan Y *et al.*(2016), "Aggregation Induced Enhancement of Linear and Nonlinear Optical Emission from a Hexaphenylene Derivative," *Adv. Funct. Mater.* **26**(48) pp. 8968–8977.

Dvornikov AS, Walker EP, and Rentzepis PM (2009), "Two-photon three-dimensional optical storage memory," *J. Phys. Chem. A,* **113**(49) pp. 13633–13644.

Gonçalves H, Saavedra I, Ferreira MR, Caldeira Lopes PE, de Matos Gomes E, and Belsley M (2018), "Efficient second harmonic generation by para-nitroaniline embedded in electro-spun polymeric nanofibres," *J. Phys. D. Appl. Phys.* **51**(10) 105106.

Holzwarth U and Gibson N (2011), "The Scherrer equation versus the 'Debye-Scherrer equation,'" *Nature Nanotechnology* **6**(9) p. 534.

Isakov DV, Belsley MS, De Matos Gomes E, Gonçalves H., Schellenberg P, and Almeida BG (2014), "Intense optical second harmonic generation from centrosymmetric nanocrystalline para-nitroaniline," *Appl. Phys. Lett.* **104**(18) p. 181903.

Islam MM, Bhuiyan MDH, Bredow T, andbTry AC (2011), "Theoretical investigation of the nonlinear optical properties of substituted anilines and N,N-dimethylanilines," *Comput. Theor. Chem.*, **967**(1) pp. 165–170.

Kato M, Kiguchi M, Sugita N, and Taniguchi Y(1997), "Second-Order Nonlinearity of Mixtures Including p-Nitroaniline Derivatives," *Nonlinearity*, **5647**(97), pp. 8856–8859.

Lalama SJ and Garito AF (1979), "Origin of the nonlinear second-order optical susceptibilities of organic systems," *Phys. Rev. A,* **20**(3) pp. 1179–1194.

Li M, Li Y, Zhang H, Wang S, Ao Y, and Cui Z (2017), "Molecular engineering of organic chromophores and polymers for enhanced bulk second-order optical nonlinearity," *J. Mater. Chem. C,* **5**(17) pp. 4111–4122.

Malagoli M and Munn RW (2000), "Microscopic calculation of surface-induced second-harmonic generation in crystals of para-nitroaniline," *J. Chem. Phys.***112**(15) pp. 6757–6762.

Naseri N, Mathew AP, and Oksman K (2016), "Electrospinnability of bionanocomposites with high nanocrystal loadings: The effect of nanocrystal surface characteristics," *Carbohydr. Polym.***147** pp. 464–472.

Ni B and Wang X (2016), "Chemistry and properties at a sub-nanometer scale," *Chem. Sci.*, **7**(7) pp. 3978–3991.

O'Brien MN, Jones MR, and Mirkin CA (2016), "The nature and implications of uniformity in the hierarchical organization of nanomaterials," *Proc. Natl. Acad. Sci.*, **113(**42) pp. 11717–11725.

Ostroverkhova O (2016), "Organic Optoelectronic Materials: Mechanisms and Applications," *Chemical Reviews*, **116**(22) pp.13279–13412.

Pecharsky V and Zavalij P (2009), *Fundamentals of Powder Diffraction and Structural Characterization of Materials*. Boston, MA: Springer.

Shkir M *et al*. (2014), "Optical spectroscopy, crystalline perfection, etching and mechanical studies on P-nitroaniline (PNA) single crystals," *Opt. Mater. (Amst).* **36**(3) pp. 675–681.

Varughese S (2014), "Non-covalent routes to tune the optical properties of molecular materials," *J. Mater. Chem. C*, **2**(18) p. 3499.

Werner L, Caro J, Finger G, and Kornatowski J (1992), "Optical second harmonic generation (SHG) on p-nitroaniline in large cyrstals of AIPO4-5 and ZSM-5," *Zeolites*, **12**(6) pp. 658–663.

Williamson, G.K. and Hall, W.H. (1953) X-Ray Line Broadening from Filed Aluminium and Wolfram. Acta Metallurgica, **1**, pp22-31

Zak AK, Majid WHA, Abrishami ME, and Yousefi R (2011), "X-ray analysis of ZnO nanoparticles by Williamson-Hall and size-strain plot methods," *Solid State Sci.***13**(1) pp. 251–256.

Self-assembled para-Nitroanaline polymeric thin films as highly efficient generators of second harmonic light.

Hugo Gonçalves[a], Marlene Lúcio[a], Paulo E Lopes[b], César Bernardo[a] Michael Belsley[b]

[1] Centre of Physics, University of Minho, Campus de Gualtar, 4710-057 Braga, Portugal
[2] Institute for Polymers and Composites/i3N, University of Minho, Guimarães, Portugal

Abstract: Intense well-polarized second harmonic light was generated by *para*-Nitroaniline self-assembled thin films in different polymeric host matrices. The large area films of the organic chromophore with a thickness of a few microns were produced using a modified version of capillary growth. Analysis of the generated second harmonic light indicates that the *para*-Nitroaniline molecules, which nominally crystalize in a centrosymmetric space group, were organized into non-centrosymmetric structures with an appreciable second order susceptibility dominated by a single tensor element. Under the best conditions, films effective nonlinear optical susceptibility is slightly greater than that of beta barium borate. Generalizing this approach to a broad range of organic molecules with strong individual molecular second order nonlinear responses, but which ordinarily form centrosymmetric organic crystals, could open a new pathway for the fabrication of efficient sub-micron sized second harmonic light generators.

PACS: 42.65.-k Nonlinear optics**; 42.65.An** Optical susceptibility; hyperpolarizability, **42.65.Ky** Frequency conversion; harmonic generation; **42.70.Jk** Polymers and organics

Declarations of interest: none

1. Introduction

Over the past decades, scientists have sought strategies to enhance the nonlinear optical response of organic molecules and polymers and to incorporate them into assemblies with high optical and thermal stability, as well, as the good optical transparency needed for most practical applications[1–6]. More often than not, the large individual molecular first order hyperpolarizabilities of the developed organic chromophores are associated with large dipolar moments in the ground state leading to strong interactions between the constituent molecules in these assemblies and a tendency to assemble in head to tail centrosymmetric structures that preclude stable and strong macroscopic second order nonlinear optical responses[7,8].

The arrangement of the molecular building blocks within supramolecular structures has a marked effect on their physical properties[9]. The development of techniques for controlling the spatial arrangement of the individual components of a composite material at the nanometre and

micrometre scale is, therefore, crucial to the design and fabrication of advanced electronic, optical, and mechanical materials[7,10–12]. *para*-Nitroaniline (*p*Na) is an organic chromophore with an appreciable molecular hyperpolarizability (β)[13,14], often considered a model for organic donor-acceptor systems with strong second order molecular responses[15–17]. However, *p*Na molecules tend to arrange themselves in an antiparallel centrosymmetric fashion in the solid state, causing their individual even order molecular non-linearities to cancel, making the bulk SHG signal vanish. Various methods to prevent this alignment have been proposed, including the introducing of chiral substituents, aligning the chromophores by a strong externally applied electric field or confined within 1D nanostructures and host-guest complexes [18–24].

Our group has previously reported that electro-spun nanofibers embedded with *p*Na can be efficient generators of second harmonic light [4,21], well beyond what can be expected due to the breaking of centrosymmetry at the *p*Na bulk crystalline surfaces [4]. This implies that the electrospinning process is able to somehow break the nominal centrosymmetry of the *p*Na embedded in the polymeric fibers. One possibility is that the strong DC electric field applied to eject the jet in the electro-spinning process induces subtle distortions into the *p*Na nanocrystals, or provokes a local polarization of the surrounding polymer which is then frozen into the fiber as it rapidly solidifies. To test whether the electric field is an essential stimulus for obtaining strong second harmonic responses we explore here growing *p*Na together with various polymers in a confined geometry. We have found that *p*Na thin films with a high SHG response can be cast using a series of linear aliphatic polymers with different molecular weights and with varying degrees of crystallinity; from amorphous to semi-crystalline. These films were obtained using a variation of capillary growth, by placing a precusrsor polymer *p*Na solution between the surfaces of two closely spaced glass slides. That is instead of restricting the *p*Na nanocrystals geometries by the physical dimensions of the ejected polymer jet in electro-spinning, the self-assembly of *p*Na crystals was restricted to the limited space on the order of a micron between the glass slides.

We have characterized the SHG response of the resulting thins films. For polymers with sufficient length, their inherent flexibility is the key factor determining the organization of the resulting *p*Na thin films. Two distinct co-crystallization mechanisms were observed. Long chain polymers, tended to produce largely continuous planar *p*Na films, whereas shorter polymer chains gave rise to dendritic arrangements. These different assemblies lead to different second harmonic responses as well as notable differences in the respective Raman spectra.

2. Experimental Section

Methods

Para-Nitroaniline (*p*Na) was purchased from Sigma Chemical Co and used as received. Polystyrene (PS) with a molecular weight (M_W 300000) was purchased from Alfa Aesar. Both Poly(hexano-6-lactone) (PCL) with (M_W 80000) and Poly(methyl methacrylate) (PMMA) with medium (M_W 120000) and low (M_W 15000) molecular weights were acquired from Sigma Chemical Co. The polymeric raw materials were dissolved in toluene ($C_6H_5CH_3$, 99.8%), purchased from Sigma-Aldrich. The prepared solution was stirred for several hours under ambient conditions. *p*Na in powder form was subsequently added to the polymeric solution, in a ratio of 2:1 polymer to *p*Na by weight, together with a few drops of acetone to aid solvation. The respective polymeric solutions with a concentration 10 wt% were deposited on glass microscope slides. The deposited solutions were covered with thin glass coverslips. The growth of the films was a slow process, occurring over several days.

Thin film fabrication

The thin films studied are quasi two-dimensional systems, with a thickness slightly greater than one micron, produced under ambient conditions at a constant temperature. In this approach the growth of the *p*Na films were geometrically restricted to the narrow gap between the two glass slides, similar to the capillarity growth process reported in the literature[25,26], see figure 1.

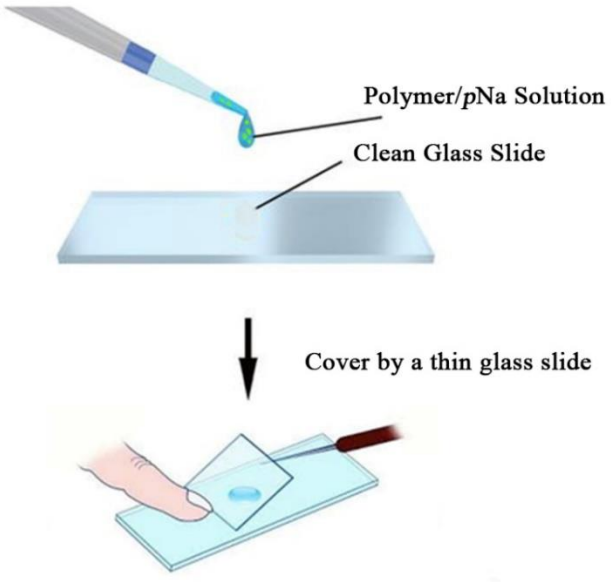

Figure 1 – The method used to obtain the two-dimensional *p*Na-polymeric thin films.

The resulting *p*Na/polymeric thin films become visible to the naked eye after a few days. However, they continuously grow as long as some residual mobility in the polymeric matrix exists, that is until complete evaporation of the toluene. The resultant morphologies depend on the respective host matrix; different polymeric matrices lead to distinct *p*Na nanostructures.

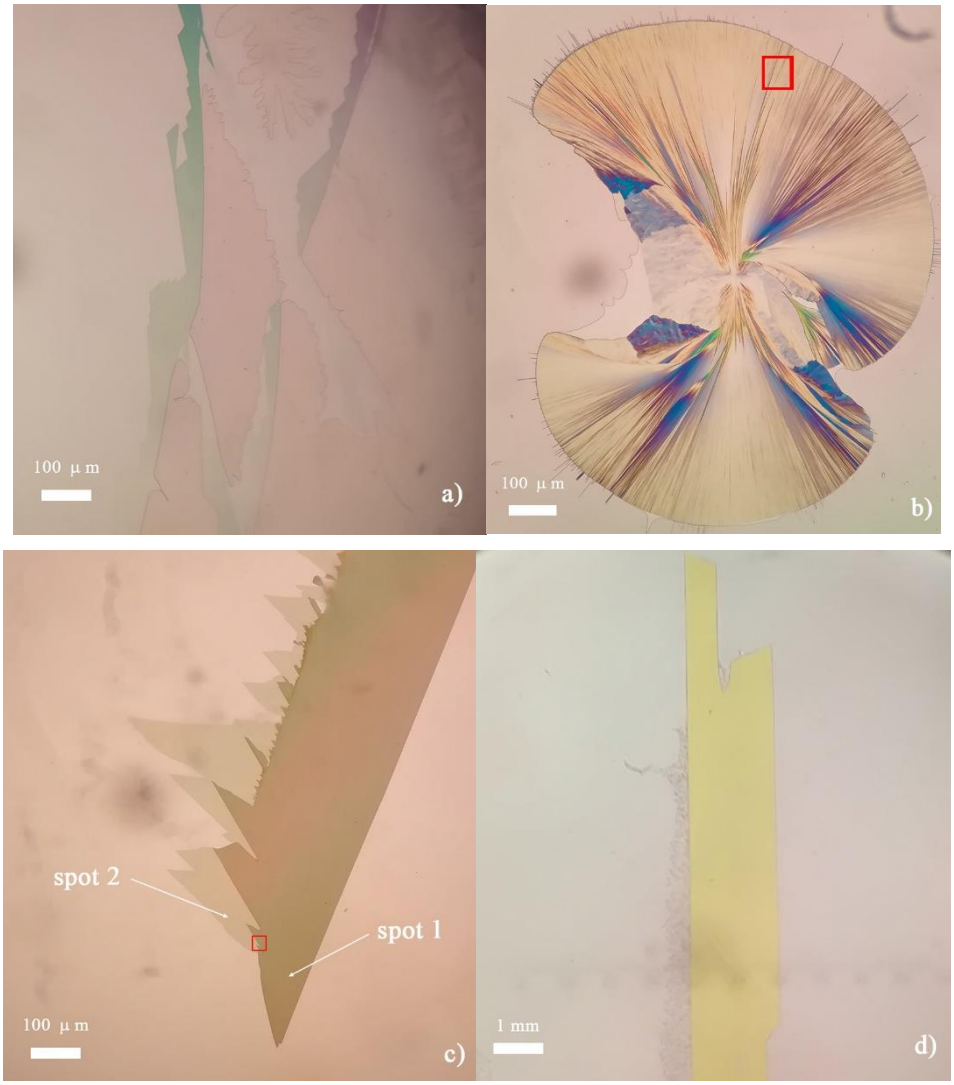

Figure 2 – Several representative *p*Na thin films obtained using different polymeric matrices: a) a PS matrix, b) low molecular weight PMMA, c) medium molecular weight PMMA and d) PCL matrix. The images were taken using a microscope equipped with a combination polarizer/analyser under incoherent white light illumination.

In Figure 2 several differences are visible between the thin films. The PS matrix leads to a considerable number of forms with relatively large elongated sizes the majority of which have at least one sharp edge. By contrast, PCL, with a tendency to form a semi-crystalline matrix, leads a small number of elongated rectangular shaped *p*Na structures with relatively sharp edges. The *p*Na structures obtained in PMMA matrices vary with the PMMA mean molecular weight.

For low molecular weight PMMA, conical and needle-like forms arise, whereas medium molecular weight PMMA leads to layered *p*Na films with a mixture of sharp and jagged edges.

3. Experimental characterization

AFM Measurements

AFM imaging was performed under ambient conditions in air with a Nanosurf FlexAFM (Paralab SA, Portugal) instrument with a 100×100 μm^2 head. The measurements were carried out in tapping mode employing a Tap190Al-G from BudgetSensors, with a resonance frequency ~190 kHz and a force constant of 48 N/m.

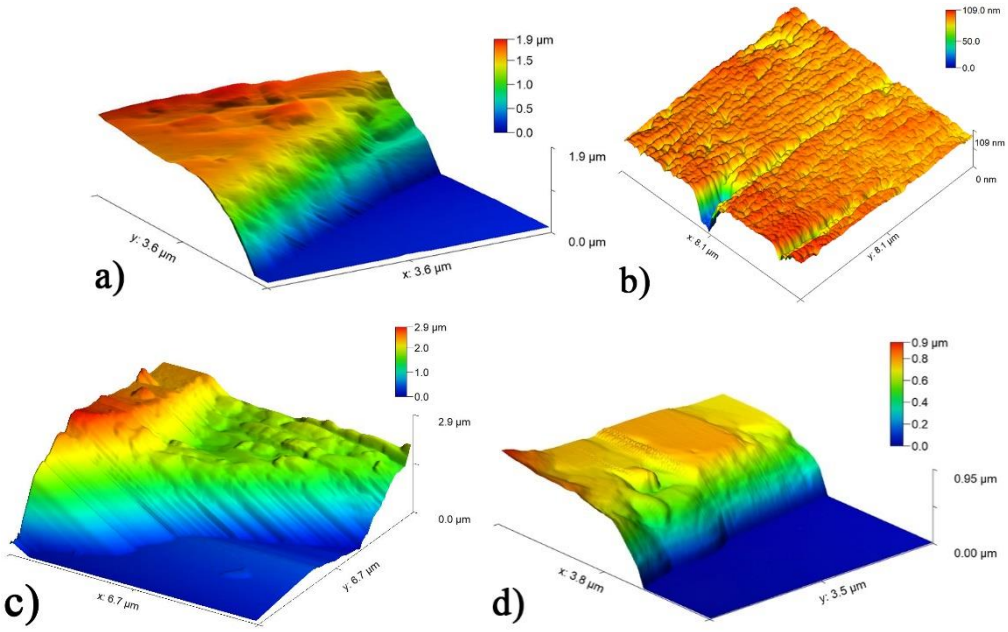

Figure 3 – AFM topography of the surface of films presented in Figure 2 and the respective thicknesses. In a) PS matrix, b) low molecular weight PMMA, c) medium molecular weight PMMA and d) PCL matrix. The samples were partially destroyed during separation of the glass slides necessary to perform the measurement. The measurements were performed at the edge of the thin film structures. In the cases of the low and medium weight PMMA matrices, the specific location is marked with a red square in Figure 2b and 2c.

The AFM images show evidence of a compact packing of the self-assembled *p*Na films which depends on the polymer host. Films grown in the presence of long chain polymeric matrices tend to have sharp-edges, sometimes assuming a layered structure, with smooth planar surfaces of sub-micron height. There are no noticeable ruptures, folds or fissures. On the other hand, films grown in the presence of small chain polymeric matrices give rise to textured granular surfaces, ordered in conical shapes and needles with no apparent order or growth orientation.

Wide-angle X-ray scattering

Taking advantage of the micro-focus wide-angle x-ray scattering beam line (MiNaXS)[27] at PETRA III at DESY in Hamburg, Germany the crystallographic orientation of the *p*Na thin films were investigated. The micro beam with a 13.43 keV of energy at the P03 end station, focused down to a size of $1\times1\mu m$ was employed. The corresponding X-Ray diffraction patterns were recorded using a Pilatus 1K detector system with a pixel size of 172 µm. As might be expected from the above polarizing microscope images, the micro focused X-Ray scattering measurements reveal that the *p*Na films grown in PMMA with low molecular weight do not have a preferential crystal orientation.

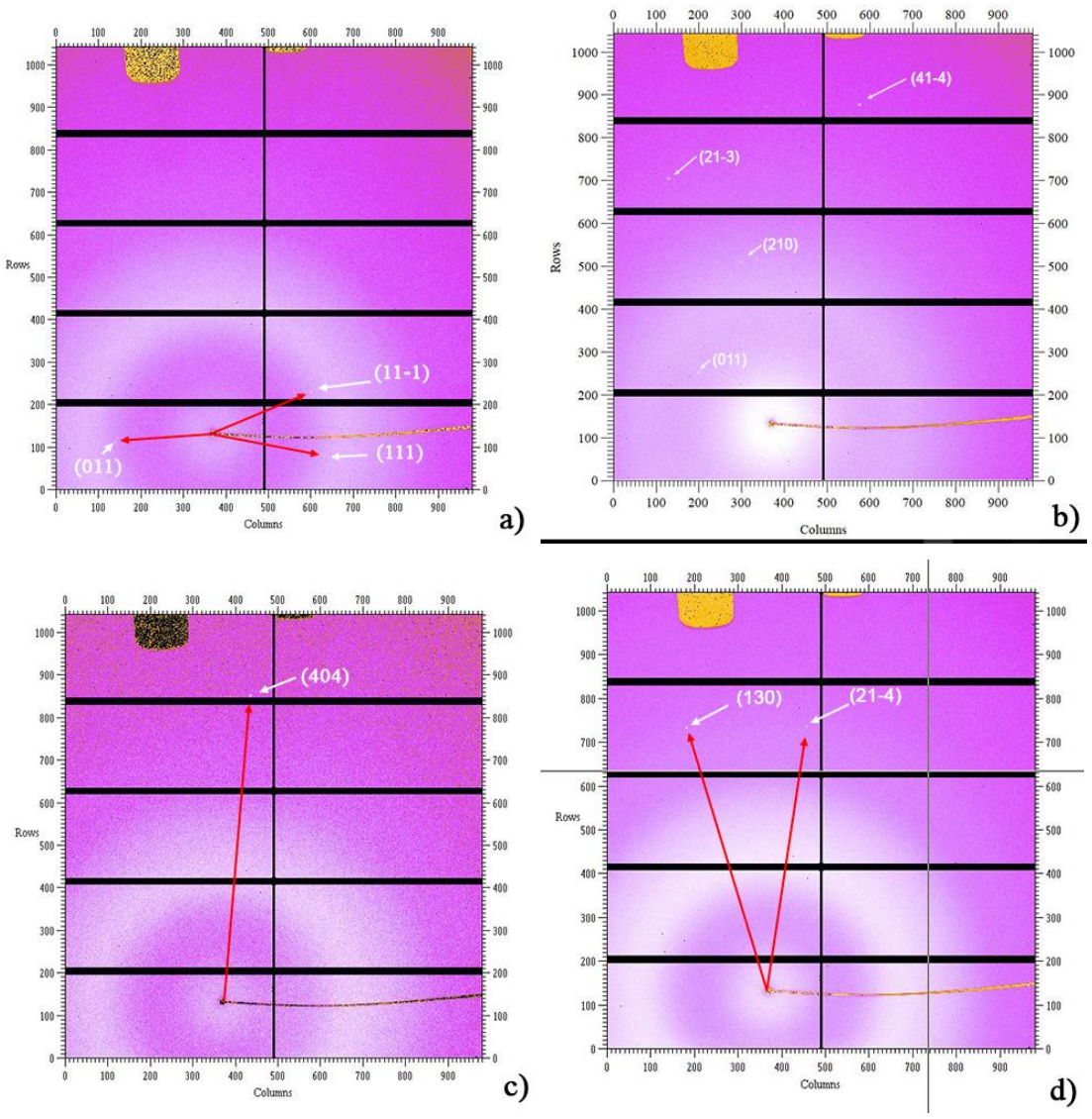

Figure 4 – X-Ray diffractograms of the thin films presented in Figure 2. The red arrow represents the **Q** vector normal to the diffracting planes. (a) *p*Na/PS matrix, (b) *p*Na/low molecular weight PMMA, (c) *p*Na/medium molecular weight PMMA and (d) *p*Na/PCL matrix.

However, the thin films obtained in the host matrices of PS, PMMA (medium molecular weight) and PCL produce fewer peaks, raising the possibility of preferential orientation of the pNa crystals. The strongest peak observed for the *p*Na crystals grown in the presence of PS has Miller indices of [1 1 -1] with weaker peaks at [0 1 1] and [1 1 1]. PMMA medium molecular weight polymers encouraged growth that gave rise to an intense peak with Miller indices of [4 0 4], while the PCL matrix produced a film with the strongest reflection indexed as [1 3 0] and a much weaker [2 1 -4] reflection , see Table 1. In contrast, the films obtained using the PMMA matrix with lower molecular weight produced a number of diffraction peaks indicating the presence of multiple orientations. This is consistent with the AFM topography of its surface suggesting a random agglomeration of *p*Na nanocrystals. We note that for all of our samples it is very likely that several prominent lower angle diffraction peaks are obscured by the strong background diffraction rings produced by the polymer and glass supports.

Table 1 – Identified x-ray diffraction angles of the *p*Na crystals in the respective polymeric matrices and the respective theoretical values based on the structure of [28].

Structure	Miller Indices	Observed 2θ (degrees)	Theoretical 2θ (degrees)
*p*Na/PS	[011]	10.69	10.68
	[11-1]	11.45	11.44
	[111]	11.53	11.56
*p*NA/PMMA	[404]	30.67	30.70
*p*Na/PCL	[130]	26.63	26.69
	[21-4]	27.47	27.54

Raman analyses

A high-resolution Raman spectrometer, Horiba LabRAM HR Evolution confocal microscope using a laser excitation at 532 nm (2.33 eV), was employed to characterize the bulk molecular order and orientation of the *p*Na in all the different thin films. A 100x objective lens was used to focus the laser onto the sample. Polarized Raman spectra were obtained at room temperature between 600-1800cm^{-1} corresponding to the internal molecular vibrations. The Raman spectrum of *p*Na is sensitive to its physical phase state[29–31]. The most salient feature of crystalline *p*Na's Raman spectra is a broad intense peak at 1282 cm^{-1}. In Figure 5, the Raman bands of the films displayed in figure 2b) and 2c) present three prominent lines at 862 cm^{-1}, 1282 cm^{-1} and 1316 cm^{-1} all of which can be assigned to the Raman spectrum of *p*Na in its crystalline form. On the other hand, the Raman bands of the films displayed in 2a) and 2d) are dominated by

two lines at 862 cm^{-1} and 1276 cm^{-1} with a substantial red shift (≈ 6 cm^{-1}) in relation to the other films and the bulk crystalline form. The most striking feature of Figure 5 is the absence of the Raman band cantered at 1316 cm^{-1} and a red shift of ≈ 6 cm^{-1} and a broadening of ≈ 5 cm^{-1} in the band 1282 cm^{-1} in the spectra corresponding to films grown in PS and PCL hosts.

The peaks centered at 1282 cm^{-1} is attributed to a Fermi resonance between a symmetric benzene ring vibrations and a combination line from a lower frequency symmetric ring vibration and the torsion motion of the amine group [30]. The strength of this resonance is sensitive to the localization of the π electrons. In the crystalline state, strong hydrogen bonding promotes an increase of the electron density around the C-N bonds with the amine and nitro groups, leading to a pseudo-quinoidal configuration enhancing the intensity of the ω_3 Raman band. In contrast in non-polar liquids, the π electron cloud assumes a largely aromatic distribution and the Raman peak near 1280 cm^{-1} is reduced in intensity. Harrand has shown [30] that for crystalline *p*Na this intense band shifts and narrows with increasing temperature moving from 1276.8 cm^{-1} at 30 K to 1284.4 cm^{-1} at 300 K, reflecting a blue shift with an increase in the intermolecular distances. This suggests that the red shift of the 1280 cm^{-1} band observed for the *p*Na/PS and *p*Na/PCL systems might be associated with smaller intermolecular distances and consequently slightly stronger hydrogen bonding.

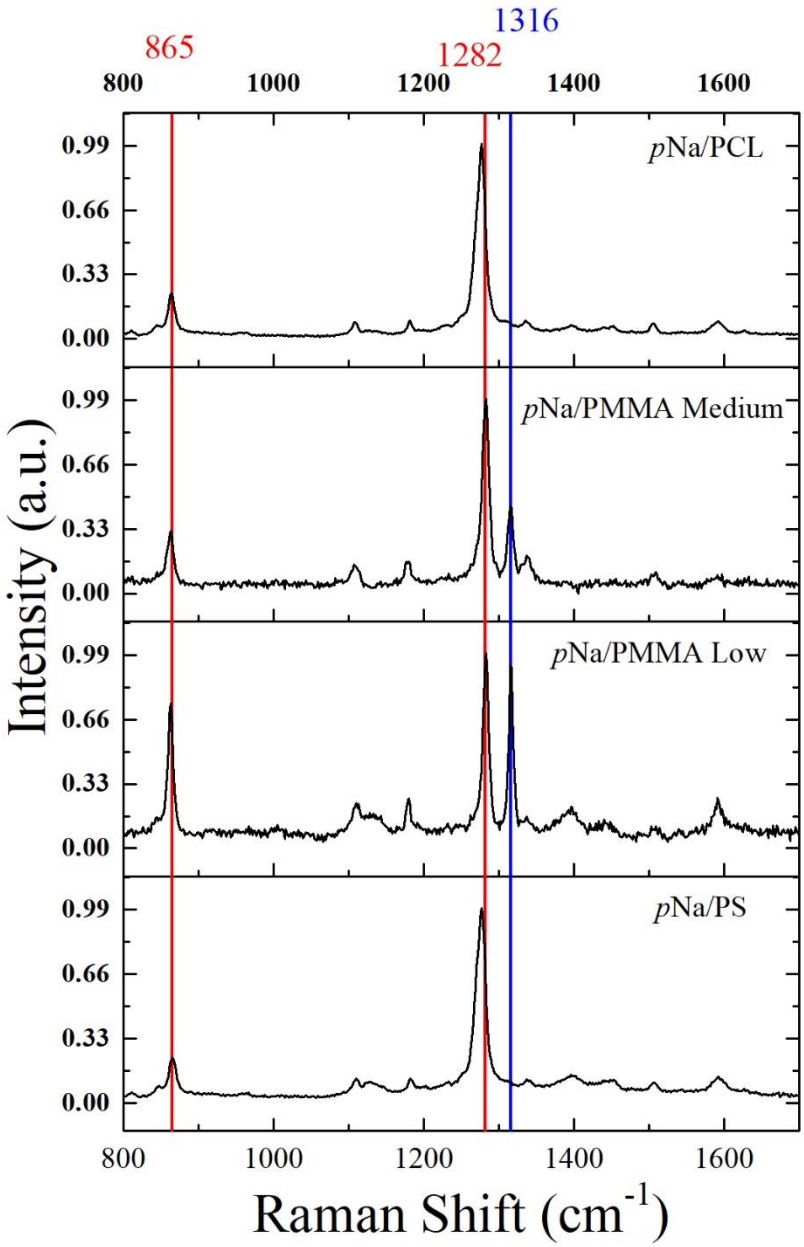

Figure 5 – Raman spectrum of the films represented in Figure 2. A red shift is observed in the peak characteristic of the crystalline state at frequency $\nu = 1284\,\mathrm{cm}^{-1}$ in the spectra of Figure 2a) and 2d).

The Raman line near 1316 cm^{-1} was assigned by Harrand [30] to a bending motion of the CH groups, while that at approximately 865 cm^{-1} is associated with a bending mode of the nitro group. Both of these bands are less intense relative to the main 1282 cm^{-1} line in the *p*Na/PS and *p*Na/PCL films, while the lower weight PMMA enhances their relative intensity. We suspect that the relative decrease in the 1282cm^{-1} line observed in the low weight PMMA system indicates a more random orientation of the *p*Na nanocrystals reducing the projection of the mode onto the incident laser polarization. We note that this film generates very little if any second harmonic light and produces the weakest Raman signal overall. In contrast, the *p*Na/PS and *p*Na/PCL films have the

strongest Raman response. The Raman bands of the medium weight PMMA thin film, (that of figure 2c) represent an intermediate arrangement. There is no shift in the 1282 cm^{-1} peak, but the peak at 1316 cm^{-1} is reduced in intensity as is the NO_2 bending mode at 865 cm^{-1}. This might reflect the better orientational order of the *p*Na grown in the presence of medium weight PMMA.

Polarimetry measurements

The SHG response of the *p*Na films was analysed as a function of the polarization direction of the incident light. The incident fundamental light (at frequency ω) was provided by a femtosecond Ti:Sapphire mode-locked laser (Coherent Mira 900F) pumped by a frequency doubled CW Neodymium-laser (Coherent Verdi 5W). The incident light had a 100 femtosecond (fs) temporal pulse width and a central wavelength of 800nm. The measurement consists in illuminating the *p*Na films with different polarization orientations and collecting and analysing the transmitted SHG field. An achromatic half-wave plate ($\lambda/2$) is placed before a 10× microscope objective with a numeric aperture (NA=0.25), in order to continuously vary the polarization direction of the incident light (0 – 360º). The SHG field is collected through a microscope objective 100× Mitutoyo Plan infinity-corrected long working distance objective (NA=0.7). A set of filters were used to reduce the incident beam intensity and select the SHG field with a central frequency of 2ω. Before detection the generated second harmonic light was analysed using a linear polarizer, fixed to be either parallel to the incident polarization that gave rise to the highest SHG signal (q-p configuration) or perpendicular to this polarization (q-s configuration) to the incident beam polarization that produced the largest SHG signal. The analysed SHG field was recorded by focusing the beam into an optical fiber bundle connected to the entrance of a 0.3meter imaging spectrograph (Andor Shamrock SR-303i), with 0.20 nm resolution (see Figure 6).

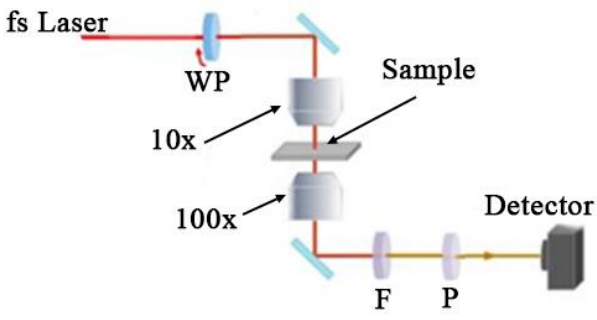

Figure 6 - Polarimetry Setup. The sample is excited by a linearly polarized Ti:Sapphire laser beam. The polarization of the incident beam is continuously varied using an achromatic half-wave wave plate (WP – λ/2). A 10x objective is used to focus the beam on the sample. The SHG is collected via a 100x objective. A set of bandpass filters are used to eliminate the fundamental

beam. After passing through a fixed polarization analyser (P) the SHG signal is detected using a cooled CCD array coupled to a 0.3 m spectrograph.

The polarimetry study of the different *p*Na films are shown in Figure 7. The stronger responses were obtained for the *p*Na films grown in PS and medium weight PMMA. For these the energy per incident pulse was approximately 17 pJ corresponding to a peak power of order 200 W. The film grown with the PCL host required a higher incident energy of roughly 660 pJ, nearly 40 times greater.

Except for the *p*Na/PCL film, the SHG polarization dependence is dominated by a cosine squared type variation indicating the dominance of a single nonlinear dipolar response orientated in the thin film plane. Consequently, *p*Na thin films grown in PS and medium weight PMMA create nonlinear mediums where the SHG signal is dominated by a single element of the second order susceptibility tensor. However, since the growth orientation are different between them, the respective tensor element corresponds to a distinct plane in each film. The clover leaf pattern of the signal form the sample grown in the presence of PCL is indicative of a cross-polarization dependence, typical of the situation when two elements of the second order susceptibility tensor, related by symmetry, have equal magnitudes. The pattern is similar to one that would be generated by a crystal with $\bar{4}2m$ symmetry such as Potassium diphosphate (KDP).

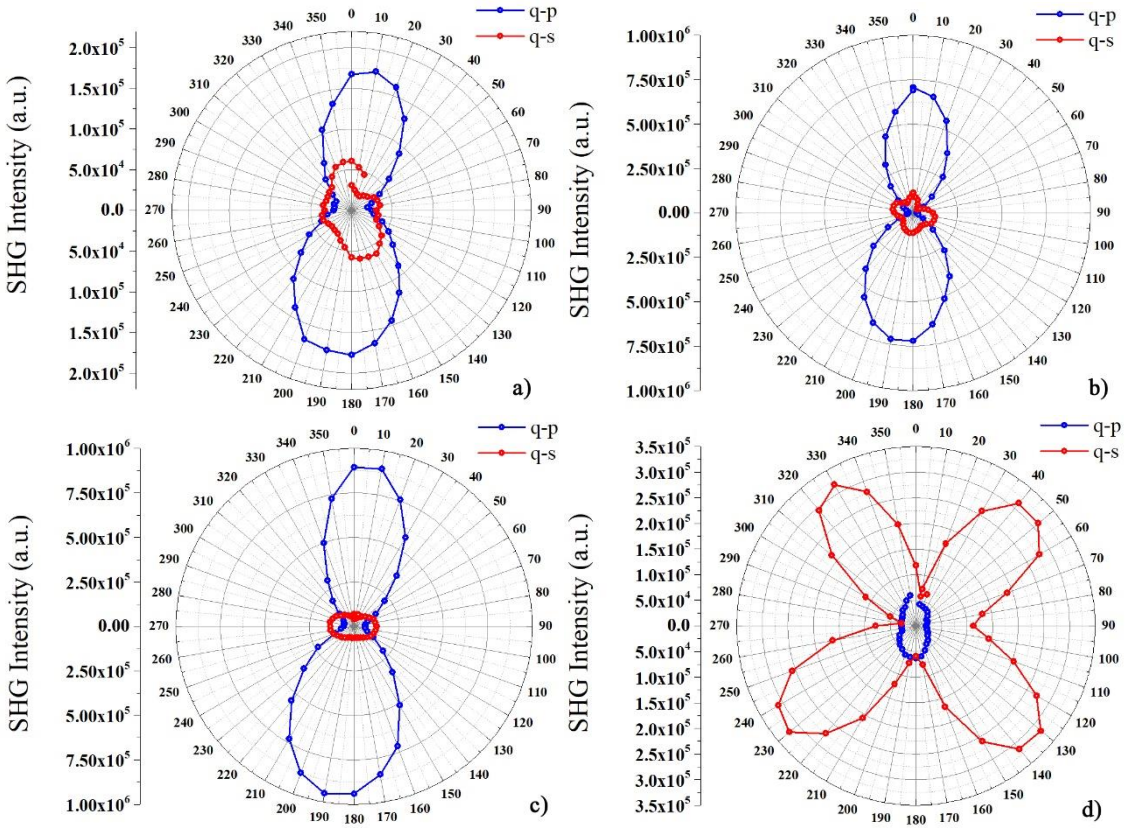

Figure 7 - Polar plots of the SHG intensity of the pNa-polymer films represented in Figure 2. a) displays the SHG polarimetry data of the *p*Na-PS thin film shown in Figure 2a), acquired using an incident beam with an average pulse energy ≈ 17 pJ. b) and c) display the SHG polarimetry data for the pNa-medium weight PMMA films obtained at the illuminated spots 1 and 2 respectively as marked in Figure 2c). The incident beam had average energy per pulse ≈ 17 pJ. d) shows the data of the *p*NA-PCL film displayed in Figure 2d). In this case the SHG signal was much lower, requiring a higher average incident energy per pulse of ≈ 660 pJ.

Second order response estimates

To calibrate our SHG polarimetry system we replaced the *p*Na thin film samples by a 1 mm thick beta barium borate (BBO) crystal. For these measurements, the incident fundamental light consisted of pulses with an approximate energy of 4 pJ, a FWHM duration of 100 fs and a $1/e^2$ diameter of 6 mm. Using a x10 microscope objective with a numerical aperture of 0.25 to focus the fundamental beam onto the BBO crystal, we estimate that the focused fundamental beam diameter is roughly 2.2 μm within the crystal. Under this tight focusing, it is necessary to take into account spatial walk-off of the second harmonic beam due to the crystal birefringence. Wang and Weiner have developed a theoretical expression taking into account both spatial walk-off and the temporal walk-off effects due to group velocity mismatch between the fundamental and second harmonic beams [32]. Assuming an incident beam with transverse spatial and temporal profiles well described by Gaussians, their asymptotic expression for the second harmonic generation conversion efficiency is given by,

$$\eta_{2\omega}^{BBO} = \frac{U_{2\omega}^{BBO}}{U_{\omega}^{BBO}} = \sqrt{2\ln(2)}\,\frac{\gamma U_{\omega}^{BBO} l_{S-T}}{t_p}\tan^{-1}(\mu) \qquad 1$$

Here U_ω and $U_{2\omega}$ are the energies of the incident fundamental and generated second harmonic pulses, t_p is the FWHM pulse duration of the fundamental beam, while μ is the ratio of the crystal thickness L to the incident beam's confocal length. In our situation $\mu \simeq 63$ indicating a very tight focusing limit and allows us to replace $\tan^{-1}(\mu)$ by its limiting value of $\pi/2$. The parameter l_{S-T} represents an effective length over which the fundamental and second harmonic beams propagate together before separating due to the crystal birefringence or the group velocity mismatch. It is given by summing in quadrature the spatial and temporal effects according to the expression

$$l_{S-T} = \left[\left(\frac{\rho}{\omega_0}\right)^2 + 2\ln(2)\left(\frac{\beta}{t_p}\right)^2\right]^{-1/2} \qquad 2$$

where ρ denotes the angle between the ordinary and extraordinary ray's pointing vectors and β represents the group velocity mismatch between the fundamental and second harmonic beams. In our case these values are $68\ mrads$ and $194\ fs/mm$ respectively for SHG of 800nm in BBO by type I phase matching. The parameter ω_0 is the $1/e^2$ radius of the fundamental beam at its focus within the BBO crystal. We estimate that for our case $l_{S-T} \approx 16\ \mu m$ and is dominated by the spatial walk-off. Finally, γ represents a scaled nonlinear coupling coefficient and is given by,

$$\gamma = \frac{4\omega^2 {d_{eff}}^2}{n_\omega n_{2\omega} \lambda_0 c^3 \varepsilon_0} \qquad 3$$

with $d_{eff} = 2.0\ pm/V$ the effective second order nonlinear coefficient for SHG via type I phase matching of 800nm light with a BBO crystal, n_ω and $n_{2\omega}$ are the respective refractive indices of the two beams (both are equal to 1.660) and $\lambda_0 = 800\ nm$ is the fundamental wavelength in air. In our case $\gamma \approx 1.7 \times 10^{-2}\ s/Jm$. Substituting these values into equation (1) we estimate the second harmonic efficiency of our system to be $\eta \approx 2x10^{-4}$ well into the non-depletion regime.

Momentarily, let us assume that the observed SHG generated by the *p*Na films arises from the symmetry breaking at the surfaces. The SHG power generated by the surfaces can be described in terms of an effective surface susceptibility using the approach of Brevet[33]. According to his theoretical development, the SHG efficiency arising from a single *p*Na crystalline surface would be given by the following expression,

$$\eta_{2\omega}^{pNa} = \sqrt{\frac{2\ln 2}{\pi}} \frac{4\omega^2 \left[\chi^{(2s)} \right]^2}{n_\omega n_{2\omega} \lambda_0 c^3 \varepsilon_0} \frac{U_\omega^{pNa}}{b t_p} \qquad 4$$

Here, $\left(\chi^{(2s)} \right)$ is the effective quadratic surface polarization, while b is the confocal length of the incident fundamental beam (in air) and is approximately equal to 550 μm. Small correction factors related to the Fresnel reflection and transmission coefficients have been ignored in equation 4. Combining the above expressions, we can readily obtain an estimate for the quadratic surface susceptibility of the *p*Na films,

$$\chi_{pNa}^{(2s)} = d_{eff}^{BBO} \frac{U_\omega^{BBO}}{U_\omega^{pNa}} \sqrt{\left(\frac{S_{2\omega}^{pNa}}{S_{2\omega}^{BBO}} \right) \left(\frac{\sqrt{\pi^3}}{2} l_{S-T} b \right)} \qquad 5$$

where $S_{2\omega}^{(BBO,\,pNa)}$ is the second harmonic signal measured for the BBO crystal or *p*Na/polymeric thin film and is proportional to the energies of the respective second harmonic pulses. We have

ignored small factors related to differences in the refractive indices of the BBO crystal and the *p*Na thin films. The respective estimates are reported in Table 2.

Table 2 - Estimates for the effective quadratic surface susceptibility and effective material quadratic susceptibility of the *p*Na/polymeric thin films

Material	Thickness, L (μm)	Incident pulse energy, U_ω (pJ)	SHG $S_{2\omega}$ (au)	$\chi^{(2s)}$ (nm^2/V)	d_{eff}^{pNa} (pm/V)
BBO	$1.0x10^3$	4	$1.11x10^8$	_	2.0
*p*Na/PS	1.9	17	$1.78x10^5$	2.9	1.5
*p*NA/PMMA (Spot 1)	2.7	17	$7.06x10^5$	5.8	2.1
*p*NA/PMMA (Spot 2)	2.0	17	$9.52x10^5$	6.7	3.3
*p*Na/PCL	0.9	660	$3.23x10^4$	0.03	0.03

Alternatively, if the second harmonic light is generated throughout the thickness of the thin pNa crystal one can use the standard plane wave result for estimating the effective quadratic susceptibility coefficient, d_{eff}^{pNa} ,

$$\eta_{2\omega}^{pNa} = \frac{4\omega^2 \left[d_{eff}^{pNa} \right]^2}{n_\omega n_{2\omega} \lambda_0 c^3 \varepsilon_0} \sqrt{\frac{2\ln 2}{\pi}} \frac{U_\omega^{pNa} L_{pNa}^2}{b t_p} \qquad 6$$

Since the propagation of the fundamental light within the thin films is on the order of a few wavelengths phase mismatch between the fundamental and second harmonic waves can be safely ignored. In addition, neither temporal separation nor spatial separation, due to group velocity mismatch and birefringence respectively, are relevant. Combining this relation with equation 1 we arrive at the following estimate for the effective quadratic susceptibility of the *p*Na thin films,

$$d_{eff}^{pNa} = d_{eff}^{BBO} \frac{U_\omega^{BBO}}{U_\omega^{pNa}} \sqrt{\left(\frac{S_{2\omega}^{pNa}}{S_{2\omega}^{BBO}} \right) \left(\frac{\sqrt{\pi^3} l_{S-T} b}{2 L_{pNa}^2} \right)} \qquad 7$$

Again we have ignored small corrections that take into account the difference in the refractive indices of the nonlinear media. The above relation is used to estimate the last column of values in Table 2.

Using equation 5 the $\chi^{(2s)}$ for the *p*Na films grown with PS (Figure 2a) is roughly $\chi^{(2s)} \simeq 3\,\mathrm{nm}^2/\mathrm{V}$, roughly a factor of twenty below that estimated for *p*Na nanocrystals

assembled inside of PMMA polymeric electrospun nanofibers [4]. For the *p*Na crystals grown with medium weight PMMA the values obtained are factors of 2 and 2.3 greater for the two different spots measured (se figure 2c). Finally, the signal from the *p*Na/PCL films of Figure 2d) leads to an estimate which is roughly a factor of 100 lower than the *p*Na/PS sample. We note however that these estimates are for a single surface, whereas it is quite likely the eletrospun fibers contain multiple *p*Na nanocrystals within the area illuminated by the incident fundamental beam. In comparison, the quadratic surface susceptibility values estimated theoretically by Malagoli and Munn [34] for an isolated surface of a bulk *p*Na crystal are three orders of magnitude lower than the above estimates for the *p*Na medium weight PMMA system. The highest surface quadratic susceptibility tensor element they estimate is $\chi_{zzz}^{(2s)} = -1.416\times10^{-3}\,\mathrm{nm}^2/\mathrm{V}$ for a surface with Miller indices of (004). This implies that the large second order nonlinear response of these systems must be due to an interaction with the underlying polymeric matrix.

Alternatively, it is plausible that interactions at the polymer/*p*Na crystals surface leads to slight strains or distortions that break the nominal centrosymmetry of the *p*Na crystals over a distance extending more than a few atomic layers into the crystal. However, given that the thicker *p*Na/PMMA sample produced a slightly lower signal, this symmetry breaking appears not to extend throughout the full sample thickness. Nevertheless, the estimates in the last column provide an interesting basis for comparison with previous studies. Hwang et al. [35] obtained strong second harmonic generation from *p*Na /PS mixtures that were formed by flash evaporation from a toluene solution. When the *p*Na concentration was 10% by weight they observed a signal over 1000 times greater than urea which has a nonlinear coefficient of $d_{36} \simeq 1.2\,pm/V$ [36]. Earlier in 1988 Miyazaki et al. [24] observed SHG from a cast benzene solution of a *p*Na/ PCL (Mw = 75000) composite that that was 115 times as large as urea when the *p*Na composition was 20% by weight. Although our observations lead to lower effective second order nonlinear coefficients, we note that the previous systems investigated by Hwang et al. and Miyazaki et al. are both highly scattering, whereas our *p*Na/ polymeric films have reasonable optical quality, an advantage for many potential applications. Furthermore, the x-ray data suggest that our films are preferentially oriented crystals, so that it might be possible to improve the SHG response by optimizing the fundamental beam's angle of incidence.

In summary, except for the low weight PMMA-*p*Na films, all of the samples produce second harmonic light with good efficiency observable by the naked eye with low energy fundamental pulses. The above estimated quadratic surface susceptibilities are all several orders of magnitude greater than that expected from an isolated *p*Na crystalline surface based on the estimates of Malagoli and Munn [33]. We note that these authors predict that the dominant contribution from the centrosymmetry breaking at the crystal surface rapidly vanish with the main contributions

coming from the first two unit cells. We hypothesize that interactions with the polymeric hosts, most likely through hydrogen bonding, introduces alteration of the normally centrosymmetric head to tail crystalline structure of *p*Na that persists over multiple molecular layers enhancing the second harmonic response relative to that of an isolated crystal.

4. Conclusion

In this study, we have shown it is possible to obtain a strong macroscopic second harmonic response from *p*Na molecules organized in a layered thin film with good optical quality. A modified version of capillary growth was used to obtain various *p*Na thin films in different host polymeric matrices. The thin films here obtained in a confined environment have distinct nonlinear optical properties compared to bulk *p*Na crystals. It was observed that matrix with long molecular chains tend to produce lamellar structures which favour SHG while matrices with short molecular chains leads to randomly oriented *p*Na microstructures that do not generate appreciable second harmonic light. The strength of the observed SHG signal in these systems, is roughly an equivalent to that previously measured in electro- spun *p*Na-PMMA fibers [4], if one assumes that any given ray of the incident fundamental beam will encounter on average 3-5 *p*Na nanocrystals when traversing the fibers. This suggests that rather than the strong dc electric fields applied during the electro-spinning process, *p*Na-polymer interactions are likely to play a major role in inducing the strong SHG response. Future efforts will explore whether the response of these films can be optimized by varying the relative *p*Na – polymer concentration or by changing the temperature under which the films are formed.

The fabrication method used here should be extendable to other organic molecules with large dipole moments and strong second order nonlinear optical responses that crystalize primarily though hydrogen bonding via the donor and acceptor moieties. Given the large number of NLO active organic compounds that crystallize in centrosymmetric crystalline structures; this technique has the potential to open up a new pathway to fabricate sub-wavelength photonic materials into with large second order nonlinear optical responses. The thin films here obtained in a confined environment have distinct optical nonlinear properties in relation to that of the ordered bulk structure.

5. Acknowledgements

Hugo Gonçalves thanks the Portuguese Foundation for Science and Technology (FCT) for the support under grant PD/BD/111873/2015. The equipment used to characterize the second harmonic response of the thin films was acquired within the framework of the Portuguese National Program for Scientific Re-equipment, contract REEQ-25/FIS/2005 with funds from

POCI 2010 (FEDER) and FCT. The Raman microscope was acquired through the project nSTeP Nanostructured Systems for Tailored Performance, NORTE-07-0124-FEDER-000039, ON.2. The authors thank Desy at PETRA P03, Hamburg Germany for beam time and support through the project I-20170586 EC.

References

[1] Cabanetos C, Bentoumi W, Silvestre V, Blart E, Pellegrin Y, Montembault V, Barsella A, Dorkenoo K, Bretonnière Y, Andraud C, Mager L, Fontaine L and Odobel F 2012 New cross-linkable polymers with Huisgen reaction incorporating high μβ chromophores for second-order nonlinear optical applications *Chem. Mater.* **24** 1143–57

[2] Vallée R, Damman P, Dosière M, Toussaere E and Zyss J 2000 Nonlinear optical properties and crystalline orientation of 2-methyl-4- nitroaniline layers grown on nanostructured poly(tetrafluoroethylene) substrates *J. Am. Chem. Soc.* **122** 6701–9

[3] Li M, Li Y, Zhang H, Wang S, Ao Y and Cui Z 2017 Molecular engineering of organic chromophores and polymers for enhanced bulk second-order optical nonlinearity *J. Mater. Chem. C* **5** 4111–22

[4] Goncalves H, Saavedra I, Ferreira R A S, Lopes P E, De Matos Gomes E and Belsley M 2018 Efficient second harmonic generation by para-nitroaniline embedded in electro-spun polymeric nanofibres *J. Phys. D. Appl. Phys.* **51**

[5] Rau I, Armatys P, Chollet P A, Kajzar F and Zamboni R 2006 Conjugated polymers oriented organic thin films for nonlinear optics *Molecular Crystals and Liquid Crystals* vol 446 pp 23–45

[6] Ledoux I and Zyss J 2002 Molecular engineering of molecules and materials for quadratic nonlinear optics *Comptes Rendus Phys.* **3** 407–27

[7] Jonathan W. Steed J L A 1993 Supramolecular chemistry. *Science* **260** 1762–3

[8] Maymó M, Martorell J, Molinos-Gómez A and López-Calahorra F 2006 Visible second-harmonic light generated from a self-organized centrosymmetric lattice of nanospheres. *Opt. Express* **14** 2864–72

[9] Kajzar F, Messier J, Chemla D S and Zyss J 1987 Nonlinear Optical Properties of Organic Molecules and Crystals *by DS Chemla J. Zyss, Acad. Press. New York* **1** 51

[10] Bhattacharya S and Saha B K 2011 Inclusion of a chiral guest in a centrosymmetric organic host lattice *CrystEngComm* **13** 6941–4

[11] Zappe H 2010 Fundamentals of Micro-optics Technology , Devices and Applications

[12] Papadopoulos M G, Sadlej A J and Leszczynski J 2006 *Non-Linear Optical Properties of Matter*

[13] Werner L, Caro J and Finger G 1992 Optical second harmonic generation (SHG) on p-nitroaniline in large crystals of AIPO.hlf.4.rhlf.-5 and ZSM-5 *Zeolites* **12** 658–63

[14] Dadsetani M and Omidi A R 2015 Linear and nonlinear optical properties of 3-nitroaniline (m-NA) and 4-nitroaniline (p-NA) crystals: A DFT/TDDFT study *J. Phys. Chem. Solids* **85** 117–31

[15] Parka C, Choia U and Kimb C 1995 Theoretical Study of the Structures and Nonlinear Optical Properties of Hydrogen-Bonded Nitroaniline Systems **71** 1701–2

[16] Damman P, Vallée R, Dosière M, Toussaere E and Zyss J 2001 Oriented crystallization of NLO organic materials *Synthetic Metals* vol 124 pp 227–32

[17] Gauvin S and Zyss J 1996 Growth of organic crystalline thin films, their optical characterization and application to non-linear optics *Journal of Crystal Growth* vol 166 pp 507–27

[18] Henningsen T, Singh N B, Hopkins R H, Mazelsky R, Hopkins F K, Frazier D O and Singh O P 1994 Growth of binary organic NLO crystals: m.Na-p.NA and m.Na-CNA systems *Mater. Lett.* **20** 203–9

[19] Lalama S J and Garito A F 1979 Origin of the nonlinear second-order optical susceptibilities of organic systems *Phys. Rev. A* **20** 1179–94

[20] Werner L, Caro J, Finger G and Kornatowski J 1992 Optical second harmonic generation (SHG) on p-nitroaniline in large cyrstals of AIPO4-5 and ZSM-5 *Zeolites* **12** 658–63

[21] Isakov D V., Belsley M S, De Matos Gomes E, Gonçalves H, Schellenberg P and Almeida B G 2014 Intense optical second harmonic generation from centrosymmetric nanocrystalline para-nitroaniline *Appl. Phys. Lett.* **104** 181903

[22] Kobayashi H and Kotani M 1996 Observation of Generation of Intense Second-Harmonics at Etch Pits of p -Nitroaniline Single Crystal Surface *Mol. Cryst. Liq. Cryst. Sci. Technol. Sect. A. Mol. Cryst. Liq. Cryst.* **278** 125–30

[23] Kobayashi H and Kotani M 1994 Study of single crystal surface with second-harmonic generation: P-nitroaniline *Mol. Cryst. Liq. Cryst. Sci. Technol. Sect. A. Mol. Cryst. Liq. Cryst.* **252** 277–81

[24] Miyazaki T, Watanabe T and Miyata S 1988 Highly efficient second harmonic generation in p-nitroaniline/poly(lactone) systems *Jpn. J. Appl. Phys.* **27** L1724–5

[25] Manetta S, Ehrensperger M, Bosshard C and Günter P 2002 Organic thin film crystal growth for nonlinear optics: Present methods and exploratory developments *Comptes Rendus Phys.* **3** 449–62

[26] Sherwood J N and Simpson G S 1993 The growth, structural and optical characterization of large area, single crystalline thin films of 3-nitroaniline (mNA) *J. Cryst. Growth* **128** 981–5

[27] Buffet A, Rothkirch A, Döhrmann R, Körstgens V, Abul Kashem M M, Perlich J, Herzog G, Schwartzkopf M, Gehrke R, Müller-Buschbaum P and Roth S V. 2012 P03, the microfocus and nanofocus X-ray scattering (MiNaXS) beamline of the PETRA III storage ring: The microfocus endstation *J. Synchrotron Radiat.* **19** 647–53

[28] Trueblood K N, Goldish E and Donohue J 1961 A three-dimensional refinement of the crystal structure of 4-nitroaniline *Acta Crystallogr.* **14** 1009–17

[29] Harrand M 1979 Raman study on p-nitroaniline: Molecular structure in the molten phase *J. Raman Spectrosc.* **8** 161–4

[30] Marlow F, Hill W, Caro J and Finger G 1993 Raman-Study on P-Nitroaniline in Channels of the Molecular-Sieve Alpo(4)-5 *J. Raman Spectrosc.* **24** 603–8

[31] Harrand M 1975 Raman study on para nitroaniline single crystal. II: Internal Vibrations *J. Raman Spectrosc.* **4** 53–73

[32] Wang H and Weiner A M 2003 Efficiency of Short-Pulse Type-I Second-Harmonic Generation With Simultaneous Spatial Walk-Off, Temporal Walk-Off, and Pump Depletion *IEEE J. Quantum Electron.* **39** 1600–18

[33] Brevet P F 1996 Phenomenological three-layer model for surface second-harmonic generation at the interface between two centrosymmetric media *J. Chem. Soc. Faraday Trans.* **92** 4547

[34] Malagoii M and Munn R W 2000 Microscopic calculation of surface-induced second-harmonic generation in crystals of para-nitroaniline *J. Chem. Phys.* **112** 6757–62

[35] Hwang Y, Garetz B A and Okamoto Y 1992 Second-harmonic generation in pure p-nitroaniline and in composites with polystyrene by flash evaporation *Opt. Lett.* **17** 487–9

[36] Dmitriev V G, Gurzadyan D D and Nikogosyan D N 1997 *Handbook of Nonlinear Optical Crystals* (Berlin: Springer Verlag)

Conclusions and future work

What has been done

In this work we have discussed many aspects of the unusual optical nonlinear properties of polymeric nanofibers doped with organic *p*Na. Tuning the electrospinning parameters, such as the applied tension and flow rate of the polymeric solution, the size of the self-assembled *p*Na nanocrystals inside of the nanofibre vary with the resultant speed of the jet. In contrast, the resulting SHG field shows a tendency to increase as the size of nanocrystals decreases. The size and the strain induced during the self-assembling, result from interactions with the matrix and appear to induce at least a partial breaking of the bulk symmetry. The intense resultant SHG was observed and measured using the polarimetry technique. The magnitude of the effective non-linear coefficient is higher than the theoretical value reported in literature for a single surface which led us to conclude that there are other effects apart from the surface effects. These results made us question about the role of the polymeric matrix and of the strong electric field used during the electrospinning process. To eliminate the electric field contribution a modified version of the traditional capillarity growth method was used to growth *p*Na structures in confined environment and conditions. The shape, non-linear properties and orientational growth of the resultant structures were correlated. The shape and measured non-linear properties show differ according to the polymeric matrix used. The resultant SHG intensity in the best cases was observed to be a few orders of magnitude greater than that generated by the doped nanofibres. The main results and conclusions are summarized in a reprint of three articles in chapter 5. We discussed the properties of hybrid nanofibers and the *p*Na structures, the nano crystals size, the influence of surface, bulky strain, polymeric matrix, depositions parameters and growth orientation.

What is still left to do

The two approaches that we explore and introduce overcome many of the restrictions associated with organic non-linear chromophores in optoelectronic applications, but there is still plenty of room for improvement. For example, a better exploration of the method used to grow the *p*Na structures could possibly go beyond the results discussed, improving this method to a potentially viable commercial process to fabricate optically non-linear custom-made structures. Another aspect that has not been addressed was the use of templates and seed nanocrystals to induce a preferential growth orientation. Besides the detailed testing of substrate effects we need also to investigate

grating effects. One of the limitations of the electrospinning process is the lack of controlled deposition. This is something, which in principle can also be controlled within a appropriate apparatus, but further investigation on this topic is still needed. In the polymeric structures obtained with the two approaches, the limits that the source bandwidth sets on the efficiency of the SHG was not yet determined. It would be interesting to measure the SHG bandwidth generated by an ultrashort laser with a few femtoseconds pulse width duration. This could potentially be of use in characterizing the temporal profile of ultrashort pulses. In future, properties such as wave guiding, lasing, SHG in function of incident frequency and higher harmonic generation can also be explored in such materials.

Another very interesting and exciting strategy is the possibility to use sieves and mixtures of chromophores to create layered sandwich like structures. This represents a very nice continuation of our approach and will hopefully allow deeper insights into the self-assembly of organic nanocrystalline structures for optoelectronic applications. The key to success in any kind of fundamental research is to find the unexpected and then explore how the limits of how science constrains the new phenomena. Thus, the prediction of future perspectives in any kind of research field is inherently risky. Nevertheless because of the highly diverse nature of organic world we can assume an exciting future and high activity in this field. For instance there is great potential in merging inorganic with organic structures, with plasmonic or biochemical applications motivating themes. There are still many other open questions to explore and we are looking forward to new challenges and tasks.